



HAL
open science

Coherent transport of ultracold atoms in disordered potentials: Manipulation of time-reversal symmetry in weak localization experiments

Kilian Muller

► **To cite this version:**

Kilian Muller. Coherent transport of ultracold atoms in disordered potentials: Manipulation of time-reversal symmetry in weak localization experiments. Optics [physics.optics]. Institut d'Optique Graduate School, 2014. English. NNT : 2014IOTA0013 . tel-01127067

HAL Id: tel-01127067

<https://pastel.hal.science/tel-01127067>

Submitted on 6 Mar 2015

HAL is a multi-disciplinary open access archive for the deposit and dissemination of scientific research documents, whether they are published or not. The documents may come from teaching and research institutions in France or abroad, or from public or private research centers.

L'archive ouverte pluridisciplinaire **HAL**, est destinée au dépôt et à la diffusion de documents scientifiques de niveau recherche, publiés ou non, émanant des établissements d'enseignement et de recherche français ou étrangers, des laboratoires publics ou privés.

INSTITUT D'OPTIQUE GRADUATE SCHOOL
ÉCOLE DOCTORALE ONDES ET MATIERE

DISCIPLINE : Physique

THÈSE

pour l'obtention du grade de Docteur en science de l'Institut d'Optique Graduate School
préparée au Laboratoire Charles Fabry

soutenue le 24. Novembre 2014

par

Kilian MÜLLER

Coherent transport of ultracold atoms in disordered potentials:
Manipulation of time-reversal symmetry in weak localization
experiments

Directeur de thèse : Thomas Bourdel – Institut d'Optique Graduate School

Composition du jury :

Président du jury : Gilles MONTAMBAUX – Paris XI
Rapporteurs : Olivier GORCEIX – Paris XIII
Patrizia VIGNOLO – Université Nice
Examineurs : Markus OBERTHALER – Universität Heidelberg
Bruno LABURTHE-TOLRA – Paris XIII
Membres invités : Vincent JOSSE – Institut d'Optique Graduate School

Foreword / Remerciements

One of the most fond memories of my time at the Institute d'Optique, one that will stay with me for the years to come and one that shows how much I enjoyed being part of the Atom Optics group there, must be my 30th birthday. It was a Thursday, I was in the third year of my thesis, and we were in the process of taking data. I did not plan on celebrating big. But my supervisor, Vincent Josse, had convinced me and my colleagues on the experiment to join him at his place for the birthday party of his wife. I was thinking nothing of it, and only found it a little weird that over three years I had never noticed that Marie and me shared the same birthday. Upon arriving it turned out that they had successfully, thanks in large part to my gullibility, organized a surprise party behind my back. Many of the permanent staff and of my fellow PhD and master students were there, there was food, wine, and the cake I had bought for Marie.

I was very lucky for having been accepted into the experiment of Vincent, and for having had the fortune to work closely with him, Fred, Jérémie, Valentin, and Vincent (junior). Having come from a different field I learned everything about optics and cold atoms from or with them, not to mention the physics of wave propagation in disordered media. Vincent's enthusiasm and guidance pushed our projects forward, and the work that we accomplished over the last years is testimony to the studious and cooperative atmosphere in the group. Especially during the crunch-times just before and during a publication, but also on the occasional discussion, I benefitted greatly from the presence, the advice, and the experience of Alain. Every member of the atom optics group, permanent staff and students, were always approachable and had an open ear for discussions. But a special mention must go to Lynn, Bess, Raphael, and Guillaume, with whom I started my PhD, and who became fast and supportive friends.

For a long stretch during my thesis I was nearly daily in the mechanical and optics workshop of the institute. It is so very important for the constructions and modifications of an experiment to be able to work with skilled and helpful technicians. As an added bonus, during my daily visits I developed a sixth sense of when there was cake during their coffee break. In the same sense I want to thank Frédéric, who was an invaluable help for all things related to electronics.

For the last two years of my thesis I was very happy to be involved in teaching at the institute. Even though it meant early hours, the contact

with the students, and with the teaching staff, Fabienne, Lionel, Thierry, and Cédric was more than worth it.

I was very happy to having been able to have Gilles Montambaux as the jury president of my defense. The book he co-authored with E. Akkermans [3] was a constant companion. Valuable and detailed feedback regarding my manuscript came from my referees, Olivier Gorceix and Patrizia Vignolo. The examiners, Markus Oberthaler and Bruno Laburthe-Tolra completed my jury. I was especially happy that Markus was able to come, since it was from him that I got the advice, more than four years ago now, to apply for a thesis in the group of Alain. I particularly enjoyed the discussion with the jury members following my presentation.

My always encouraging and caring family, as well as some old friends from my student time in Heidelberg were able to be there as well. Amos, Moritz, Max, and Eugenia (and Henrik and Anika, who were unfortunately not able to come): You are, without exception, fantastic people, and I could not have asked for better companions in my student time.

It was a big celebration after, and I am happy for each and every one of you who came and made it an awesome evening.

On my very first weekend in Paris I was sitting in a cafe, close to Nation. My “apartment”, a lousy 8 square meter over-expensive room, did not have internet, so I had already taken the habit of going either to the McDonalds across the road, or to this place that I had stumbled upon whilst looking for a shared flat to check my mails in the evening. You sat next to me, we started talking, and have not stopped since. I think that you, Anna, deserve an honorary title for having the patience and understanding it takes to be the partner of a PhD student. You were looking after me, encouraged me, and took care I was eating well - which earned you many brownie-points from my mum and my grandparents!

We are now living together, in a much nicer apartment than my first one, and are continuing our Paris adventure together.

Contents

1	Introduction	1
1.1	Course of this thesis	4
1.2	Outline of this manuscript	5
2	Wave propagation in disorder	9
2.1	Disorder, interference, and disorder averaging	9
2.2	Energy scales	10
2.2.1	Weak and strong disorder	13
2.3	The elastic mean free path and the transport path	13
2.4	Diffusion constants	15
2.5	Weak Localization	17
2.6	Strong / Anderson localisation	18
3	Introduction to our experimental apparatus	21
3.1	Imaging	23
3.2	From the oven to the first chamber: First stage preparation of the atoms	25
3.2.1	Manipulating atoms with magnetic fields	25
3.2.2	Radiative force	26
3.2.3	Collimating and slowing the atomic beam	28
3.2.4	Magneto-optical trap and optical melasses	29
3.2.5	Trapping and evaporation in the magnetic trap	31
3.3	From the first to the second chamber: Cooling to nano-kelvin temperatures	33
3.3.1	Dipole force	33
3.3.2	Gaussian beams	34
3.3.3	Transport to the second chamber	35
3.3.4	Magnetic levitation	38
3.3.5	Evaporation in the crossed optical dipole trap	42
3.3.6	Bose-Einstein condensation	43
3.3.7	Delta-kick cooling	46
3.4	Conclusion	49
4	Optical speckles	51
4.1	A general introduction to optical speckles	51
4.1.1	Intensity distribution	52
4.1.2	Spatial structure	53
4.2	The speckle configuration in our experiment	54

CONTENTS

4.3	Natural units	55
5	Modifications of the experiment	57
5.1	Imaging system	57
5.2	Dimple beam setup	59
5.2.1	Design considerations	61
5.2.2	Characterisation of beam shape and trap frequency	65
5.3	Speckle setup	68
5.3.1	Setup of the speckle	69
5.3.2	Characterisation of the speckle	71
5.4	Vaccum / LIAD	75
6	3D Anderson localization	79
6.1	Experimental sequence	80
6.2	Expected behaviour of the system	81
6.3	Experimental observations	83
6.4	Conclusions	87
7	Coherent Backscattering	89
7.1	The Coherent Backscattering mechanism	91
7.2	Experimental sequence	93
7.3	Expected dynamics	95
7.3.1	Quasi 2D dynamics	95
7.3.2	Momentum space resolution	97
7.3.3	Dynamics of the CBS peak	97
7.4	Experimental results	99
7.4.1	Determination of the mean scattering and the transport time	99
7.4.2	CBS dynamics	102
7.4.3	Inherent disorder averaging	104
7.5	Conclusion	105
8	Coherent Backscattering revival	109
8.1	Reciprocity and time reversal symmetry	110
8.1.1	Basic notations on scattering theory	111
8.1.2	The reciprocity theorem	112
8.1.3	Reciprocity and Coherent Backscattering	113
8.2	Previous experiments on CBS and time-reversal invariance of wave propagation in complex media	114
8.2.1	Time reversal mirrors	114

8.2.2	Previous experiments on the deliberate breaking of time-reversal symmetry	116
8.3	Breaking of time-reversal symmetry by short perturbations	119
8.3.1	Perturbative picture	119
8.3.2	Extension to strong perturbations	122
8.4	Expected dynamics of the system	123
8.4.1	Evolution of the contrast in direct backscattering direction	125
8.4.2	Momentary shift of the momentum distribution	126
8.4.3	Evolution of the coherent contribution between dephasing and revival	126
8.4.4	Comparison between the CBS and the CBS Revival peak	127
8.4.5	Summary of the dynamics	128
8.5	Experimental observation of the CBS Revival	128
8.5.1	Experimental sequence	129
8.5.2	Presentation of the data and analysis	131
8.6	Numerical simulations and investigations of arbitrary pulse shapes	137
8.6.1	2D numerical simulation of the Schrödinger equation	138
8.6.2	Arbitrary shape of the dephasing pulse	142
8.7	Conclusion	144
9	Conclusion and outlook	147
A	Ensemble view of the experiment	149
B	CBSR data treatment	152
C	Properties of Rubidium 87	155
D	Optical setup for laser cooling, trapping, and imaging	156

CONTENTS

1 Introduction

The phenomenon of wave propagation is ubiquitous in nature: Light, sound, and quantum particles all are waves, and can therefore spread out and interfere. The expansion of a wave can be disturbed by changing the uniformity of the supporting medium. In the case of light for example, fluctuations of the refractive index of the medium or placing an object in its path will scatter the wave. Scattering from an ordered array of obstacles, as shown qualitatively in panel **a** of figure 1 can lead to discernible interference effects. The example given here is reminiscent of Bragg scattering, where the constructive interference can be intuitively understood by employing Huygens principle and by considering the regular positioning of the scatterers. If on the other hand the scatterers are located at random positions as in panel **b** one expects no easily predictable regular interference pattern, but rather an irregular intensity distribution.¹ Such a disordered potential is characterised by statistical quantities, like the average distance between two neighbouring scatterers, and the resulting irregular wave pattern depends on the specific realisation of the disorder. Averaging over many potential configurations with the same defining statistical properties will show how a wave propagates “on average” in such a medium, and one naively expects that interference effects cancel out. In other words, this train of thought suggests that when modelling the average propagation of waves through a disordered medium one can neglect the wave nature and treat the problem as a random walk of classical particles.

The propagation of waves through a medium with a random assortment of scatterers is encountered in many instances in nature (sunlight shining through a cloud, seismic waves propagating through the earth, surface water waves in a pond with reeds, ...) and in artificial technical situations (ultrasound imaging, electron transport through a metal with impurities, ...). It is therefore desirable to have a good understanding of wave propagation in complex disordered media. Quite successful first descriptions were based on the assumption given above that any interference effects would be completely washed out: The Drude-Boltzmann theory in the case of conducting electrons in metals, and later the radiative transport theory in the case of electromagnetic waves (see [81] and references therein). In both cases the resulting propagation is of diffusive nature.

Perhaps the first hint that interference effects must in fact not be ne-

¹This kind of interference pattern, known as “speckle”, is employed in our experiment and will be described in section 4.

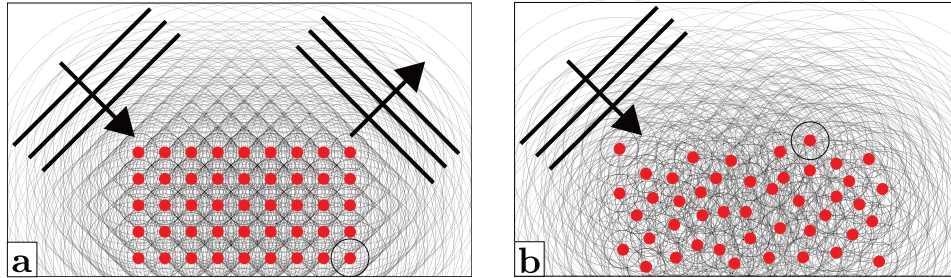


Figure 1: **Scattering of a wave from an ordered and a disordered array of obstacles.** An incoming plane wave (from the upper right hand corner) is scattered by a regular (panel **a**), or a random (panel **b**) assortment of scatterers (red). In the former case the resulting wave pattern exhibits a pattern that reflects the scatterers’ order, whereas in the latter case the interference is irregular.

glected came from P. W. Anderson in his seminal paper “Absence of Diffusion in Certain Random Lattices”, published in 1958 [11]. Loosely speaking, in certain strongly scattering cases where a classical particle could propagate further and further away from its original position as time increases, Anderson Localization predicts bound states of a wave, trapped in self-interference.² Famously, it went initially largely unnoticed before becoming a topic of thriving theoretical and experimental research.³

Anderson localization may be the most striking, but it is not the only effect due to coherent propagation in disorder. The theory of weak localization was conceived in order to explain the anomalous resistivity of a thin metal film subject to an external magnetic field (see [18] and references therein). Weak localization results in a correction of the diffusion constant, or equivalently a correction of the resistivity, and relies on the time-reversal symmetry of wave propagation in the disordered medium. An external magnetic field breaks this symmetry, therefore changing the resistivity as a function of the applied magnetic field [7, 105]. Weak localization is nowadays seen as a precursor of Anderson localization.

Many experiments were carried out on the observation of Anderson localization and weak localization with electrons and classical waves (most

²The terminology of strong and weak scattering media will be explained in section 2.2.1.

³Anderson was jointly awarded the 1977 Nobel prize for this and related works [12].

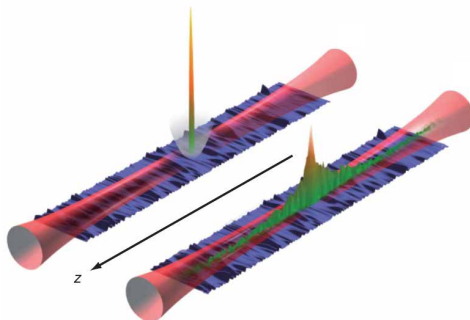


Figure 2: **1D Anderson localization of ultracold atoms.** A cloud of atoms confined in a 1D waveguide is released from a trap and expands until it reaches its exponentially localized state. Graphic reproduced from [20].

notably light and ultrasound), and an overview of previous works will be presented in the introductions of chapters 6 and 7. Our group is one of the first to add ultracold atoms to the mix, which resulted in the observation of 1D Anderson localization in 2008 in parallel to a group at LENS in Florence, Italy [20, 97, 14]. The appeal of ultracold atoms lies in the control the experimenter can exercise over many important parameters: The system is very well isolated from the environment and is therefore highly coherent, its dimensionality can be controlled, properties of the disordered potential can be changed easily, the interaction between the atoms and the potential can be made completely conservative (no absorption), the interactions between the atoms can be controlled, and the density of the atomic cloud can be imaged directly. Since the propagation of waves in disordered media is theoretically and computationally hard to solve, especially in the case of Anderson localization, ultracold atoms therefore provide a nice test bed to explore still unsolved questions [119, 14, 66, 101].

Despite there having been theoretical and experimental explorations on coherent transport in disordered media for over half a century now the field is still very active: Only during the duration of this thesis several new ideas were developed theoretically, and a small and subjective list includes for example a novel mechanism explaining weak and Anderson localization [42], a novel feature in the momentum distribution of an Anderson localized sample of ultracold atoms (“Coherent Forward Scattering”, CFS) [59, 79, 69, 46], and a novel signal appearing when breaking and restoring the time-reversal symmetry in a weak localization experiment (“Coher-

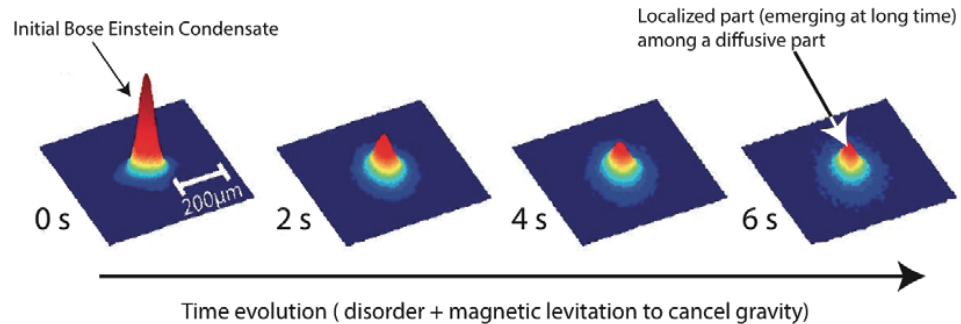


Figure 3: **3D Anderson localization of ultracold atoms.** A fraction of the atoms were localized and detected as a peak emerging from the diffusive atoms after long propagation times in the disorder.

ent Backscattering Echo” or “Coherent Backscattering Revival”, CBSE / CBSR) [80]. These were accompanied by experimental successes like a test of the universality of the metal-insulator phase transition in 3D [75], the observation of 3D Anderson localization with ultracold atoms [56, 103], and the measurement of the mobility edge [103, 62].

1.1 Course of this thesis

After the initial success of observing 1D Anderson localization in 2008 it was decided to mount an experiment specifically to study the propagation of ultracold atoms in a 3D configuration. It was constructed in the atom optics group led by Alain Aspect at the Institut d’Optique at Palaiseau, France, with Vincent Josse as team leader, Alain Bernard and Fred Jendrzejewski as the PhD students, and Patrick Cheinet as PostDoc. When I arrived in 2011 the setup was about finished and the studies on 3D Anderson Localisation went underway. With Jérémie Richard as a new arrival we then undertook a study on a phenomenon akin to weak localisation, called Coherent Backscattering. Here, we monitored the momentum space evolution of the waves propagating in the disorder, a fact that enabled us to also characterize two important transport parameters, the mean free time and the transport time. At this point the experiment had proven to be able to produce competitive results. In order to ensure more flexibility for future experiments several major modifications were carried out during the middle of this thesis. After their completion Valentin Volchikov joined us as Post-

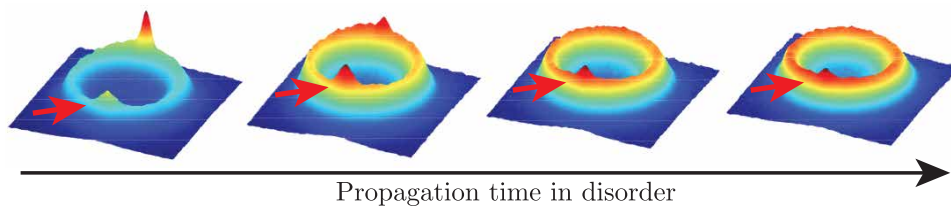


Figure 4: **Coherent Backscattering.** The appearance of the Coherent Backscattering peak, indicated with the red arrows, was observed in momentum space as a function of the propagation time. It is a telltale sign of coherent and time-reversal invariant transport in disorder.

Doc and Vincent Denechard for his master thesis. Another experiment on a novel effect, the Coherent Backscattering Revival was carried out during the last year of this thesis.

The combined works presented here would not have been possible without the dedicated work by all members of our team. Besides the PhD students and PostDocs mentioned above we were very lucky to benefit from the visits of Aditya Date and Raymond Santoso who joined us for several months as master students.

1.2 Outline of this manuscript

An introduction to the topic of wave propagation in complex disordered media is given in **Chapter 2**. The key concept of disorder averaging is introduced before qualitatively motivating basic effects like scattering, the mean free path, and the transport path. Weak localization and Anderson localization are introduced at the end of this chapter.

In **chapter 3** an overview over our experimental cycle is given, with which we produce a sample of ultracold atoms in the nano-Kelvin regime. Some standard experimental techniques used in cold atom experiments that we employ are briefly introduced. This includes a special feature of our experiment, the magnetic levitation, which cancels gravity for the atomic sample. These experimental steps are equal, bar some minor modifications and improvements, to all experiments presented in this thesis. The last leg of the experimental cycle that is specific to the experiment in question will be detailed in the chapters on Anderson Localization, Coherent Backscattering, and Coherent Backscattering Revival.

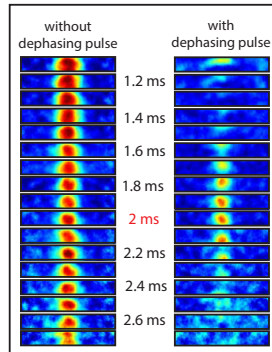


Figure 5: **Coherent Backscattering Revival.** With a controlled surgical dephasing the time-reversal symmetry of counter-propagating loops the coherent backscattering peak was destroyed, except for a specific time when quantum interferences aligned again, leading to a revival of the peak. In the left column the always visible CBS peak is shown for increasing propagation times in the disorder, whereas in the right column it appears only around the revival time, when time-reversal symmetry is briefly re-established.

Chapter 4 introduces another speciality of our experiment, the optical speckle, which provides us with a well controlled disordered potential.

The modifications of the experiment that were executed during this thesis are shown in **Chapter 5**. The imaging system, a beam path for a dipole trap beam, and the speckle setup were all completely redone. In each case the new setup is detailed and its performance characterised.

Briefly shown in **Chapter 6** are our results on 3D Anderson localization with ultracold atoms. The results we obtained were already described in depth in the thesis of F. Jendrzejewski [55], and only a short account is given here.

Chapter 7 presents the results obtained on Coherent Backscattering (CBS). After an introduction to the mechanism of CBS with an emphasis on the importance of the time-reversal symmetry of the wave propagation, a detailed analysis of the experimentally observed dynamics of the CBS peak is given.

The chapter on CBS forms the basis for our experiments on Coherent Backscattering Revival given in **Chapter 8**, where we manipulate the time-reversal symmetry of the wave propagation in the medium and study the effects on the CBS peak. An introduction to the relationship between time-reversal

symmetry and reciprocity is given, followed by an overview of related previous experimental works. The methodology of how we achieve time-reversal symmetry breaking is detailed, and the experimental results are presented. Finally, **Chapter 9** gives an overview over possible future projects that can be tackled with our experimental setup.

1.2 Outline of this manuscript

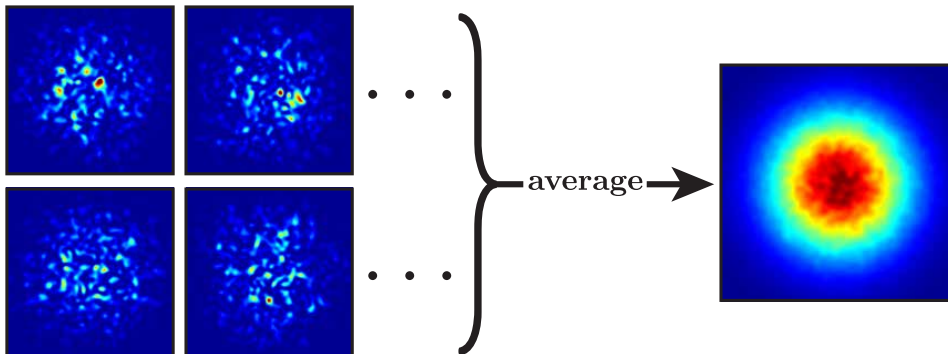


Figure 6: **Disorder average.** Shown on the left hand side are four examples of a numerically simulated speckle with a gaussian envelope. Each of the images is a distinctly different configuration, but all were generated according to the same statistical parameters. On the right hand side an average over 1000 such different configurations is shown. Gradually the features corresponding to a specific realisation disappear, leaving in this case only the gaussian envelope.

2 Wave propagation in disorder

In this section a qualitative overview over wave propagation in a disordered medium is given. We will motivate several key concepts, like relevant energy scales and disorder averaging, which will be revisited and explored more in depth when necessary in later sections. This discussion is based on several works on this topic [3, 64, 81, 104]. The qualitative results shown here are mostly general, but an emphasis is put on our specific situation, that is, matter waves propagating in a speckle potential.

2.1 Disorder, interference, and disorder averaging

The general ingredients in the system we are considering are a wave that is exposed to a disordered medium. This disordered medium can in a first approximation be viewed as a number of scatterers located at random positions: In solid state physics for example these are the impurities in a conductor, or for electromagnetic waves they are random changes of the refractive index. An incident wave will then scatter on these impurities and interfere with itself, leading to a complicated interference pattern that is unique to the specific details of the system under consideration. We want to

make general statements on how a wave will propagate, which necessitates to derive results that are true “on average”.

In order to motivate this idea further we consider the case of an optical speckle.⁴ A speckle can be produced by shining a monochromatic laser beam (the wave) through a rough glass plate (the disordered medium), whereby the light acquires spatially random phases. The interference pattern behind the glass plate then produces a random distribution of bright and dark spots. Let us assume that we have many different rough plates, each with a distinct surface structure, but all of them are produced to comply with the same statistical properties. In this scenario then, the refractive index of the glass, and the average size of the surface structures will be the same for all plates. Changing the plate while leaving all other parameters of the setup equal will produce a different speckle pattern. Figure 6 shows four examples of numerically computed speckle patterns, each of them corresponding to a different realisation of the disorder. In order to find out what the average intensity distribution looks like we take the mean over many different disorder realisations. This will suppress all random fluctuations, smoothing out the intensity distribution, and revealing the overall structure. In this particular example we find that the intensity distribution is, on average, a symmetric gaussian.⁵

In this thesis we are interested exclusively in effects of wave propagation in disorder that survive such a disorder averaging. To imply that a quantity is disorder averaged we will use angled brackets $\langle \dots \rangle$: Using the example of the speckle given above, the individual intensity patterns I_k that are produced by specific disorder configurations enumerated by the index k result in the average intensity distribution $\langle I \rangle$,

$$\langle I \rangle = \frac{1}{N} \sum_k I_k, \tag{1}$$

where N is the total number of different realisations.

2.2 Energy scales

The average height and width of a scatterer in the disordered potential define certain energies. Together with the kinetic energy of the quantum particle

⁴Optical speckles are a fundamental part of our experimental setup, and will be treated in detail in section 4.

⁵This example, the overall gaussian intensity distribution, is somewhat arbitrary. One could imagine different setups with different outcomes, but in each case the random fluctuations would disappear through the disorder averaging, revealing the general structure.

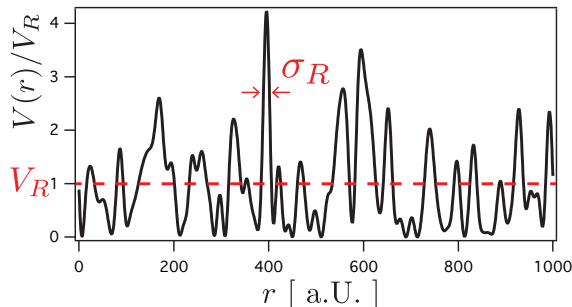


Figure 7: **Example of a 1-D speckle potential.** The average value of the potential V_R , as well as the typical size of a speckle grain σ_R is indicated.

propagating in it they determine the qualitative behavior of the system. We will use the optical speckle potential in this discussion, as it is used in all our experiments as the disorder, and loosely follow the arguments given in [104]. As an example, figure 7 shows a 1-dimensional speckle.

First we introduce the average value of a disordered potential $V(\vec{r})$, which will be referred to as the amplitude of the disorder $V_R = \langle V(\vec{r}) \rangle$. For speckles the square of this quantity is equal to the variance of the potential, $V_R^2 = \langle (V - V_R)^2 \rangle$, a result that will be derived in section 4. In theoretical calculations the disordered potential is commonly shifted by V_R to have zero mean value, $V(\vec{r}) \rightarrow V(\vec{r}) - V_R$, and we will use this convention unless otherwise noted.

Second, the speckle is a correlated disorder. This means that the potential fluctuates over a certain characteristic distance σ_R .⁶ This length defines an energy called the correlation energy $E_R = \hbar^2/(m\sigma_R^2)$, with m the mass of the particle.⁷ The correlation energy has the interpretation of the ground state energy of a particle with mass m trapped in a potential well of width σ_R .

Third is the total energy of the particle. If the potential fluctuations contribute just a small perturbation to the total energy, the total energy can be approximately given as the kinetic energy in free space $E_k = \hbar^2 k^2/(2m)$, with mass m and with wavevector k . For increasing disorder strength this

⁶Note that for a given disordered potential the length σ_R can be defined differently, up to a numerical factor. For this qualitative section it is to be understood just as an order of magnitude.

⁷We will follow this notation given for example in [64]. Another convention used for example in [104] is $E_R = \hbar^2/(2m\sigma_R^2)$.

2.2 Energy scales

is no longer the case, and the relationship between the wavevector and the energy is given in a more general form by the spectral function

$$A(k, E) = |\langle \vec{k} | E \rangle|. \quad (2)$$

Having the spectral function in mind the total energy can still be designated by E_k , where the wavevector is to be understood just as a parameter.

One can characterise the behavior of the system using the two ratios of these three energies:

- $\eta = V_R/E_R$, the ratio between the potential fluctuations and the correlation energy.
- $E_k/E_R = 1/2(k\sigma_R)^2$, the ratio between the particle's energy and the correlation energy.

The value η is important for the considerations of Anderson localization, which will be briefly discussed in section 2.6. In short, Anderson Localisation is the localisation of a wave in a disordered medium due to self-interference. It has to be distinguished from localisation due to bound states in sufficiently deep potential wells. If $\eta \ll 1$ a typical valley in the potential will not be deep enough to support a bound state. Therefore, if localisation is observed under this condition it is a strong hint that it is Anderson localization, and not due to trivial localisation of bound states in potential wells. In this localized case the potential fluctuations are smoothed out by the large de-Broglie wavelength and may be described by an effective disorder amplitude $V_R^{\text{eff}} = V_R^2/E_R$ [104, 106]. This regime is referred to as “quantum disorder”.⁸

If $\eta \gg 1$ trivial trapping in potential wells is a possibility. Anderson Localisation will still take place at energies above the classical percolation threshold,⁹ but it might be difficult to experimentally separate these two effects.

The ratio between the kinetic energy and the correlation energy is essentially a ratio between the typical size of a scatterer σ_R and the deBroglie wavelength of the particle $\lambda_{dB} \sim k^{-1}$. For $k\sigma_R \ll 1$ the deBroglie wavelength is much larger than the structures of the disordered potential, details

⁸Our experiments on Anderson localization, described in chapter 6, fall into this regime with η on the order of 0.01 to 0.1.

⁹When decreasing the energy of a classical particle in a given disordered potential the medium will eventually become an isolator, since energetically allowed regions become disconnected. The classical percolation threshold is the critical energy at which this transition from conductor to isolator happens.

2.3 The elastic mean free path and the transport path

of the potential therefore cannot be resolved: This already motivates that a single scattering event completely randomizes the direction of the wave, an effect that will be treated more in detail in section 7.4.1. Also this condition implies that the wave experiences an effective potential, which is smoothed out over a sphere with a radius on the order of λ_{dB} . For $k\sigma_R \gg 1$ on the other hand the deBroglie wavelength is much smaller than the smallest structures of the potential, quantum effects like tunneling are suppressed, and semiclassical considerations may be applied. The structure of a potential peak can be resolved by the wave and scattering may be very anisotropic.

2.2.1 Weak and strong disorder

If the disordered potential is sufficiently weak the trajectory of the particle is only slightly perturbed with respect to its free space counterpart, that is, one can assume that it moves in a straight line. In this approximation, called the thin phase grating approximation [52], the additional accumulated phase due to the disordered potential V is simply $\int V[\vec{r}(t)]dt/\hbar$, where $\vec{r}(t)$ is the trajectory. One speaks of weak disorder if this phase accumulated over a distance σ_R is small. If the particle's velocity is v the time it takes to cover this distance is $\tau = \sigma_R/v$, and the phase can be estimated as $V_R\tau/\hbar = \eta/(k\sigma_R) = \sqrt{\Delta}/2$. We have introduced here the important parameter $\Delta = V_R^2/(E_k E_R)$, which serves as the quantity that distinguishes weak ($\Delta \ll 1$) from strong disorder ($\Delta \gg 1$). The parameter Δ is also used to gauge whether the Born approximation is applicable: In weak disorder $\Delta \ll 1$ the first term of the diagrammatic series is sufficient to describe the scattering behavior [64].

Finally the weak disorder condition $\Delta \ll 1$ can be rewritten as $E_k \gg E_\Delta = V_R^2/E_R$, that is, the wave is only weakly scattered in a given disorder if its energy is larger than the characteristic energy E_Δ . This energy is important in the context of localisation in three dimensions, since it gives an estimate of the mobility edge, below which the states are localised.

2.3 The elastic mean free path and the transport path

A wave in a disordered medium can propagate for a certain distance before it is being scattered. This distance is called the mean free path, and we will motivate it and a related quantity, the transport path, following general and intuitive arguments given in [104]. This brief discussion is limited to 2D systems, which is the situation encountered in our experiments on Coherent Backscattering and Coherent Backscattering Revival treated in sections 7

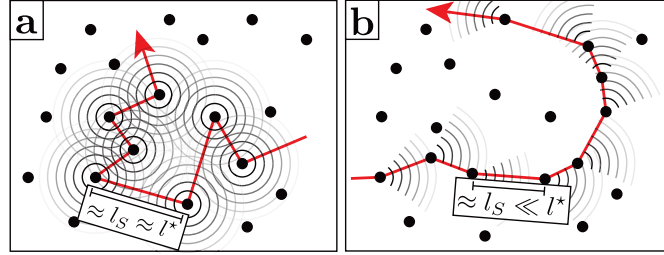


Figure 8: **Mean free path and transport path.** Shown here are two distinct cases of wave propagation in disordered media: In panel **a** the deBroglie wavelength is larger than the average structure of the potential ($k\sigma_R \ll 1$), leading to isotropic scattering. The propagation direction is therefore completely randomised after one scattering event, and the transport path l^* approaches the mean free path l_S . Panel **b** shows the case of fast particles ($k\sigma_R \gg 1$), where the waves are scattered in the forward direction. It then takes several scattering events to completely scramble the direction of propagation, leading to a transport path larger than the mean free path. It must be noted that in both cases only one out of a multitude of different possible trajectories is shown.

and 8.

Assuming weak disorder as defined in the previous section, the scattering cross section of a barrier can be calculated in the Born approximation: An average scatterer in the disorder has the amplitude V_R and the width σ_R , which then leads to a cross section of $\sigma_x \sim \eta^2/k$ for slow particles $k\sigma_R \ll 1$. Assuming that the density of scatterers n_{scat} is on the order of σ_R^{-2} the mean free path then is

$$l_S = \frac{1}{\sigma_x n_{scat}} \sim \frac{k\sigma_R^2}{\eta^2}. \quad (3)$$

We assumed for the calculation of the scattering cross section that $k\sigma_R \ll 1$, that is, we assumed that the deBroglie wavelength is larger than the average structure of the disorder. An incoming wave in this case is scattered isotropically in all directions as shown in figure 8 **a**. A single scattering event then is sufficient to scramble the information about the initial direction. This happens on a time scale $\tau_S = l_S/v$ with v the velocity of the particle, which is called the mean (elastic) scattering time.

In weak disorder the mean scattering time is linked with the spectral function, introduced in equation (2). It takes the form of a lorentzian in

the energy of the particle, centered around the kinetic energy E_k and with a width $\Delta E = \hbar/\tau_S$:

$$A(k, E) = \frac{\hbar}{2\pi\tau_S} \frac{1}{(E - E_k)^2 + (\hbar/(2\tau_S))^2} \quad (4)$$

For $k\sigma_R \gg 1$ the scattering is anisotropic, with a higher probability to scatter in the forward direction. This situation is shown in figure 8 **b**. In this case it takes several scattering events to completely scramble the information about the initial direction, which happens after a total path length l^* called the transport path. Again one can define the time it takes to lose the information about the initial direction, the transport time, as $\tau^* = l^*/v$. The opening angle of the scattering is $\sim (k\sigma_R)^{-1}$, which implies that it takes on average $(k\sigma_R)^{-2}$ scattering events to completely scramble the propagation direction. Furthermore in this limit of fast particles the scattering cross section is reduced by a factor $(k\sigma_R)^{-1}$. Comparing with equation (3) we can therefore write the order of magnitude of the transport path as

$$l^* \sim \frac{k^4 \sigma_R^5}{\eta^2}. \quad (5)$$

2.4 Diffusion constants

The propagation of waves in disordered potentials that we have considered so far in this section is diffusive in nature: In analogy to a classical particle in a disordered medium the path can be modelled as a random walk with an average step size equal to the transport path l^* introduced in the previous section. After many steps the probability distribution of the particle's position is gaussian with a width $\sqrt{2Dt}$:

$$P(t) = \frac{1}{(4\pi Dt)^{d/2}} \exp\left(-\frac{|\vec{r}|^2}{4Dt}\right) \quad (6)$$

The dimension of the system is denoted by d , and we have assumed here that the starting position at $t = 0$ is $\vec{r}_0 = 0$. The diffusion constant is denoted as D , and can be expressed in terms of the number of dimensions of the system, the velocity of the particle v , and the transport path l^* [64]:

$$D = D_B = \frac{1}{d} v l^* \quad (7)$$

Other notations exist, where the dimensionality d is not integrated into the diffusion constant. The subscript \dots_B indicates that in this form the

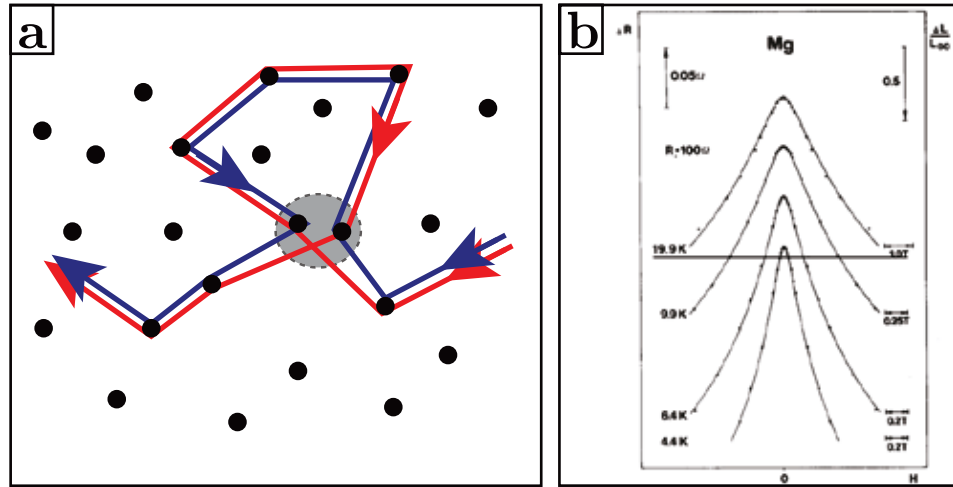


Figure 9: **Weak Localisation.** At the basis of weak localisation is the constructive interference of counter-propagating loops, shown schematically in panel **a**. Since the phase acquired while traversing the loop is the same for the red and the blue path both interfere constructively in an area around the origin of the loop (shaded gray). The interference increases the probability of return, and therefore slows down the propagation. The Weak localization effect in thin metallic films can be made evident by dephasing the electron counter-propagating paths using a magnetic field. Shown exemplary in panel **b** are resistance measurements in such a configuration as a function of the magnetic field (reproduced from [18]).

diffusion constant is also called the Boltzmann diffusion constant. As shown in section 7.4.1 we are able to experimentally extract the transport time τ^* , and therefore also the transport path, for a given initial velocity, allowing us to directly estimate the Boltzmann diffusion constant.

Formula (7) relies on the analogy to the random walk of a classical particle. Extending its validity to the propagation of waves in disorder assumes that there are no corrections due to interference. This assumption seems to be reasonable, since the interference corrections would have to survive the disorder averaging. In the next section though we will see that there are indeed corrections to the classical transport picture.

2.5 Weak Localization

The first order corrections to transport in disordered media due to interferences are weak localisation and coherent backscattering. The two are very similar in their origin, since both rely on the constructive interference of counter propagating loops. In order to motivate that interference can lead to corrections of transport we will give a very brief introduction into weak localisation here. A more formal description with a focus on coherent backscattering will be presented in section 7.

As of now when talking about the propagation of waves in disorder we have pictured only one specific path, for example in figure 8. In reality a wave explores a multitude of trajectories at once, leading to interferences. Since we are interested in phenomena that survive disorder averaging (see section 2.1) we are looking for a class of distinct paths common to all disorder configurations, and which produces interference effects that are also independent of the specific disorder configuration.

Such a class is the one of counter-propagating loops, an schematic example of which is shown in panel **a** of figure 9. In such a loop the phase acquired by the clockwise and the counter-clockwise path is exactly equal, leading to constructive interference in an area around the origin of the loop. This interference increases the probability of return, and consequently the propagation of a wave is therefore slowed down. Such loops exist for all disorder configurations, and the effect of slower propagation due to interferences therefore survives the disorder averaging. This effect is called weak localisation.

The importance of these interference effects on the propagation depends on the average number of times a given trajectory crosses with itself to form a loop. This number can be easily estimated: Since the propagation is diffusive we can assign a diffusion constant D , which contains all possible corrections due to interferences. In d dimensions the wave then explores a volume $\sim L^d = (2Dt)^{d/2}$ within a time t . Assuming that the wavepacket has a size comparable to the deBroglie wavelength the volume traced out by the trajectory within a time dt is $\lambda_{dB}^{d-1}vdt$ with v the velocity of the particle. The increase of probability for a crossing after the propagation time t then is the ratio of these two volumes, $dp_x(t) \sim \lambda_{dB}^{d-1}vdt/(2Dt)^{d/2}$. The total probability then is [3]

$$p_x(t) \sim \int_{t_0}^t \frac{\lambda_{dB}^{d-1}v d\tilde{t}}{(2D\tilde{t})^{d/2}}. \quad (8)$$

The time t_0 serves as a cut off to make the integral finite. Its physical interpretation is that diffusive propagation sets in for times $t > t_0$.

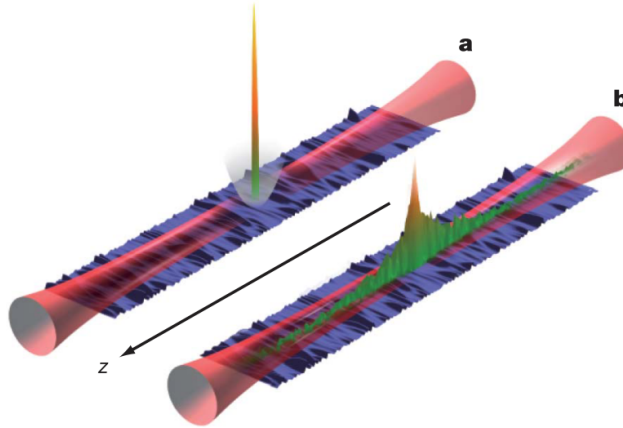


Figure 10: **1D Anderson Localization.** Shown here are images from the realisation of 1D Anderson localized ultracold atoms [20]. An initially trapped cloud (**a**) is released and can propagate along a waveguide (the pink tube). After an initial expansion a final stationary profile is reached (**b**).

The kind of correction we showed in figure 9 is only the first in a whole series of corrections. As the disorder strength increases the probability for crossings in equation (8) increases and loops of higher order become more important.

2.6 Strong / Anderson localisation

In sufficiently strongly scattering media transport can be suppressed completely, rendering the medium an isolator as opposed to a conductor. In this case the wave function is localized within a region of a certain size characterised by the localization length l_{loc} , and does not extend over the whole medium as the propagation time tends towards infinity. This localization is qualitatively different from the way one usually thinks about confining a particle or wave: Instead of surrounding it with sufficiently high potential barriers or mirrors, here the localization is solely due to self-interference. In a thought experiment, an initially Anderson localized system would start to diffuse indefinitely if one switched off only the interference effects. In other words, a quantum mechanical particle might be trapped due to interference, whereas a particle propagating in a purely classical manner would diffuse away.

This behaviour was first postulated by Anderson in 1958 [11], and went from being initially largely unrecognised to becoming a cornerstone in condensed matter, as well as other branches of physics.¹⁰ Anderson localization is a difficult topic, both in its theoretical description and in the experimental realisation. This is exemplified by there existing several different definitions of the phenomenon [114]. A simple working criterion follows from the title of Anderson’s original work and defines localization as the “absence of diffusion”:

$$D(E) = 0 \tag{9}$$

In this picture a particle of energy E in a given disordered potential is confined to some finite region due to self interference, giving the diffusion constant D a vanishing value.

Localization depends strongly on the dimensionality of the system, as shown by the scaling theory developed by Abrahams, Anderson, Licciardello, and Ramakrishnan [1]. This can be motivated qualitatively by considering the classical probability of return in a random walk as an indicator of the influence of interference effects: In a 1-dimensional system each scattering event reflects the wave towards its previous position, and interference effects are strong. Indeed, it turns out that in infinite 1D systems all states in a given disorder are localized, independent of their energy. Increasing the dimensionality decreases the impact of the interference effects: 2D systems are considered to be the marginal case, where states of all energies are still localized, but the region occupied by the localized states increases exponentially with the energy of the particle.

3D systems are qualitatively different, as there exists a critical threshold energy E_c called the mobility edge that separates diffusive from localized states. An estimation for the value of the mobility edge is given by the Ioffe-Regel criterion [54], relating the two fundamental length-scales of the system with each other:

$$kl \approx 1 \tag{10}$$

Here, $k = 2\pi/\lambda$ is the wave vector, and l is the mean free path. Localization therefore sets in when the wavelength becomes comparable to the mean distance between two subsequent scattering events. Crossing the mobility edge the medium experiences a phase transition from conductor to insulator. For energies around the mobility edge the diffusion constants and the

¹⁰For a historic overview of the development of the research concerning Anderson localization see [13].

localization lengths are predicted to vary according to critical exponents s and ν :

$$\begin{aligned} D &\propto |E - E_c|^s && \text{for } E > E_c \\ l_{loc} &\propto |E - E_c|^{-\nu} && \text{for } E < E_c \end{aligned} \tag{11}$$

Anderson Localization is still a field of active research, with open questions remaining especially in higher dimensional systems. The precise position of the mobility edge and the values of the critical exponents for example can be calculated numerically, but so far no satisfying analytical treatment exists. Precise experiments tackling these open questions therefore provide valuable input for the comparison with theoretical models.

Our experiment was custom built to investigate 3D Anderson localization with ultracold atoms. The first result was obtained at the beginning of this thesis, and is briefly described in section 6. A more in-depth discussion can be found in the thesis of F. Jendrzejewski [55].

3 Introduction to our experimental apparatus

As outlined in the first two introductory chapters, the purpose of our experiment is to study the coherence effects of wave propagation in disordered potentials. The waves in our experiment are the quantum mechanical matter waves associated with ultracold Rubidium 87 atoms.¹¹ In this chapter the experimental steps necessary to cool a gaseous ensemble of these atoms down to the temperatures necessary to perform our experiments are outlined.¹²

The need for low temperatures lies in the fact that the de Broglie wavelength λ_{dB} of a particle increases as its momentum p decreases (h is the Planck constant):

$$\lambda_{\text{dB}} = \frac{h}{p} \quad (12)$$

The wave nature of the atoms in an ensemble therefore becomes more and more apparent as the temperature decreases. In particular we have seen in section 2.6 that in order to enter the regime of Anderson Localization the de Broglie wavelength has to reach the same order of magnitude as the mean free path in the disorder (see equation 10). If, in a back of the envelope estimation, we assume the mean free path to be on the order of 1 μm , the necessary temperature

$$T = \frac{2\pi\hbar^2}{m_{\text{Rb}}k_{\text{B}}\lambda_{\text{dB}}^2} \quad (13)$$

is on the order of 10 nK (\hbar is the reduced Planck constant, m_{Rb} the mass of an ^{87}Rb atom, and k_{B} the Boltzmann constant).¹³

We cool the atoms down to these temperatures in several stages, using optical cooling and evaporation techniques, in an ultra-high vacuum environment. These techniques will be introduced in the following sections in the chronological order of a typical experimental sequence, preceded by a brief introduction to the imaging methods that are employed to gather information about the atomic cloud. For a more technical description of the

¹¹An overview over some relevant physical properties of ^{87}Rb can be found in appendix C.

¹²The second ingredient to our experiments, the disorder, is treated separately in chapter 4.

¹³The order of magnitude for the mean free path is justified by the fact that the disordered potential we are using is created optically. The typical structure size of said disorder is then on the order of the wavelength used, in our case 532 nm.

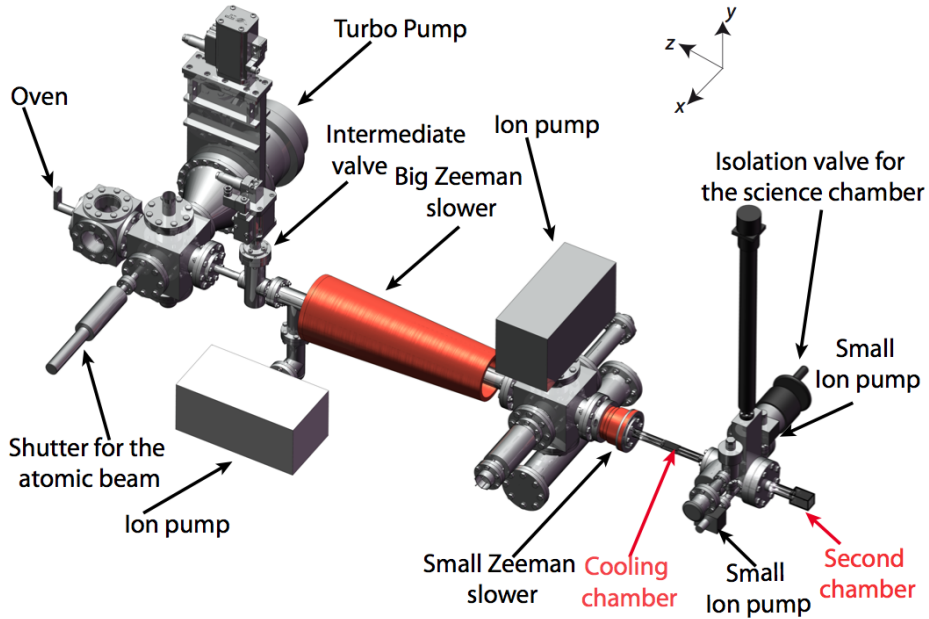


Figure 11: **Overview of the experiment.** The atoms originate from an oven containing a sample of rubidium, which is heated to 120°C . Rubidium at this temperature has a vapor pressure of about 10^{-3} mbar [109], which is the starting point of our experiment. Through several cooling and trapping steps (see text) a thermal sample of $\approx 10^7$ atoms with a temperature of $\approx 4\ \mu\text{K}$ is obtained in the first, or cooling chamber. They are then transported into the second, or science chamber, where with a final cooling sequence temperatures in the nano-Kelvin regime are achieved and all experiments take place.

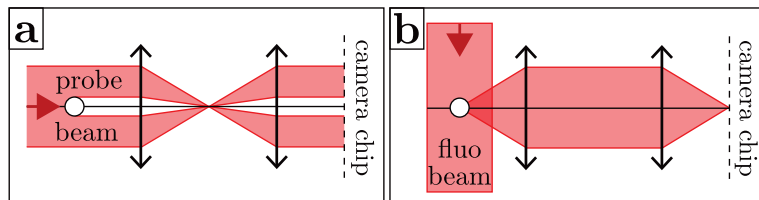


Figure 12: **Schematic of absorption and fluorescence imaging.** Panel **a** shows the scheme for absorption imaging, where the atomic cloud casts a shadow in the probe beam that is imaged onto the camera. In the case of fluorescence imaging shown in panel **b** the resonant laser beam is not directed towards the camera. Instead the light emitted by the excited atoms is collected and imaged onto the chip.

parts of the experiment mentioned in this section the reader is referred to the theses of A. Bernard and M. Fauquembergue [19, 41].

Figure 11 shows an overview of our experimental apparatus, which can be roughly separated into two major parts: The first part (pre-cooling) contains all elements from the oven (the source of the Rubidium atoms) to the first, or cooling chamber, where a cloud of atoms with a micro-Kelvin temperature is produced. This cloud is then transported to the second part, the second or science chamber, where the nano-Kelvin temperatures are achieved and all experiments carried out during this thesis take place. The experimental sequence laid out in this chapter qualitatively remains the same for all experiments described in this manuscript, except for minor changes or improvements.

In appendix A an ensemble view of the experiment is shown.

3.1 Imaging

The primary way information about the atomic ensemble is gathered in our experiment is by taking an image of the cloud's spatial density at the end of an experimental cycle. To this end three highly sensitive cameras (*EMCCD Hamamatsu C9102*) are installed: one for the first, and two for the second chamber. Two different imaging methods are employed in this experiment, absorption and fluorescence imaging. In both cases a laser beam resonant to the $F = 2 \rightarrow F' = 3$ (F being the total angular momentum quantum

3.1 Imaging

number) transition is shone onto the atoms.¹⁴ The source of this laser light is prepared on a separate optics table, and an overview of the process is given in appendix D. This light is then transported to the appropriate locations of the experiment via optical fibers.

Below is a brief outline of the most relevant aspects of absorption and fluorescence imaging. Their different setups are shown schematically in figure 12. A more detailed account on imaging cold atoms can for example be found in [60].

- **Absorption Imaging:** In the case of absorption imaging the laser beam illuminating the cloud is directed towards the camera. The image therefore shows the shadow produced by the cloud, which is darkest where the integrated density of the atoms is highest. The intensity that is recorded is linked to the density of the cloud by the Beer-Lambert law:

$$I(y, z) = I_0(y, z)e^{-\sigma \int n(x, y, z) dx} \quad (14)$$

Here, σ is the cross section that the atoms show towards the resonant light, and $n(x, y, z)$ is the density of the cloud. It is assumed that x is the optical axis of the imaging. If the light is exactly on resonance, and if the intensity is small compared to the so-called saturation intensity $I_{\text{sat}} = 1.67 \text{ mW/cm}^2$, the cross section is constant to a good approximation [109]:

$$\sigma = \frac{3\lambda^2}{2\pi^2} \approx 92 \times 10^3 \text{ nm}^2, \text{ with } \lambda = 780 \text{ nm} \quad (15)$$

Comparing the intensity $I(y, z)$ with an image taken under the same conditions but without atoms $I_{\text{ref}}(y, z)$ one can then simply deduce the integrated density:

$$\int n(x, y, z) dx = \frac{1}{\sigma} \ln \left(\frac{I_{\text{ref}}(y, z)}{I(y, z)} \right) \quad (16)$$

Since the resonant cross section σ is well known there is no further calibration necessary to deduce the number of atoms.

¹⁴Since during the imaging process there are many absorption and re-emission processes there is a significant heating of the cloud, and both of these types of imaging are destructive. Therefore a new sample has to be created after each time an image was taken.

- **Fluorescence Imaging:** In fluorescence imaging the resonant laser beam is not shining towards the camera. It just serves to bring the atoms into the excited state, from where they subsequently decay and emit a photon. During a single exposure each atom absorbs and emits many photons, which are emitted in all directions. A part of these fluorescence photons are then captured by a system of lenses, which transports the light towards the camera.

Since the photons are emitted in all directions only a part of them are collected by the imaging objective. The intensity reaching the camera is proportional to NA^2 , where NA is the numerical aperture of the objective. In order to be able to detect small atom numbers it is therefore imperative for the imaging system to have a large numerical aperture.

Contrary to absorption imaging, where the laser beam has a low intensity $I \ll I_{\text{sat}}$, for fluorescence imaging it is advantageous to operate at intensities $I \gg I_{\text{sat}}$. This prevents a translation of intensity fluctuations of the incident laser beam to fluctuations of the emitted intensity.

3.2 From the oven to the first chamber: First stage preparation of the atoms

In the following steps of the experimental sequence the interactions of atoms with resonant light and magnetic fields are used to collimate, cool and trap the atoms. Before commencing the description of the experiment a brief introduction to the underlying principles of how atoms react to an exposure to magnetic fields and resonant light are given in the following two sections.

3.2.1 Manipulating atoms with magnetic fields

The potential energy of a magnetic moment $\vec{\mu}$ placed in an external magnetic field $\vec{B}(\vec{r})$ is given by

$$E_B(\vec{r}) = -\vec{\mu} \cdot \vec{B}(\vec{r}). \quad (17)$$

Rubidium atoms are paramagnetic and therefore possess a magnetic moment, which stems from the spin \vec{S} and the orbital angular momentum \vec{L} of their valence electrons, and the total angular momentum of their nuclei \vec{I} . Using the normal convention to express the interaction energy between the magnetic moments and the external magnetic field using the Bohr magneton μ_B and appropriate g-factors one can write the hamiltonian as [109]

3.2 From the oven to the first chamber: First stage preparation of the atoms

$$\begin{aligned}\mathcal{H}_B &= \frac{\mu_B}{\hbar} (g_S \vec{S} + g_L \vec{L} + g_I \vec{I}) \cdot \vec{B}(\vec{r}) \\ &= \frac{\mu_B}{\hbar} (g_S S_z + g_L L_z + g_I I_z) B(\vec{r}),\end{aligned}\tag{18}$$

where in the second line it was assumed that the magnetic field points in z direction. If this energy contribution due to the external magnetic field is smaller than the fine structure splitting, the electron spin and orbital angular momentum couple to form the total electron angular momentum $\vec{J} = \vec{L} + \vec{S}$, and the hamiltonian simplifies to

$$\mathcal{H}_B = \frac{\mu_B}{\hbar} (g_J J_z + g_I I_z) B(\vec{r}).\tag{19}$$

Similarly, if this energy is small compared to the hyperfine structure splitting then \vec{J} and \vec{I} couple to form the total atomic angular momentum $\vec{F} = \vec{J} + \vec{I}$, and the hamiltonian becomes:

$$\mathcal{H}_B = \frac{\mu_B}{\hbar} g_F F_z B(\vec{r})\tag{20}$$

The addition of angular momenta follows the known rules (see for example [100]): In the combination of \vec{S} and \vec{L} for example the total angular momentum of the electron J can take on values m_J from $|L - S|$ to $L + S$ in integer steps. The same reasoning applies for the total atomic angular momentum F with quantum number m_F .

In the special case of the two hyperfine ground states $F = 1$ and $F = 2$ the energy shifts ranging both aforementioned regimes can be expressed in analytical form using the Breit-Rabi formula [23]:

$$E_{\pm} = \pm \frac{\hbar \Delta\nu}{2} \sqrt{1 + m_F \xi + \xi^2}\tag{21}$$

Here, $\xi = 2 \frac{\mu_B |\vec{B}(\vec{r})|}{\hbar \Delta\nu}$, and $\Delta\nu = 6.835$ GHz is the splitting between the hyperfine levels $F = 1$ and $F = 2$ in the absence of an external magnetic field. This formula is plotted in figure 13.

3.2.2 Radiative force

Here the interaction between an atom with a light field resonant to a cycling transition is considered. The description given here is based on [31, 50, 77], to which the interested reader is referred for a more detailed discussion. In such a cycling transition the atom is excited from its ground state $|g\rangle$ to

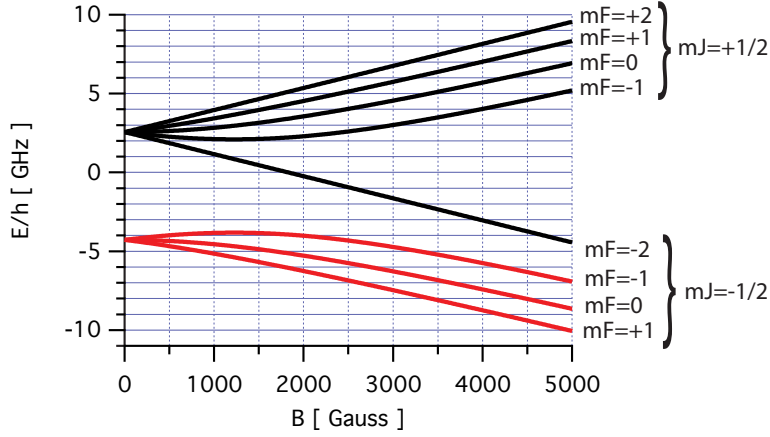


Figure 13: **Breit-Rabi diagram of the $^{87}\text{Rb } 5^2S_{1/2}$ ground states.** The $F = 1$ (red) and $F = 2$ (black) ground state energy levels are shown as a function of a static external magnetic field B . These energy levels were calculated using the Breit-Rabi formula (21).

an excited state $|e\rangle$ by the absorption of a photon, after which it falls back again to the ground state $|g\rangle$ while emitting a photon. For Rubidium 87 this condition is met for the $F = 2 \leftrightarrow F' = 3$ transition.¹⁵

In good approximation the atom can be considered to only have the aforementioned ground and excited state, which are separated by the energy $\Delta E = \hbar\omega_a$. Once in the excited state the atom falls back to the ground state after an average time τ , which defines the decay rate $\Gamma = \tau^{-1}$. The light field is assumed to be characterised by a single frequency $\nu_1 = \omega_1/2\pi$. The difference between the laser and the atomic transition frequency is called the detuning $\delta = \omega_1 - \omega_a$.

If the laser frequency is on, or close to resonance with the atomic transition ($|\delta| \ll \Gamma$) photons are absorbed, and subsequently spontaneously re-emitted. Both processes impart a momentum $\hbar k_1 = \hbar\omega_1/c$ onto the atom, where c is the speed of light. The absorbed photons all have the same direction, the propagation direction of the laser light. The spontaneously

¹⁵Since the excited states $F' = 3$ and $F' = 2$ are close to each other there is a small probability for the atom to be excited to $F' = 2$, and subsequently to fall into the $F = 1$ state. To compensate for this we are always adding laser light resonant with the $F = 1 \rightarrow F' = 2$ in order to pump the atoms back to the $F = 2$ state.

3.2 From the oven to the first chamber: First stage preparation of the atoms

emitted photons on the other hand fly off randomly, and their effect on the atom's momentum averages out to zero. Therefore a net force remains, which points in the same direction as the propagation of the laser. This net force is proportional to the momentum of a single photon $\hbar k_l$ and the rate of scattering γ :

$$\vec{F} = \hbar \vec{k}_l \gamma \quad (22)$$

This scattering rate depends on the intensity of the laser light with respect to the saturation intensity $s = I/I_{\text{sat}}$,¹⁶ the decay rate of the excited state Γ , and on the detuning δ . It also has to be taken into account that the atom can move with a velocity \vec{v} , and therefore experience the frequency of the light field Doppler shifted by the amount $\omega_d = -\vec{k}_l \cdot \vec{v}$. This velocity dependence of the scattering rate, and consequently of the resulting radiative force, can be exploited experimentally to manipulate the atoms. The scattering rate is given by [77]:

$$\gamma = \frac{s\Gamma/2}{1 + s + (2(\delta + \omega_d)/\Gamma)^2} \quad (23)$$

The acceleration rates that can be achieved by this radiative force are rather impressive: Under optimal conditions they are on the order of 10^4 m/s^2 for ^{87}Rb .

3.2.3 Collimating and slowing the atomic beam

A schematic drawing of the first part of the experiment is shown in panel **a** of figure 14 (to be compared with figure 11). The source of the Rubidium atoms is a sample placed inside an oven that is heated up to 120° C . Rubidium at this temperature has a vapor pressure of about 10^{-3} mbar [109], and it is this vapor that is the starting point of our experiment. The oven is connected to the rest of the experiment by a long and narrow tube, which limits the angle under which the gaseous atoms can exit the oven into the vacuum chamber, and therefore collimates the beam [41].¹⁷ For further collimation we use the radiative force in a transverse molasses configuration [78], as shown in panel **b** of figure 14: Two pairs of counter-propagating laser beams are shone perpendicularly onto the atomic beam. They are tuned slightly

¹⁶For ^{87}Rb one has $I_{\text{sat}} = 1.67 \text{ mW/cm}^2$.

¹⁷In order to separate the relatively high pressure in the region of the oven from the rest of the experiment we use a mechanical shutter, which is only briefly opened to allow the atomic beam to enter the experiment.

3.2 From the oven to the first chamber: First stage preparation of the atoms

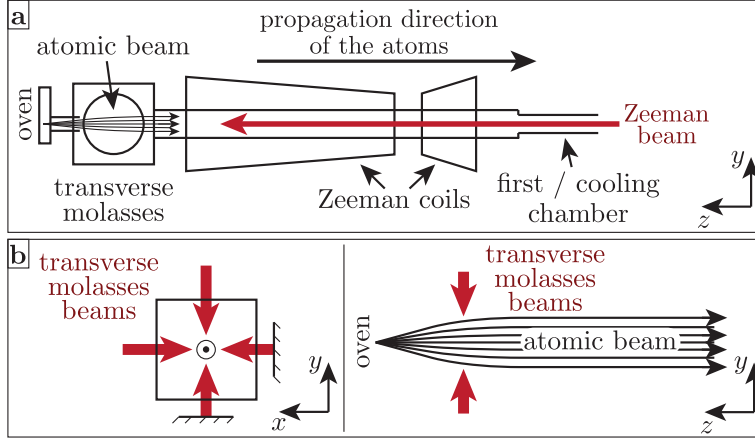


Figure 14: **Schematic view of the first part of the experiment and the transverse molasses configuration.**

below the atomic resonance (by ≈ -4.5 MHz) such that atoms with a non-vanishing transverse velocity component see the light Doppler-shifted closer to resonance, and consequently have this velocity component damped. This collimation greatly increases the flux of the atoms reaching the first atom trap (the magneto-optical trap, MOT) further downstream, as shown in figure 15, and therefore shortens the overall length of the experimental cycle.

In order to slow down the longitudinal velocity component (along z) this collimated beam of atoms is lead through a Zeeman slower [89]. Here, a resonant laser beam (the Zeeman beam in figure 14 a) propagating in opposite direction to the atoms is used to decelerate them. Since the atoms' velocity is changing they experience a varying Doppler shift of the Zeeman beam, which is compensated by shifting the atomic energy levels by a magnetic field that changes accordingly along z . At the end of this deceleration the atoms have a velocity of about 20 m/s, which is slow enough for them to be captured by a Magneto-Optical Trap.

3.2.4 Magneto-optical trap and optical molasses

The MOT is the first atom trap in our experiment. In it the decelerated atoms from the Zeeman slower are captured until its maximum capacity is reached (see figure 15). As shown schematically in figure 16 it uses three

3.2 From the oven to the first chamber: First stage preparation of the atoms

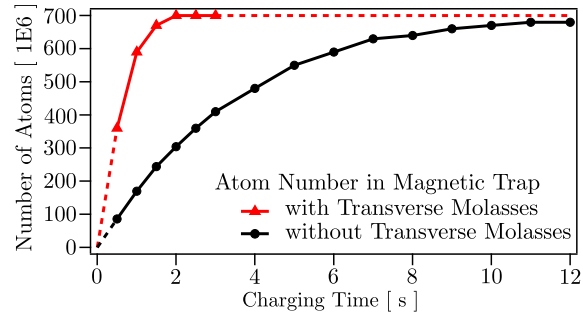


Figure 15: **MOT loading with and without transverse molasses.** The divergence of the atomic beam can be decreased by applying transverse molasses beams (see text). In doing so the flux directed towards the MOT is increased, leading to a much shorter loading time.

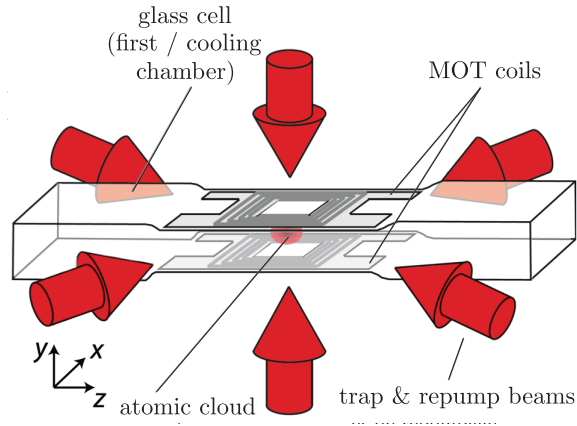


Figure 16: **Schematic drawing of the Magneto-Optical Trap.**

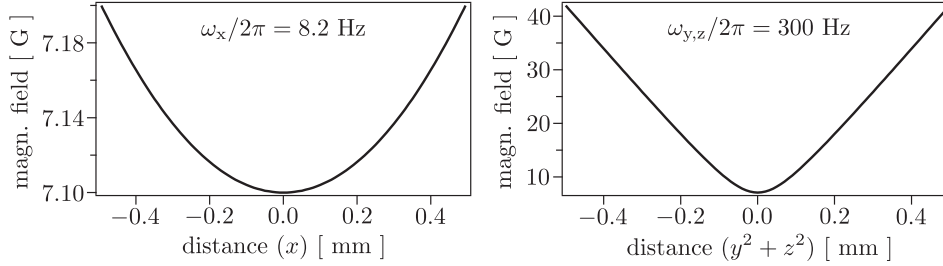


Figure 17: **Magnetic field in the Ioffe-Pritchard trap.** In the Ioffe-Pritchard configuration the magnetic field is cylindrically symmetric (with respect to the x -axis in our case). Note that the confinement is much steeper in the radial direction ($y^2 + z^2$) than along x ; the corresponding trap frequencies ω_x and $\omega_{y,z}$ are indicated. Due to a magnetic bias field the minimum field strength is non-zero (about 7.1 G).

pairs of counter-propagating laser beams, oriented along three orthogonal spatial directions, in conjunction with a magnetic quadrupole field [96, 78]. The magnetic field strength and the polarisation of the optical beams is chosen such that atoms deviating from the center of the trap experience radiation pressure forcing them back to the center.

Once the atom number in the MOT has saturated the mechanical shutter separating the oven from the rest of the vacuum system is closed, and the incoming flux of atoms is stopped.

At this point the temperature of the atomic cloud is $\approx 500 \mu\text{K}$. In a subsequent optical molasses phase [74, 34] the atoms are further cooled down to $\approx 50 \mu\text{K}$. Since the optical molasses also uses the cycling transition $F = 2 \leftrightarrow F' = 3$ the atoms are in the $F = 2$ state after the completion of this step.

3.2.5 Trapping and evaporation in the magnetic trap

In order to cool the atoms further they are transferred to a second, conservative trap. It uses the potential created by a static magnetic field as described in section 3.2.1, and is of the Ioffe-Pritchard type [94]. In this configuration the center of the trap is the point of minimal magnetic field strength (see figure 17), and the atoms therefore have to be brought into a low field seeking state where $g_F m_F > 0$ (see equation 20) before the magnetic trap is switched on. We choose the state $|F = 1, m_F = -1\rangle$, and

3.2 From the oven to the first chamber: First stage preparation of the atoms

therefore pump the atoms optically from $|F = 2\rangle$ to $|F = 1\rangle$ by applying the trap beams tuned to the $F = 2 \rightarrow F' = 2$ transition without the repumping beams.¹⁸ From this excited state the atoms de-excite to the $F = 1$ ground state, with roughly equal populations in the $m_F = \{0, \pm 1\}$ substates. In a last step before switching on the trap we optically drive transitions towards the $|F = 1, m_F = -1\rangle$ state in order to be able to capture most of the atoms.¹⁹

By switching on the magnetic fields of the trap we capture the atoms, and obtain a sample with a total number of about 10^9 at a temperature of $250 - 300 \mu\text{K}$.²⁰ To decrease the temperature the technique of forced evaporative cooling is employed: By lowering the trap depth the most energetic atoms are able to escape, which leaves a continuously colder sample in the trap. In magnetic traps this can be accomplished by the RF-knife method [36, 88]: Shining a radio frequency field onto the atoms in the trap can induce spin flips between different m_F states while leaving F unchanged, provided the RF field is resonant with the transition. Since the $m_F = -1$ is the only trapped state for $F = 1$ the atoms with a flipped spin are no longer caught and leave the cloud. The resonance frequency depends on the magnetic field via the Zeeman shift, and flips only happen at a certain field strength B for a given RF frequency. It is therefore possible to selectively let only atoms with a total energy greater than the potential associated with B evaporate. Reducing the RF frequency decreases the effective depth of the magnetic trap, leading to continuously lower temperatures.

In our experiment the evaporation sequence takes 10.5 seconds, after which we obtain a thermal sample of about 10^7 atoms at a temperature of $4 \mu\text{K}$ is obtained.

¹⁸The $|F = 2, m_F = 1\rangle$ and $|F = 2, m_F = -1\rangle$ states are also low field seeking, but experience higher loss rates [108].

¹⁹This optical pumping increases the number of atoms in the magnetic trap by about a factor 2. If the different m_F states prior to the pumping were populated equally one would expect a theoretical maximum increase of 3 of the atom number in the $m_F = 1$ state. Next to the possibility that our pumping is not perfectly efficient it is also possible that due to the optical molasses in conjunction with a remnant magnetic field there already is a higher population in the $|F = 1, m_F = 1\rangle$ state prior to the optical pumping.

²⁰The atomic cloud heats up during the transfer due to a center of mass movement induced by the optical molasses.

3.3 From the first to the second chamber: Cooling to nano-kelvin temperatures

The optical and mechanical access to the first chamber is limited due to the coils and laser beams of the MOT and the magnetic trap, described in the previous section. The second, or science chamber, is about 35 cm away from the first chamber, which gives us free optical and mechanical access around it to engineer the environment of the atoms for our experiments (compare with figure 11). This section details the transport from the first to the second chamber, and the subsequent final preparation of the atoms for our experiments.

During this thesis several key components around the second chamber, namely the imaging system, the dimple setup, and the optical speckle were completely rebuilt. The technical description of these modifications can be found in chapter 5.

In these final stages of the experimental cycle we make use of so-called optical dipole traps for the transport and cooling of the atomic cloud, which are created by far detuned gaussian laser beams. The underlying principles are introduced in the next two sections before the continuation of the description of the experimental cycle.

3.3.1 Dipole force

The dipole force results from the interaction between an atom and light with a frequency far off resonance of any transition. The description given here is based on [31, 50, 77], to which the interested reader is referred to for a more detailed discussion. As in section 3.2.2 we consider a simplified atom with only a ground state $|g\rangle$ and one excited state $|e\rangle$, which are separated by the energy $\hbar\omega_a$. The laser frequency is denoted by $\nu_1 = \omega_1/2\pi$, and the decay rate of the excited atomic state by Γ .

If the detuning between the laser frequency and the atomic transition frequency $\delta = \omega_1 - \omega_a$ is much larger than the line width ($|\delta| \gg \Gamma$), then in a fully quantum mechanical picture the ground state is perturbed by virtual absorption and stimulated emission of photons. This leads to a displacement of the ground state energy, called the AC Stark shift or light shift [31]. Equivalently a semiclassical picture can be adopted to understand this shift, where the light is viewed as a classical field: In this picture the external oscillating electric field induces an electric dipole moment in the atom. The dipole force then comes from the interaction between the external electric field and this induced dipole. In analogy with any other driven oscillator,

3.3 From the first to the second chamber: Cooling to nano-kelvin temperatures

the induced dipole can either oscillate in phase with the electric field if $\omega_l \ll \omega_a \Leftrightarrow \delta < 0$, or it can oscillate in phase opposition if $\omega_l \gg \omega_a \Leftrightarrow \delta > 0$. In the first case one speaks of a red-detuned laser, and the atom is attracted towards higher intensities. In the second case the laser is said to be blue-detuned, and the atom is repelled from higher intensities.

The potential associated with this interaction is given by

$$V_{\text{dip}}(\vec{r}) = -\frac{3\pi c^2 \Gamma}{2\omega_a^3 \tilde{\delta}} I(\vec{r}). \quad (24)$$

In the rotating wave approximation one can set the generalised detuning $\tilde{\delta} = \delta = \omega_l - \omega_a$. More precisely though one has to use

$$\tilde{\delta} = \left(\frac{1}{\omega_a - \omega_l} + \frac{1}{\omega_a + \omega_l} \right)^{-1}, \quad (25)$$

which contains the counter-rotating term.²¹ Note that the sign of the potential changes with the sign of the detuning $\tilde{\delta}$, which means that the creation of attractive and repulsive potentials is possible by choosing the appropriate light frequency.

3.3.2 Gaussian beams

The most commonly used transverse shape of a laser beam is a gaussian, the TEM₀₀ (Transverse Electro Magnetic). In this section some basic formula and technical terms are introduced. For a more in-depth treatment of gaussian beams used to trap atoms see [50]. For the propagation of a gaussian beam including lenses see for example [86].

The intensity of a gaussian beam propagating along the z direction with radial coordinate r is given as:

$$I(r, z) = \frac{2P}{\pi\omega(z)^2} e^{-2\frac{r^2}{\omega(z)^2}} \quad (26)$$

Integrating over the whole transverse profile recovers the total power of the beam P . The dependence of the waist ω on the longitudinal coordinate z is

$$\omega(z) = \omega_0 \sqrt{1 + \frac{z^2}{z_R^2}}, \quad (27)$$

²¹In our case, using lasers with wavelengths 1070 nm and 532 nm, omitting the counter-rotating term induces an error of more than 10% and 20% respectively.

3.3 From the first to the second chamber: Cooling to nano-kelvin temperatures

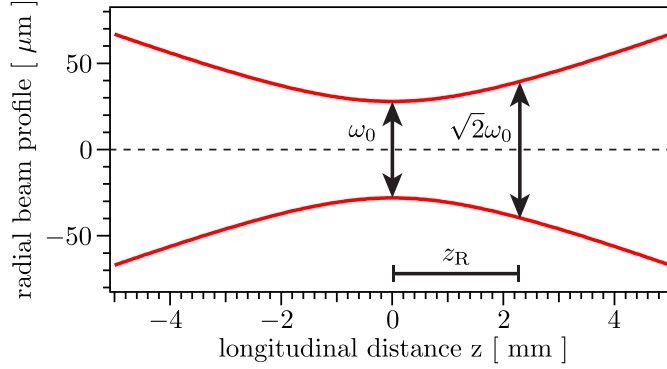


Figure 18: **Gaussian beam around its focal point.** As a concrete example the parameters chosen here are those of the tweezer (introduced in the following section): $\omega_0 = 0.28 \mu\text{m}$ and $\lambda = 1070 \text{ nm}$. The Rayleigh length in this case is $z_R = 2.3 \text{ mm}$.

where ω_0 is the minimal beam waist and $z_R = \pi\omega_0^2/\lambda$ is the Rayleigh length. Figure 18 shows a schematic drawing pointing out these parameters. The intensity distribution is directly linked to the potential felt by the atoms via relation (24), giving a maximum amplitude of the potential [50]

$$U_0 = -\frac{3c^2}{\omega_a^3} \frac{\Gamma}{\omega_0^2} \frac{P}{\delta}. \quad (28)$$

As discussed in the previous section, this potential is attractive for a red-detuned laser frequencies and forms a well. Around the center of this trap the potential can be approximated by a harmonic potential with trap frequencies

$$\omega_r = \sqrt{-\frac{4U_0}{m\omega_0^2}} \text{ and } \omega_z = \sqrt{-\frac{2U_0}{mz_R^2}}, \quad (29)$$

with m the mass of the atom.

3.3.3 Transport to the second chamber

The ensemble of atoms obtained at the end of the evaporation sequence in the magnetic trap is cold enough to be loaded into an optical dipole trap (see section 3.3.1), which we call the tweezer. This tweezer is characterised by its waist of $28 \mu\text{m}$, its Rayleigh length of 2.3 mm , and a maximum optical power

3.3 From the first to the second chamber: Cooling to nano-kelvin temperatures

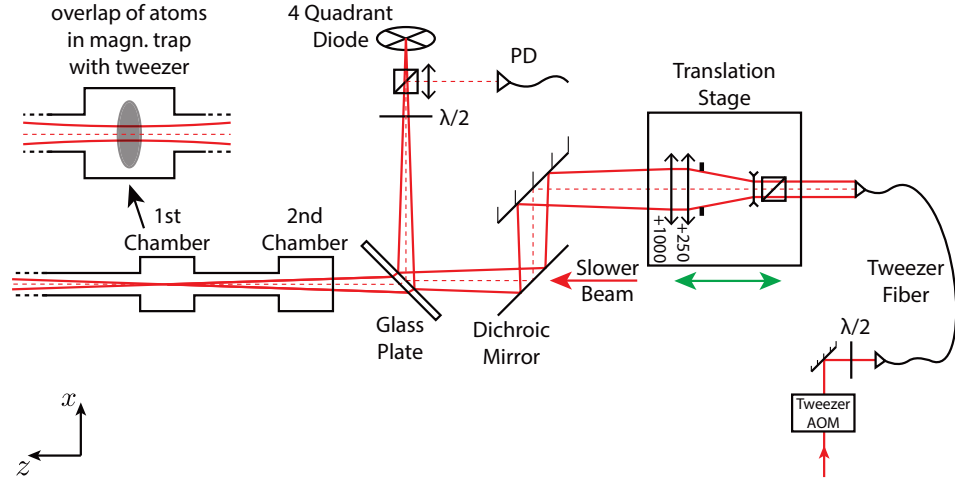


Figure 19: **Schematic drawing of the tweezer setup.**

of 2 – 3 W. This power can be switched off or regulated seamlessly with a controllable servo-loop containing an Acousto-Optical Modulator (AOM) and a photodiode (PD). Its wavelength of 1070 nm is far red-detuned with respect to the atomic transition. A schematic drawing of the tweezer setup is shown in figure 19. The loading is accomplished by ramping down the magnetic trap, while at the same time ramping up the power of the tweezer. Both the magnetic trap and the tweezer form cigar-shaped traps, and their long axes are oriented perpendicularly with respect to each other. Due to this non-ideal overlap, but also due to 3-body losses only about 50% of the atoms can be loaded into the tweezer. During the transfer from the magnetic trap to the tweezer there is no discernible heating.

Initially the position of the focal point of the tweezer overlaps with the center of the magnetic trap. The focalising lenses are mounted on a programmable linear translation stage (*Aerotech ABL80040*), and the focal point therefore follows the movement of the translation stage. With this setup we are able to transport the atoms, trapped in the focus of the tweezer, into the second chamber within about 2 seconds.

During the transport the cloud is heated from about 4 μK to 10 μK , and we lose a certain fraction of the atoms. This heating and atom loss can be attributed to vibrations of the trap during the transport. To calibrate how many atoms are lost during the transport the number initially loaded into the tweezer is compared to the number still left after a transport to the

3.3 From the first to the second chamber: Cooling to nano-kelvin temperatures

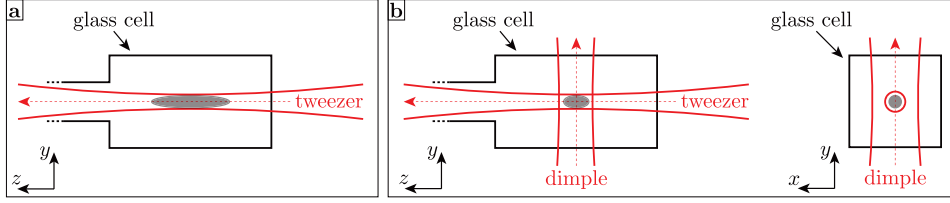


Figure 20: **Schematic drawing of tweezer and dimple in the second chamber.** Panel **a** shows the atoms (shaded gray) in the focal point of the tweezer. In panel **b** the atoms are located in the combined potential of tweezer and dimple. The dimple provides confinement in z -direction, whereas the tweezer is mainly responsible for the confinement in x and y direction.

second chamber, and back to the first one. That way in both cases the same imaging system is used, eliminating systematic errors in the estimation of the atom number. It is found that during such a transport about 25% of the atoms leave the tweezer, and we therefore estimate that during a single transport roughly 10-15% of the atoms are lost. This is confirmed by the imaging systems installed around the second chamber. At this stage the cloud contains approximately 5×10^6 atoms at a temperature of $10 \mu\text{K}$.

Coming from the magnetic trap the atoms are polarised in the state $F = 1, m_F = -1$. We noticed that after the transport the atomic ensemble was partially depolarised, indicating that they pass a region of zero (or very small) magnetic field where the atoms' spin cannot follow the field adiabatically. A magnetic coil was therefore installed between the first and the second chamber to ensure adiabatic transport. With this additional magnetic field all atoms arrive in the second chamber in the $F = 1, m_F = -1$ state.

Once the transport is complete we apply a second laser beam, called the dimple, to increase the longitudinal confinement as shown in figure 20. The dimple beam originates from the same laser as the tweezer and therefore also has a wavelength of 1070 nm. It has an elongated beam profile, with waists $\omega_x = 203 \mu\text{m}$ and $\omega_z = 91 \mu\text{m}$, and its maximum optical power is about 8 W.²² Like the tweezer, the dimple beam power is regulated over a servo-loop using an AOM. The atoms assemble at the crossing point between

²²This elongated profile simplifies the crossing with the tweezer and makes the setup less prone to variations of the positioning of the dimple. See section 5.2 for further details about the dimple beam setup.

3.3 From the first to the second chamber: Cooling to nano-kelvin temperatures

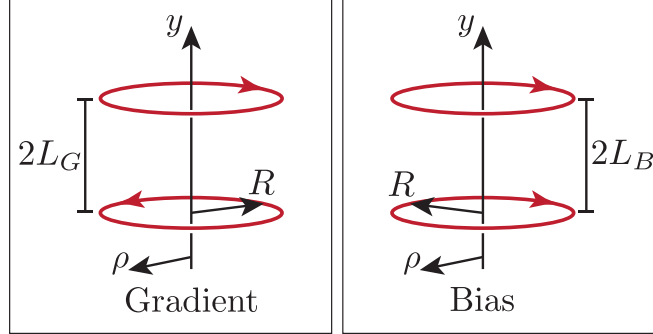


Figure 21: **Simplified model of the levitation coils.** In this simplified model the gradient and bias fields are each produced by a pair of coils with radius R . The distance between the coils is $2L_G$ and $2L_B$ respectively. To describe the field the cylindrical coordinates ρ and y are used. The total field is the sum of the gradient and the bias field.

the two laser beams, which increases the density of the cloud. Due to density related 3-body collisions the number of atoms decreases to $\approx 3 - 4 \times 10^6$. The temperature decreases slightly to $8 \mu\text{K}$ since we lower the intensity of the tweezer to counteract the above-mentioned atom loss.

In this combined potential of dimple and tweezer a final evaporation sequence takes place, which leads to the creation of a Bose-Einstein Condensate. As explained in the next section, gravity can be neglected from this point on due to our magnetic levitation.

3.3.4 Magnetic levitation

Our experiment was constructed to study the propagation of atomic matter waves in three dimensions in a disordered potential without any influence of outside forces. This means in particular that the effect of gravity has to be compensated. In order to achieve this goal a magnetic potential is applied to the atoms that cancels the gravitational potential. This magnetic levitation was built during the PhD of A. Bernard, and details to its construction and performance can be found in his thesis [19].

The total potential felt by the atoms is the sum of the gravitational

3.3 From the first to the second chamber: Cooling to nano-kelvin temperatures

potential and the magnetic potential (compare with section 3.2.1):²³

$$\begin{aligned} U(\vec{x}) &= mgy + m_F g_F \mu_B |\vec{B}(\vec{x})| \\ &= mgy + \mu |\vec{B}(\vec{x})| \end{aligned} \quad (30)$$

It is assumed here that the vertical axis is y , g is the gravitational acceleration, m is the mass of an atom, m_F is the magnetic quantum number, g_F is the Landé factor of the atomic state, μ_B is the Bohr magneton, and $\vec{B}(\vec{x})$ is the magnetic field. For convenience, the mass, Landé factor, and Bohr magneton are combined into the single factor μ . Ideally the total potential would be constant in a sufficiently large region, but this is not possible using static magnetic fields since $\vec{\nabla} \cdot \vec{B}(\vec{x}) = 0$. The potential $U(\vec{x})$ will therefore have trapping or anti-trapping curvatures. It was shown in [99] that under the constraint that the magnetic potential should support the atoms against gravity there is a lower limit for the trap frequencies ω_k ,

$$\sum_k \omega_k^2 \geq \frac{mg^2}{2\mu|\vec{B}|}, \quad (31)$$

where $k \in \{x, y, z\}$ is the index for the spatial direction. In order to achieve low curvatures it is therefore necessary to work at high magnetic fields.

The general principle of our levitation therefore is to produce a magnetic gradient field that acts against gravity, superposed by a large bias field to lower the curvature. The simplest method to achieve this is a pair of coils with current flowing in opposite directions to create the gradient field, and a pair of coils with current flowing in the same direction to produce the bias field as indicated in figure 21. Since the geometry of the coils is cylindrically symmetric with respect to the y -axis, the magnetic field will also be cylindrically symmetric and we will use the radial coordinate ρ and the vertical coordinate y to describe the field. In this configuration the absolute value of the magnetic field $B = |\vec{B}|$ approximated to second order

²³In this instance we neglect the possible potential due to the optical dipole trap and the interaction energy between the atoms.

3.3 From the first to the second chamber: Cooling to nano-kelvin temperatures

in ρ and y is [55, 41]:

$$\begin{aligned}
 B &\approx B_0 + b'y + b''y^2 + \rho^2 \left(\frac{b'^2}{8B_0} - \frac{b''}{2} \right) \\
 B_0 &= \mu_0 I_B \frac{R^2}{(R^2 + L_B^2)^{5/2}} \\
 b' &= 3\mu_0 I_G \frac{R^2 L_G}{(R^2 + L_G^2)^{5/2}} \\
 b'' &= \frac{3}{2} \mu_0 I_B \frac{R^2 (4L_B^2 - R^2)}{(R^2 + L_B^2)^{7/2}}
 \end{aligned} \tag{32}$$

B_0 is the bias field, $b'y$ is the gradient cancelling gravity, and b'' is the curvature introduced by the bias coils. The vacuum permeability is denoted by μ_0 , the current through the gradient coils is I_G , and the current through the bias coils is I_B . All coils are supposed to have the same radius R , and the distances between the gradient and bias coils are $2L_G$ and $2L_B$ respectively (see figure 21). The center of the configuration is at $\rho = y = 0$. The associated (anti-)trap frequencies of this configuration are:

$$\omega_y^2 = 2b'' \frac{\mu}{m} \quad \text{and} \quad \omega_\rho^2 = \left(\frac{b'^2}{4B_0} - b'' \right) \frac{\mu}{m} \tag{33}$$

Taking into account that b' must be equal to $-mg/\mu$ to compensate for gravity (see equation (30)) the frequencies are therefore at the low limit imposed by equation (31).

The parameter b'' can be fixed by demanding isotropic frequencies $\omega_y = \omega_\rho$, which yields

$$b'' = \frac{b'^2}{12B_0} = \frac{m^2 g^2}{12\mu^2 B_0}. \tag{34}$$

With a given geometric configuration of bias and gradient coils all parameters are therefore fixed by the requirements that the gradient should cancel gravity, and that the curvatures are isotropic. In order to loosen these constrictions the actual design of the levitation coils consists of two sets of bias coils close to the Helmholtz configuration as shown in figure 22. The currents in these two sets of coils I_{ext} and I_{int} can be adjusted independently. The combined bias field can be regarded as coming from a single pair of coils with an effective distance L_{eff} , which depends on the ration between I_{ext} and I_{int} .

3.3 From the first to the second chamber: Cooling to nano-kelvin temperatures

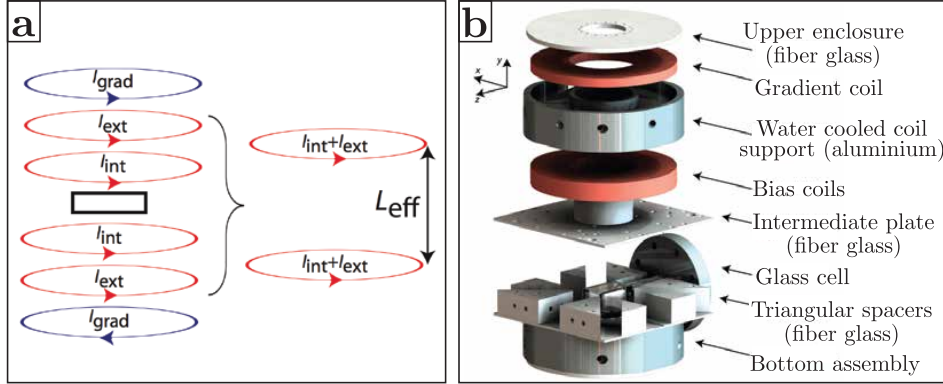


Figure 22: **Design of the magnetic levitation.** Panel **a** shows the scheme of the magnetic levitation, which consists of a pair of coils producing the gradient, and two pairs to produce the bias field. The bias field can be thought of as originating from a single pair of coils with an adjustable distance L_{eff} between them, which depends on the ratio between the currents of the external and the internal bias coil I_{ext} and I_{int} . Panel **b** shows the different parts that make up the assembly of the levitation.

The gradient and the bias coils each are fed by a dedicated highly stable power supply ($\Delta I/I = 10$ ppm). Their precision directly translates to a cancellation of the gravitational potential to the same accuracy. The power supplies of the bias coils can each generate a maximum current of 200 A, leading to a maximum bias field at the position of the atoms of $B_0 = 2000$ G. For atoms in the $F = 2, m_F = -2$ state, which we usually use for our experiments under levitation, the minimal frequencies are $\omega/2\pi \approx 0.18$ Hz [19]. In the experiments described later we chose lower bias currents between 40 and 50 A to make sure not to damage the levitation setup, which typically leads to frequencies of $\omega/2\pi \approx 0.5 - 0.8$ Hz.²⁴ The power supply of the gradient coils produces a maximum of 50 A, which is roughly twice the current necessary to achieve levitation in the $F = 2, m_F = -2$ state.

Depending on the sign of the Landé factor g_F and the sign of the magnetic quantum number m_F the curvature of the magnetic potential can either lead to trapping ($\mu > 0$), or to anti-trapping ($\mu < 0$). The associ-

²⁴The levitation coils were tested to withstand the maximum currents [19]. But the remaining curvatures at lower currents are sufficiently small for our experiments, so that taking the risk coming with applying the maximum currents was deemed unnecessary.

3.3 From the first to the second chamber: Cooling to nano-kelvin temperatures

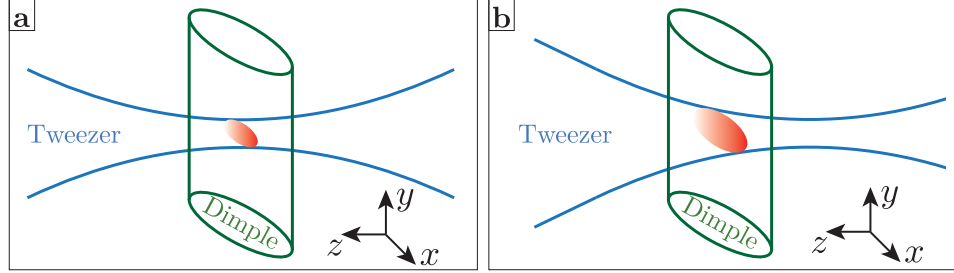


Figure 23: **Adiabatic opening of the tweezer confinement.** Initially the dimple crosses the tweezer at its focal point (**a**), providing a relatively tight confinement. By moving the focal point the trapping region, shown in red, can be adiabatically opened (**b**).

ated (anti-)trapping frequencies can be determined experimentally by time of flight experiments as described in [19, 55].

3.3.5 Evaporation in the crossed optical dipole trap

Coming from the magnetic trap in the first chamber the atoms are in the $|F = 1, m_F = -1\rangle$ state upon arriving in the second chamber. Since the magnetic levitation described in the previous section is configured to work with atoms in the $|F = 2, m_F = -2\rangle$ state we perform an RF induced transition from the former to the latter after the atoms are loaded in the crossed optical dipole trap and before the levitation is switched on.²⁵ For the remainder of the experimental sequence the levitation remains switched on.

The cooling in the crossed dipole trap can be separated into two parts: First, we force evaporation in the crossed dipole trap by ramping down the power in the tweezer and the dimple, which lowers the depth of the trap and its confinement (see equations 28 and 29).²⁶ Since the number of atoms and the confinement of the trap are decreasing, the collision rate between the atoms becomes lower until evaporation becomes ineffective. Additionally it would be necessary to lower the power in the tweezer and the dimple beam

²⁵Using the Stern-Gerlach like separation of the different m_F states in the magnetic levitation when the trap is switched off the efficiency of the RF transfer can be measured, and we find it to be practically 100%.

²⁶A detailed account of the evaporation can be found in the thesis of F. Jendrzejewski [55].

3.3 From the first to the second chamber: Cooling to nano-kelvin temperatures

to some μW , which is technically hard to achieve.

In the second part of the cooling process we therefore open the confinement of the tweezer by moving its focal point away from the dimple as shown in figure 23. This is accomplished by changing the position of the translation stage by 4.5 mm, which changes the waist of the tweezer at the crossing point from 28 μm to 60 μm . The power in the tweezer and dimple beams is then lowered again until a quasi isotropic confinement is achieved.

In its final state after evaporation and adiabatic opening the crossed dipole trap is then characterised by the following frequencies and depth:

$$\begin{aligned}\omega_{\text{tweezer}}/2\pi &= 3.9 \text{ Hz} \\ \omega_{\text{dimple}}/2\pi &= 5.3 \text{ Hz} \\ U_0/k_{\text{B}} &= 15 \text{ nK}\end{aligned}\tag{35}$$

Such a shallow trap depth is only possible since we are cancelling gravity with the magnetic levitation: The combined potential of the tweezer and gravity would not have a minimum anymore if the tweezer trap depth decreases below $U_{\text{tweezer}}/k_{\text{B}} \approx 1.5 \mu\text{K}$.

During the evaporation process a fraction of the atoms form a Bose-Einstein Condensate, described in the following section.

3.3.6 Bose-Einstein condensation

Bose-Einstein condensation of dilute atomic vapours was first achieved in 1995 [10, 35, 21], a remarkable experimental breakthrough made possible by the precise control over position and movement of atoms. A Bose-Einstein Condensate (BEC) is a mesoscopic quantum object, where all participating particles are bosons and occupy the collective ground state of the system. In the following some key formula for the description of a BEC in a harmonic trap are given, without stressing their derivation. For a more complete introduction the interested reader is referred to the extensive literature that exists on this topic, for example [33, 70, 25].

The Onset of Bose-Einstein Condensation Bose-Einstein condensation is achieved in a trap that is, in most experiments, well approximated by a harmonic potential. The confined gas has a temperature T that defines the de-Broglie wavelength λ_{dB} and a density n . Qualitatively the onset of condensation is reached when the wavepackets of the atoms, which occupy a volume $\sim \lambda_{dB}^3$, start to overlap. In other words, the phase space density

3.3 From the first to the second chamber: Cooling to nano-kelvin temperatures

D must reach a value on the order of one:

$$D = n\lambda_{dB}^3 \sim 1 \quad (36)$$

The phase-space density in a harmonic trap with trapping frequencies $\omega_x, \omega_y, \omega_z$ is given by

$$D = \left(\frac{\hbar\bar{\omega}}{k_B}\right)^3 \frac{N}{T^3}, \quad (37)$$

where $\bar{\omega} = (\omega_x\omega_y\omega_z)^{1/3}$, $\hbar = h/2\pi$ is the reduced Planck constant, N is the total number of atoms, and T is the temperature.

Condensation occurs at a critical temperature T_c , where the occupation of the ground state of the trap becomes macroscopic [33]:

$$k_B T_c = 0.94\hbar\bar{\omega}N^{1/3} \quad (38)$$

This macroscopic occupation of the ground state manifests itself in a prominent peak in the density and momentum space distribution, that is surrounded by the more dilute thermal distribution of the remaining atoms.

The Gross-Pitaevskii Equation and the Thomas-Fermi Regime

Below T_c the density at the center of the trap is high enough for the interactions between the atoms to make an appreciable contribution to the total energy. This additional potential is proportional to the density, $V_{\text{int}}(\vec{r}) = g n(\vec{r})$, where g is the coupling constant. This coupling constant is proportional to the scattering length a , which gives the cross section of an atom in a collision process, $g = a4\pi\hbar^2/m$. These interactions can be treated in a mean field approach described by the Gross-Pitaevskii equation. In the stationary regime the wave function can be written as $\psi(\vec{r}, t) = \phi(\vec{r}) \exp[-i(\mu/\hbar)t]$, where μ is the chemical potential. The density is simply $n(\vec{r}) = |\phi(\vec{r})|^2$. This wavefunction obeys the stationary Gross-Pitaevskii equation:

$$\left[-\frac{\hbar^2}{2m}\Delta + V(\vec{r}) + g|\phi(\vec{r})|^2\right]\phi(\vec{r}) = \mu\phi(\vec{r}) \quad (39)$$

The first term on the left hand side is the kinetic energy, the second term the potential energy due to the trapping potential, and the third term describes the interaction energy.

When the interaction energy is much larger than the kinetic energy the condensate is said to be in the Thomas-Fermi regime, a condition which is

3.3 From the first to the second chamber: Cooling to nano-kelvin temperatures

fulfilled in our experiment. One can then neglect the kinetic energy term in the Gross-Pitaevskii equation (39), leading to a simple spatial profile of the density [17]:

$$n(\vec{r}) = \max\left(\frac{\mu - V(\vec{r})}{g}, 0\right) \quad (40)$$

In the case of a harmonic confinement with trap frequencies $\omega_x, \omega_y, \omega_z$ the trapping potential is given by $V(\vec{r}) = m/2(\omega_x^2 x^2 + \omega_y^2 y^2 + \omega_z^2 z^2)$. The density profile of the condensate then is an inverted parabola. Its maximal extension in x-direction, the Thomas-Fermi radius $r_{TF,x}$ is given by

$$r_{TF,x} = \left(\frac{2\mu}{m\omega_x^2}\right), \quad (41)$$

and equivalently for the other two spatial directions y and z .

Integration over the density profile $n(\vec{r})$ gives the total number of atoms in the condensate N , a readily measurable quantity. In the Thomas-Fermi regime one can therefore determine the chemical potential:

$$\mu = \frac{1}{2} (15aN\hbar^2\bar{\omega}^3)^{2/5} m^{1/5} \quad (42)$$

Free Expansion of a BEC In our experiment we usually cut the trap and let the cloud expand freely before taking a picture of the distribution. The expansion of a BEC in the Thomas-Fermi regime can be described by a scaling theory [26, 58]: The initial parabolic shape of the condensate density distribution $n(\vec{r})$ is stretched along the proper axes of the trap x , y , and z by the factors $b_x(t)$, $b_y(t)$, and $b_z(t)$ respectively:

$$n(\vec{r}, t) = \frac{1}{b_x(t)b_y(t)b_z(t)} \cdot n(\vec{\rho}, 0) \quad (43)$$

Here, $\vec{\rho}$ is the rescaled position vector, $\vec{\rho} = (x/b_x(t), y/b_y(t), z/b_z(t))$.

The global picture that we observe is then the following: Below the condensation threshold a fraction of the atoms are in the collective ground state of the system and form a condensate that is well described by the Thomas-Fermi approximation. The density distribution of this condensed fraction after a free expansion is parabolic. The non-condensed atoms have a gaussian velocity distribution. Both distributions overlap, and the global density distribution is described by a double structure, with the condensate distinctly visible on top of the broader gaussian background. Figure 3.3.6 shows a typical example of a BEC. The projection of the recorded density profile clearly shows the aforementioned double structure.

3.3 From the first to the second chamber: Cooling to nano-kelvin temperatures

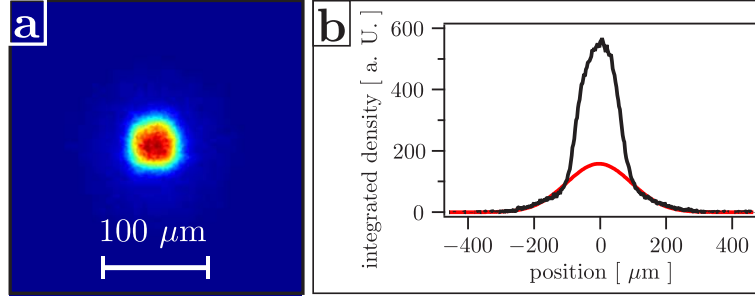


Figure 24: **Typical example of a BEC.** Shown here is an example of a typical BEC in our experiment with $\approx 10^5$ atoms after a time of flight of 150 ms. **a)** The recorded density profile. This density profile is already integrated along the optical axis of the imaging system. **b)** The projection on the horizontal axis (black) together with a gaussian fit of the wings, showing the thermal fraction of the atomic cloud. The double structure is clearly visible.

3.3.7 Delta-kick cooling

At the end of the evaporation cycle in the crossed dipole trap a cloud of about 10^5 atoms is obtained, more than 50% of which are Bose condensed. We estimate the chemical potential in the condensate to be $\mu/h \approx 40$ Hz. The temperature of the thermal fraction is 4 nK. Upon release from the trap the cloud expands and the interaction energy is converted into kinetic energy, which leads to a velocity distribution of the condensate fraction with a maximum velocity of $v_{\text{max}} = 0.3 - 0.36$ mm/s.

With a neat trick, the delta-kick cooling method, it is possible to reduce the velocity distribution even further without any downsides, like the decrease of the number of atoms, for our experiments. A more detailed treatment, as well as a quantum mechanical picture can be found in [9]. Here this technique is explained in a classical picture as shown in figure 25: Initially all the atoms are found around the center of the trap at $\vec{r} = 0$. Upon release, and after the interaction energy between the atoms is fully converted to kinetic energy, each atom travels with its own constant velocity v away from the center. In the following we assume that the center of mass of the cloud does not move during this expansion, which is a requirement fulfilled in our experiment due to the magnetic levitation. When after a time t_{exp} the size of the cloud is large compared to its initial size the dis-

3.3 From the first to the second chamber: Cooling to nano-kelvin temperatures

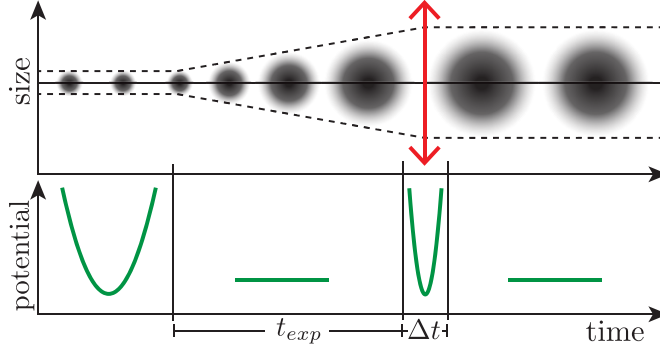


Figure 25: **Delta-Kick Cooling.** On top the size of the cloud, and on the bottom the potential of the trap is indicated. Four stages in the expansion of the atom cloud are shown: Initially the atoms are located in the trap, and the size of the cloud is constant. Once it is switched off (shown as a flat potential line) the cloud expands. Then the trap potential is switched on again for a short time and with a calibrated curvature, which affects the expansion just like a focussing lens renders a diverging beam collimated. In the last stage the potential is off again, and the expansion is stopped.

tance traveled by each atom is to a good approximation proportional to its velocity:

$$r(v) = vt_{\text{exp}} \quad (44)$$

The delta-kick cooling technique now consists of switching the trap on again for a short time Δt . During this time a given atom with velocity v_i and distance from the center $r_i = v_i t_{\text{exp}}$ is subject to a force towards the origin. Assuming a harmonic potential its velocity at the end of this kick is:

$$\dot{r}_i(\Delta t) = v_i (-t_{\text{exp}}\omega \sin(\omega\Delta t) + \cos(\omega\Delta t)) \quad (45)$$

Experimentally it is possible to adjust the trap frequency ω and the length of the kick Δt such that $\dot{r}_i(\Delta t) = 0$. This is the case when

$$\Delta t\omega = \arctan\left(\frac{1}{t_{\text{exp}}\omega}\right). \quad (46)$$

Since equation (46) is independent of the initial velocity v_i it holds true for all atoms, and applying such a kick stops each one in its place.

3.3 From the first to the second chamber: Cooling to nano-kelvin temperatures

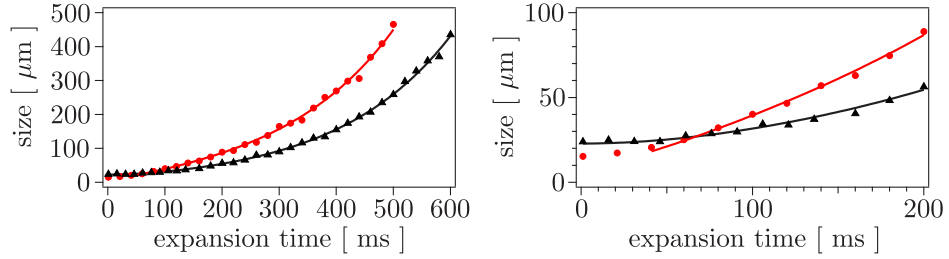


Figure 26: **Free expansion with and without delta-kick cooling.** The size of the cloud, shown here for the y -axis (vertical) is measured with a gaussian fit. The red points indicate the evolution of the size without, and the black triangles with delta-kick cooling. The solid lines are the corresponding fits (see text). The right graph shows a close-up for short expansion times. The expansion time for the data without delta-kick cooling is measured starting from the release of the trap. The fit here starts at 40 ms, when the interaction energy has been transformed into kinetic energy. In the case with delta-kick cooling the expansion time is measured from starting from the delta-kick.

To evaluate the effect of the delta-kick cooling method we release the cloud from the trap and measure its size after different times of flight. The results of such a measurement are shown in figure 26. As explained in section 3.3.4 the magnetic levitation has an expelling curvature, which has to be taken into account when fitting the data. Solving the equation of motion for a harmonic expelling potential with anti-trap frequency $\omega_{\text{lev}} = 2\pi f_{\text{lev}}$ we find for the evolution of the size $\sigma(t)$ of the cloud

$$\sigma(t) = \sqrt{x_0^2 \cosh(2\pi f_{\text{lev}} t)^2 + \left(\frac{v_0}{2\pi f_{\text{lev}}}\right)^2 \sinh(2\pi f_{\text{lev}} t)^2}, \quad (47)$$

where x_0 is the initial size and v_0 is the initial velocity spread.

Using this method we find a reduction of the velocity spread by a factor ~ 2 , from 0.3 – 0.36 mm/s to 0.18 mm/s. We choose $t_{\text{exp}} = 50$ ms, when all the interaction energy is converted to kinetic energy, and $\Delta t = 0.5$ ms. The trap frequencies were adjusted experimentally to give the lowest velocity spread after the delta-kick. We found $\omega \approx 200 \text{ s}^{-1}$, which is in very good agreement with equation (46).

There are two obvious limiting factors, which can explain why not a greater reduction in the velocity spread is achieved. First, the trap is formed

by gaussian laser beams, which only close to their optical axis form an approximate harmonic potential. Second, the initial size of the atomic cloud (RMS size $\approx 10 \mu\text{m}$) is not negligible compared to its size at t_{exp} (RMS size $\approx 30 \mu\text{m}$). The reduction in the velocity spread by a factor two is a compromise we found between these two limiting factors. Nevertheless the result is impressive: With a size of $\approx 30 \mu\text{m}$ and a typical momentum $m_{\text{Rb}} \times 0.18 \text{ mm/s}$ we are only an order of magnitude above the Heisenberg limit. Another way to emphasize the minute velocity distribution is to translate it to a temperature, which gives about 150 pK. The delta-kick cooling completes the preparation of the atomic cloud for our experiments.

3.4 Conclusion

The initial goal of achieving a sample of atoms with a very low velocity spread was achieved via a combination of laser cooling, and forced evaporation in a magnetic and an optical dipole trap. This results in the creation of an ultracold sample of $\approx 10^5$ atoms, more than 50% of which are forming a Bose-Einstein condensate. The chemical potential of the condensate is $\mu/h = 40 \text{ Hz}$, and the temperature of the thermal fraction is 4 nK. Upon release from the trap the interaction energy between the atoms is converted to kinetic energy, such that the cloud expands with a velocity of $0.3 - 0.36 \text{ mm/s}$. With the delta-kick cooling method this velocity spread is reduced by a about factor 2 to 0.18 mm/s . The RMS size of the cloud at this point is $\sigma \approx 30 \mu\text{m}$.

Figure 27 shows the atomic cloud at some exemplary stages of the experimental cycle described in this section.

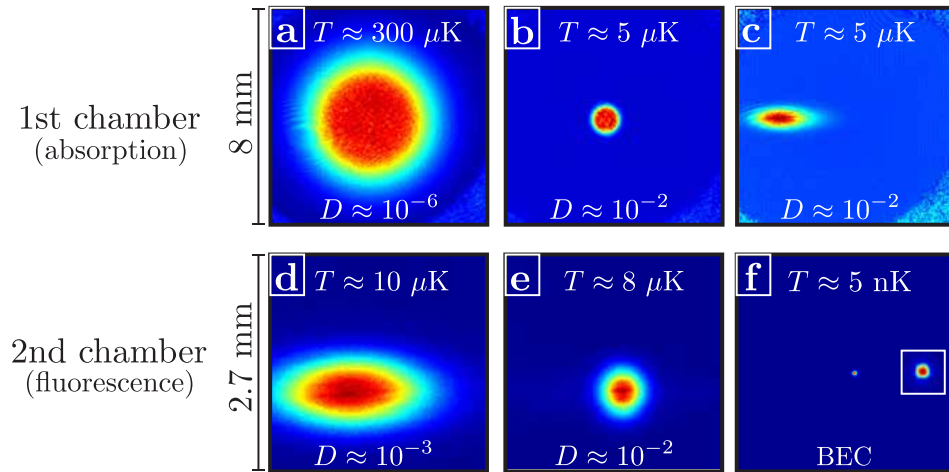


Figure 27: **The atomic cloud at different stages of the experiment.** Each image shows the atomic cloud after a time of flight of 8 ms at different stages of the experiment. The approximate temperature and the order of magnitude of the phase space density D are given. The first row shows absorption images taken in the first chamber directly after loading into the magnetic trap (**a**), after evaporation in the magnetic trap (**b**), and after loading into the tweezer (**c**). The second row shows fluorescence images taken in the second chamber directly after transport (**d**), after loading into the crossed trap (**e**), and after evaporation (**f**). The inset in panel **f** shows the BEC after an expansion time of 150 ms.

4 Optical speckles

In our experiments on wave propagation in disordered potentials the characteristics of said potentials naturally play an important role. Ideally its interaction with the atoms should be completely conservative, meaning that all scattering events are fully elastic. Furthermore the typical length scales on which the potential fluctuates should be small compared with the de-Broglie wavelength, a necessary requirement if one wants to enter into the strong localisation regime (see section 2.6). All these requirements can be fulfilled with an optical speckle potential, whose basics will be discussed in this section. Since the speckle is optical it is furthermore possible to switch the disorder on and off quasi instantaneously on the relevant time scales of the atomic dynamics, and it is possible to regulate the strength of the disorder seamlessly simply by changing the optical power.

Optical speckles have been employed in ultracold atom experiments for roughly a decade now due to the reasons given above, but also because they are comparatively simple to produce, and their statistical properties are well known. Prominent examples include the observation of Anderson localisation in 1D [20], the study of 2D diffusive expansion [98], and transport through a disordered 2D channel [22].²⁷ Recently the observation of 3D Anderson localisation of ultracold atoms was achieved, also using optical speckles [56, 62, 103]. One of these experiments was conducted during this thesis, and will be treated in section 6.

This introduction to speckle potentials is based on [32] and [48] for the general theory describing optical speckles, and [30] for a discussion with a focus more on its application to cold atom experiments. In addition a description of our specific configuration is given.

4.1 A general introduction to optical speckles

A speckle is the interference pattern of many waves with random phases. It can easily be observed by shining a coherent light source, for example a simple laser pointer, on a rough surface. Due to the roughness a random path difference, and consequently a random phase is imprinted on the beam. Another possibility to introduce these random phases, which is used in our experiment, is to shine the laser beam through a glass plate with randomly

²⁷It should be mentioned that there is a second method that can be used to produce a quasi-random potential in cold atom experiments, namely, bichromatic lattices with incommensurate wavelengths. These were for example employed for the observation of 1D Anderson localization, conducted in parallel with the above cited experiment [97].

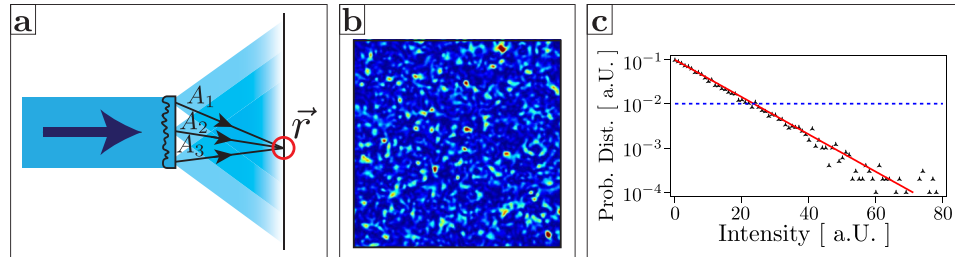


Figure 28: **An idealised speckle setup.** Panel **a** shows how a speckle pattern is created by shining a laser beam through a rough glass plate. Wavelets from different points of the diffusor arrive at a point \vec{r} with complex amplitudes A_k with random phases. Panel **b** shows a numerically generated speckle pattern. The probability distribution of the intensity is exponential, $P(I) = 1/\langle I \rangle \exp(-I/\langle I \rangle)$ as shown in panel **c**. The black points follow a numerically generated intensity distribution, and the red line is a fit. The blue dotted line shows the value $\langle I \rangle$.

varying thickness as shown in figure 28 **a**. In the following it is assumed that this glass plate, the diffusor, has a circular cross section, a constant index of refraction, and is evenly illuminated by the laser.

4.1.1 Intensity distribution

The light incident at one position (x, y) of the diffusor acquires a phase proportional to its thickness $e(x, y)$ at this point,

$$\Delta\phi(x, y) = \frac{2\pi}{\lambda} e(x, y) \cdot (n - 1), \quad (48)$$

where λ is the wavelength of the laser, and n is the refractive index of the diffusor. In our experimental configurations the phase $\Delta\phi$ is in a very good approximation equally distributed over the whole interval $[0, 2\pi[$. Each partial wave is diffracted into an outgoing cone with an opening angle that is determined by the ratio of the wavelength and the average size of a surface structure of the diffusor, much like the angle of the light cone behind a small hole is determined by the ratio of the wavelength and the diameter of the hole. The intensity at a given point \vec{r} can then be thought of as the result of the interference of many partial waves with random phases emanating from different positions of the diffusor. Assigning a complex amplitude $A_k =$

$|A_k| \exp(i\phi_k)$ to each of these partial waves the total amplitude at point \vec{r} then is:

$$A(\vec{r}) = \sum_k A_k = \sum_k |A_k| e^{i\phi_k} \quad (49)$$

This sum describes a random walk of the amplitude in the complex plane, with the steps $0, A_1, A_2$, etc. In the limit of infinitely many point sources on the diffusor it follows from the central limit theorem that the absolute value of the resulting amplitude is normally distributed around zero. It then follows from a probability transformation that the probability distribution $P(I)$ of the intensity $I = |A|^2$ is an exponential,

$$P(I) = \frac{1}{\langle I \rangle} e^{-\frac{I}{\langle I \rangle}}, \quad (50)$$

where $\langle I \rangle$ doubles as the average intensity of the speckle field and the standard deviation of the distribution. Panel **b** in figure 28 shows a numerically calculated speckle field, and panel **c** shows the probability distribution of the intensity, together with a fit of the form of the distribution in equation (50).

Two interesting properties of speckle fields that are advantageous for our experiments are already visible in formula (50): First, the probability to find points of high intensity is exponentially small, meaning that the speckle field is only occasionally accentuated by strong scattering points. Conversely, the probability for low intensities is high. This means that the atoms propagate in a potential landscape that consists mainly of low valleys, and only particles with very low energy can be classically bound, a consideration important for our experiments on Anderson localisation.²⁸ Second, since the standard deviation of the intensity distribution is equal to its mean value the fluctuations of the amplitude of the potential are large. In other words, the speckle is a disorder with a high contrast.

4.1.2 Spatial structure

Information about the spatial structure of the speckle field is contained in the intensity autocorrelation function

$$C_I(\delta\vec{r}) = \langle I(\vec{r})I(\vec{r} + \delta\vec{r}) \rangle, \quad (51)$$

where the brackets $\langle \dots \rangle$ imply statistical averaging over different speckle realisations (see section 2.1).

²⁸The potential felt by the atoms is directly proportional to the intensity of the speckle, as discussed in section 3.3.1.

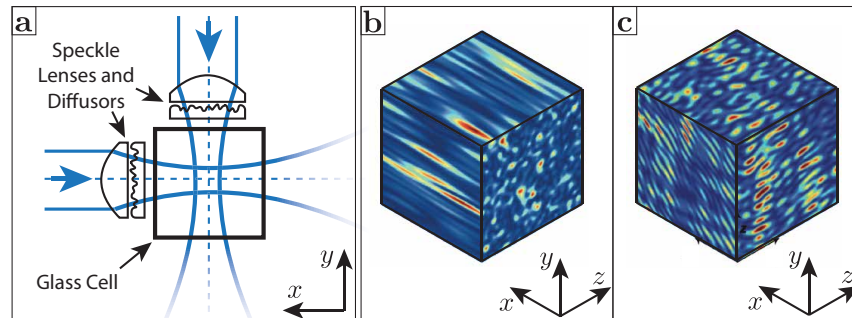


Figure 29: **Schematic setup of the speckle.** Panel a shows the schematic setup of the speckle. In order to increase the maximum optical power incident onto the atoms, and to minimize the speckle grain size and their anisotropy the light is focalised with a lens (see text). To further decrease the anisotropy two independent speckle fields can be superposed: One beam produces highly anisotropic structures (panel b), whereas the coherent superposition of the two beams changes the spatial configuration and decreases the overall anisotropy (panel c).

The transverse and longitudinal size of this autocorrelation function depend on the maximum angle θ under which light can arrive at the point \vec{r} from the diffuser.²⁹ The size of the correlation function $C_I(\delta\vec{r})$ is determined by the displacement $\delta\vec{r}$ it takes to dephase the different complex amplitudes A_k with respect to each other. It turns out that this size is diffraction limited, producing a correlation function that has a transverse extent $\sigma_{\perp} \sim \lambda/\sin(\theta)$, and a longitudinal extent of $\sigma_{\parallel} \sim \lambda/\sin(\theta)^2$ (just like the size of the Airy disk and the Rayleigh length of a diffraction limited focussed gaussian beam). With $\sin(\theta) < 1$ this produces longitudinally elongated structures. The asymmetry $\sigma_{\parallel}/\sigma_{\perp}$ is reduced when the numerical aperture $NA \sim \sin(\theta)$ is increased.

4.2 The speckle configuration in our experiment

The design goal in our experiment was to obtain a speckle potential with small structures and a minimal anisotropy, which are necessary requirements to enable experiments on Anderson localization and to simplify their inter-

²⁹“Transverse” and “longitudinal” are to be taken with respect to the optical axis of the speckle setup.

pretation (see section 6). In order to accomplish this our speckle setup contains several key features, shown schematically in figure 29:³⁰

Additionally to the diffusors the laser light is led through a focalising lens, which is positioned such that its focal point coincides with the position of the atoms. This increases the available optical power shining onto the atoms, and ensures that the angle θ mentioned in the previous section is maximal. As outlined earlier, the latter point is important for a minimal size and anisotropy of the speckle grains.

To further decrease the anisotropy we have the option to superpose two independent speckle fields, whose optical axes form a 90° angle. When the polarisation axes of the two beams are orthogonal with respect to each other the resulting light pattern is the incoherent superposition of the two speckles. In the other case of coherent superposition, when the polarisation axes are parallel, the two speckles interfere with each other. The resulting interference pattern retains the exponential intensity probability distribution of equation (50), but changes the autocorrelation function. It is this coherent superposition that was employed in our experiments on Anderson localization, and a more detailed treatment of this configuration can be found in the thesis of F. Jendrzejewski [55]. We are only pointing out here that the anisotropy of the coherent superposition of two speckles reduces the anisotropy by about a factor 3 as compared to a single speckle field.

During the course of this thesis the speckle setup was completely overhauled. Its characterisation can be found in section 5.3.

4.3 Natural units

An isotropic disordered speckle potential introduces a natural length scale of the system, namely its correlation length σ . From this length scale other units can be derived, namely [64]:

- Wavenumber: $k_\sigma = \sigma^{-1}$
- Momentum: $p_\sigma = \hbar k_\sigma$
- Energy: $E_\sigma = \frac{\hbar^2}{m\sigma^2}$, with m the mass of an atom
- Time: $\tau_\sigma = \hbar/E_\sigma$

³⁰This configuration was developed by F. Jendrzejewski, a former PhD student in our group. Detailed information can be found in his thesis [55]. The success of our setup motivated another group at the LENS in Florence to build an experiment using a very similar speckle setup [103].

4.3 Natural units

These units are the natural and convenient measures when describing the propagation of waves in such a disordered potential. They are employed for example in the code for the numerical simulations described in section 8.6.1, and for numerous qualitative arguments describing the propagation of the atoms.

This being said, the speckle potentials used in our experiments are not perfectly isotropic: In the case of the crossed speckle, used in our explorations of 3D Anderson localization (see section 6), the correlation lengths along the three major axes of the speckle are $0.11 \mu\text{m}$, $0.27 \mu\text{m}$, and $0.08 \mu\text{m}$ respectively. Since they are all of the same order, qualitative arguments using the corresponding natural units, for example the comparison of E_σ with the amplitude of the disorder V_R , could nevertheless be drawn.

For our experiments on Coherent Backscattering and Coherent Backscattering Revival (see sections 7 and 8) a single speckle beam was used, giving very different correlation lengths of $\sigma_\perp = 0.235 \mu\text{m}$ and $\sigma_\parallel = 2.77 \mu\text{m}$. But since the dynamics in these experiments were taking place only within a plane perpendicular to the optical axis of the speckle, the only relevant length scale of the disorder was σ_\perp . Therefore, in these cases, there is no ambiguity as to which natural units to use.

5 Modifications of the experiment

During the course of this thesis several modifications of the experiment were implemented. These modifications were carried out after the experiments on Anderson localization / CBS, and before the experiments on CBSR. The overall goal was to improve stability of already existing capabilities, and to add flexibility for future projects:

- The imaging system around the science chamber was upgraded in order to have diffraction limited imaging. The new system is also flexible and allows two different configurations, one with a high field of view and another with a high resolution.
- The beam line for one of the crossed optical dipole trap beams, the dimple, shares optical elements with one of the new imaging systems. It was therefore completely redone, putting an emphasis on the stability of the setup.
- The whole speckle setup was redone. It now has a dedicated optics table, giving more room and flexibility for future modifications of the speckle.

In addition a remark on the implementation of a procedure to increase the quality of the vacuum using light induced atomic desorption (LIAD) is made at the end of the chapter.

Not treated is the installation of a magnetic shielding around the science chamber to increase the stability of the magnetic field at the position of the atoms. This will become important for future works, and has no impact on the description of the CBSR experiments. A full characterisation of the performance of the magnetic shielding has therefore not been carried out yet at the moment of this writing.

5.1 Imaging system

There are three camera systems installed in our experiment: One to take images in the first, and two for imaging in the second chamber. All three cameras are *EMCCD Hamamatsu C9102*, with 1000×1000 pixel, each with a size of $8 \times 8 \mu\text{m}^2$. These cameras work in conjunction with an objective that transports the light from the focal plane to the CCD chip.

For fluorescence imaging (see section 3.1) that we use in the science chamber a spherical wavefront emanating from a point-like object first has to be transformed into an ideally flat wavefront. In order to achieve this and

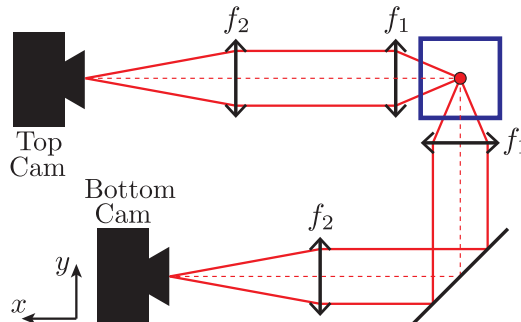


Figure 30: **Schematic overview of the science chamber imaging system.** The beam paths for the top and the bottom imaging systems are shown. Both are centered on the center of the glass cell (blue square), where the atoms are situated (red point).

obtain diffraction limited imaging while having a high numerical aperture ($NA \approx 0.4$) it is necessary to take into account the aberrations induced by the wall of the glass cell that the light coming from the atoms has to pass. This was not the case for the old imaging systems, and it was therefore decided to upgrade the two around the science chamber. The design process was carried out by Valentin Volchikov, who was then a visiting PhD student and is now working as PostDoc in our group, together with Raymond Santoso, a Master student intern. It took inspiration from the diploma thesis of T. Ottenstein, and detailed information about the design that is qualitatively similar to ours can be found therein [85].

The general setup of the imaging system around the science chamber is shown in figure 30. In the following we will concentrate on the top cam imaging system, which is nearly identical to the bottom system. The only exception is that the fluorescence light in the bottom imaging system is once reflected by a (dichroic) mirror. The optical access used for the bottom imaging is shared with the dimple beam setup, which will be described in the next section 5.2.

The glass cell is made of 3 mm thick Vycor glass (refractive index $n = 1.46$) and measures 30 mm on each side.³¹ Simulations with the program Oslo were carried out to adapt the design of [85] to our specifications.³² As

³¹This is the outside length of the glass cell. This means that the atoms at the center of the glass cell are 15 mm away from the outside surfaces.

³²Due to mechanical constraints the maximum diameter of our lenses is smaller, and our

in [85] a combination of three lenses is used to collimate the light coming from the atoms and correct for the aberrations introduced by the glass cell. The numerical aperture of this system is $NA = 0.4$. The lenses were built to our specifications by *Lens-Optics*, and are made of SF11 glass (refractive index $n = 1.77$) with a 780 nm anti-reflection coating. Figure 31 shows the technical drawings of this lens system, together with the mount used to hold them together and position them close to the glass cell. Not shown is the second part of the mount which holds the lens that focusses the light onto the CCD chip of the camera (f_2 in figure 30). In order to have the choice between either a high field of view or a high resolution it was decided to order lenses with two different focal lengths f_2 and design the mount such that one can easily switch between the two. The lenses are doublets from *Melles Griot*, *MG01LA0795* ($f = 300$) and *MG01LA0523* ($f = 100$). With these two different lenses we obtain a magnification of roughly 10 and 3 respectively.

At the time of writing this thesis we have only been using the low magnification, high field of view imaging. We found the pixel size to be $2.71 \mu\text{m}$, which is in agreement with the expected magnification, and translates to an observable surface in the focal plane of $2.7 \times 2.7 \text{ mm}^2$. This pixel size was determined experimentally by measuring the (vertical) center of mass position of the cloud in the crossed dipole trap y_0 , and comparing it to the position y_1 after a free fall of duration t . The difference in position $\Delta y = y_0 - y_1$, initially measured in number of pixels, must equal to $gt^2/2$, where $g = 9.81 \text{ m/s}^2$ is the gravitational constant.

5.2 Dimple beam setup

As explained in section 3.3.3, in the science chamber the atoms are held in a crossed optical dipole trap, consisting of a horizontal beam (tweezer), and a vertical beam (dimple). For both beams of the crossed dipole trap a single Ytterbium laser (20 W @ 1070 nm, from *Keopsys*) is used, and it is in this trap where the evaporation ramps leading to the BEC are performed.

The dimple beam uses the optical access port and part of the objective of the bottom imaging system. As laid out in the previous section, an update of both imaging systems of the science chamber was performed to achieve diffraction limited imaging, and it was therefore decided to revamp the whole dimple beam line. A characterisation of the old setup can be found in the PhD thesis of F. Jendrzejewski [55] and A. Bernard [19]. The first part of

glass cell is thinner.

5.2 Dimple beam setup

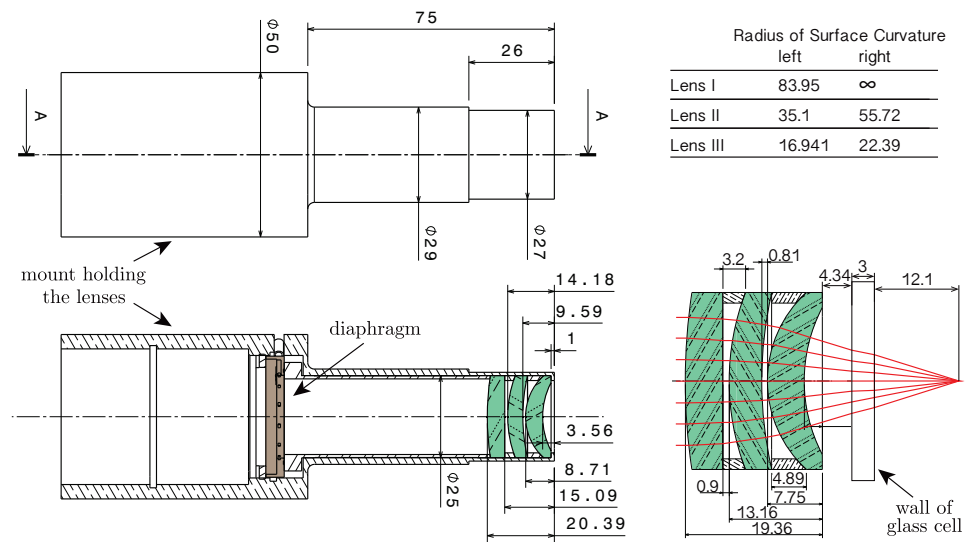


Figure 31: **Technical drawings of the top cam imaging system.** The system of lenses shown here (shaded green) correspond to the one denoted f_2 in figure 30. A diaphragm (shaded brown) can be used to decrease the effective numerical aperture of the imaging system in order to increase the depth of field.

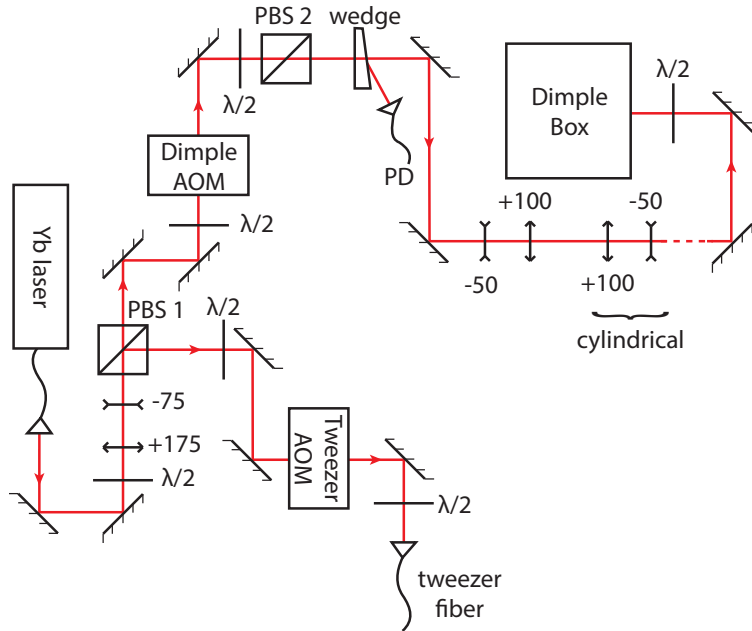


Figure 32: **The dimple beam line.** Shown here is the beam line of the dimple, starting from the output fiber of the Ytterbium laser, up until the “dimple box”. About 20% of the total power are diverted to the tweezer by a polarising beam splitter (PBS 1). Several telescopes, including a cylindrical one, are used to prepare the beam in its desired shape before entering the dimple box. Also included is the beginning of the path of the tweezer. For the missing part of the tweezer beam path, see figure 19.

the new dimple beam line is shown in figure 32, and the second part up until the science chamber in figure 33. This second part shares optical elements with the bottom imaging system and is contained in a single housing that is shown in figure 33 and will be referred to as the “dimple box”.

5.2.1 Design considerations

Stability of the new setup Great care was taken to achieve a good stability of the system. Whereas with the old setup it was necessary to adjust the dimple on a nearly daily basis to optimise its crossing with the tweezer we now don’t need to touch it for several weeks without losing the alignment. Three key changes led to this improvement in stability:

5.2 Dimple beam setup

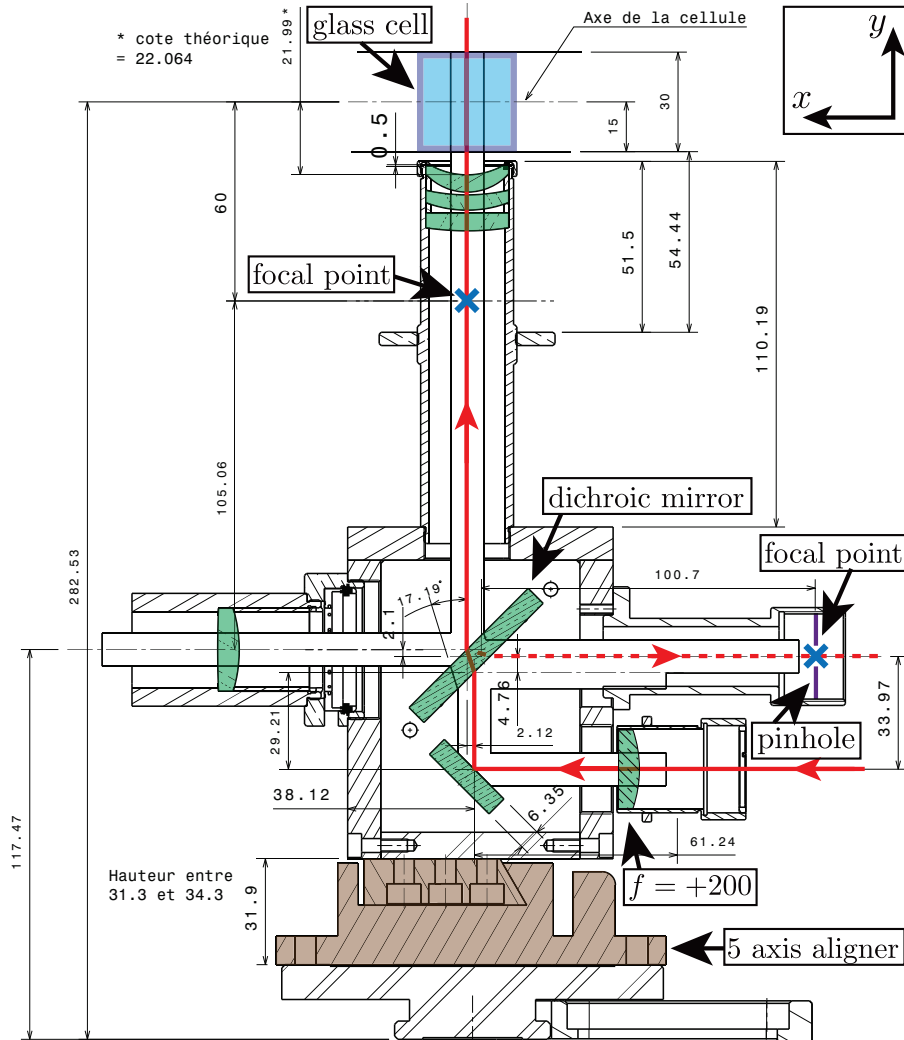


Figure 33: **The dimple box.** A technical drawing showing the dimple box, which combines the last optical elements of the dimple beam line as well as those of the bottom imaging system. This drawing was provided by André Guilbaud from the institute’s mechanical workshop, who manufactured this setup. The beam path of the dimple is marked in red, and the optical elements (lenses and mirrors) are marked in green. Before the dimple box the beam is collimated. Upon entering it is focalised by a $f = +200$ lens, and its focal points are indicated with blue crosses. A small fraction of the beam is reflected by a dichroic mirror, and is used to align it with respect to the dimple box. In order to precisely position the setup it is mounted on a 5-axis aligner, shown in brown. The glass cell, which contains the atoms, is shown in blue.

- The fiber outcoupler coming from the Ytterbium laser had degraded, resulting in a considerable part of the total beam power being dumped into it. This left less power for the dimple and the tweezer, but also led to substantial heating of the outcoupler.
- As much as possible of the beam path was tubed. This prevents poyn-ting fluctuations of the beam due to air currents, and dust settling on the optical elements.
- Most of the optical elements shown in figure 32 were shielded from the surroundings by a plastic box. This again prevents air currents, but also serves to decrease temperature fluctuations. Finally it is a safety measure to protect the eyes of PhD students.

Servo-loop In order to regulate the power that enters into the dimple and the tweezer beams, typical PI feedback loops using Acousto Optical Modulators (AOM) in conjunction with photo-diodes (PD) are employed. These are shown in figures 19 and 32 (“Dimple AOM” and “Tweezer AOM”). The efficiency of the type of AOM used for the servo-loops of both dimple and tweezer depends on the input polarisation of the beam, and each is therefore preceded by a $\lambda/2$ plate.

To monitor the power in the beam a small fraction is diverted towards a photo-diode (“PD”) using a glass prism (“wedge”). The reflection coefficient of the wedge depends on the polarisation of the incoming beam. We observed an instability of the output polarisation of the AOMs, which we attribute to a heating effect of the AOM crystals. Therefore a polarising beam splitter (“PBS 2”) is put before the wedge, which cleans the polarisation. Fluctuations of the polarisation of the beam are transformed into fluctuations of the beam power passing the PBS, but these fluctuations are corrected by the subsequent servo loop.

A similar setup is used for the servo loop of the tweezer.

Alignment of the new setup Another key point in the conception of the last part of the dimple beam line was to ensure a good alignment of the dimple beam with respect to the optical axis of the bottom imaging system and the magnetic coils of the levitation:

- Since the position of the tweezer-dimple crossing determines the position of the atomic cloud it is paramount that this position coincides with the optical axes of the top and bottom imaging systems around the science chamber. A deviation would lead to a deterioration of the

image resolution. To ensure this alignment we installed a pinhole that is positioned at the conjugate focal point of the bottom imaging triplet (see figure 33). If the dimple beam can pass this pinhole we are sure that it is also on axis with the bottom imaging system.

- The atoms are levitated in a magnetic gradient field, which is produced by pairs of coils built symmetrically around the vacuum glass cell (see section 3.3.4). These coils have a well defined geometric center, where the performance of the levitation is expected to be best. Since the (initial) position of the atoms is defined by the crossed dipole trap between the tweezer and the dimple, it is crucial that both meet as close to this center as possible.

In the new setup geometrical constraints were used to align the tube containing the last optical elements of the dimple with the levitation coils: The coils are held in a housing with a vertical hole along its symmetry axis. Attached to the dimple tube is a ring with a diameter 1 mm smaller than the diameter of this hole. The tube can then only enter the hole if it is centered better than 0.5 mm with respect to the symmetry axis of the levitation coils. Additionally, an even finer alignment was achieved by centering this ring precisely in the hole using the 5-axis aligner, on which the dimple box is mounted. Provided that the dimple beam passes the glass cell vertically we can therefore assume that it too is centered with an accuracy better than 0.5 mm.

Heating in the crossed dipole trap During the construction of the dimple beam line we observed a high loss rate of the atoms in the crossed optical dipole trap, with a lifetime of only about 2-4 seconds.³³ Initially a vibration of the tweezer or the dimple beam (“pointing fluctuations”) was suspected as a parametric heating source of the atoms [6, 45], and we went to great lengths to verify the mechanical stability of the setup.³⁴ But the loss rate was eventually determined to be due to heating induced by interferences between the dimple and the tweezer beams, as it can be completely eliminated by rotating the polarisation of the dimple beam such that the polarisation of both beams are orthogonal with respect to each

³³The lifetime of the atoms just in the tweezer was found to be 20-25 seconds, which we assume to be the limit due to collisions with the background gas.

³⁴Intensity fluctuations can also lead to heating. During the course of these investigations we therefore also verified the proper working of the intensity lock of the dimple and the tweezer.

other. To turn the beam polarisation a $\lambda/2$ plate is installed between the wedge of the servo-loop and the dimplebox (see figure 32).

The Ytterbium laser that we use as a source for both the dimple and the tweezer beam has a spectral bandwidth of the order of some MHz, which translates into a coherence length of less than a millimeter. Overlapping the two beams when their path length difference is larger than this coherence length should lead to interference fringes that change too rapidly for the atoms to follow. They would then experience an averaged potential and not be subject to any heating.

The difference in the path length of dimple and tweezer is about a meter, and therefore much larger than the coherence length. The fact that we still observe heating may be explained if the laser spectrum is not continuous, but is composed of many discrete peaks. Coherent superposition of the dimple and the tweezer would then be possible not only within one coherence length, but at repeating intervals of the path difference.³⁵

5.2.2 Characterisation of beam shape and trap frequency

In the old setup the dimple beam had an anisotropic shape at the position of the atoms, with waists $\omega_x \approx 180 \mu\text{m}$ and $\omega_z \approx 90 \mu\text{m}$ [55]. Since the dimple beam waist in x-direction is much larger than that of the tweezer (the waist of the tweezer is on the order of some tens of microns) a practically spherically symmetrical trap can be obtained by choosing the appropriate power ratio in tweezer and dimple. An additional advantage is that small changes of the relative alignment between dimple and tweezer in this direction don't have a big effect on the characteristics of the trap.

For the new setup we tried to recreate a dimple beam with the same characteristics. This would allow us to re-use the evaporation ramps of the old setup, which we knew were working well (the performance of the evaporation in the old setup is detailed in [55]). An additional constraint in the planning was that the dimple beam should enter the glass cell well collimated, in order not to be sensitive to uncertainties in the vertical position of the atoms.

Direct measurements of the dimple beam characteristics As shown in figure 32, starting from the fiber coupler with a measured isotropic waist of $1.2 \pm 0.1 \text{ mm}$ the laser beam passes several telescopes, including a cylindrical one, to shape the beam into an anisotropic gaussian profile. The beam

³⁵In order to have an intensity-noise limited life time of 2-4 seconds fluctuations of the order 10^{-3} to 10^{-4} are sufficient.

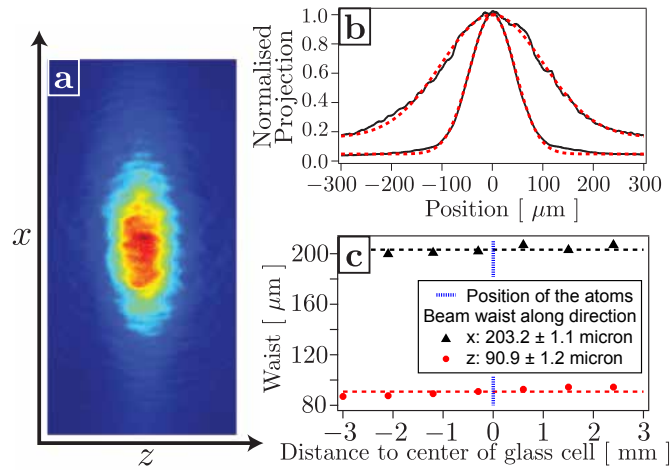


Figure 34: **Characterisation of the dimple beam shape.** A test setup to measure the dimple beam characteristics was built next to the science chamber. It included the whole and unchanged beam path. To simulate the vacuum chamber a piece of glass of equal thickness and material was placed above the dimple box. Panel **a** shows a typical image obtained. The tweezer would pierce the dimple beam parallel to the z -axis. **b** To extract the waists the image is projected onto the x and z -axis (black), and fitted by a gaussian (red). **c** Waists along x and z -axis for different distances between the imaging system and the lens system of the dimple box. The blue vertical line at zero indicates the center of the glass cell, where the tweezer and therefore the atoms would be.

waists were verified to have the expected values by directly measuring the dimple beam shape with a camera at several points along the beam line. At the input of the dimple box (see figure 33) the measured beam waists are $\omega_{\text{vert}} = 840 \mu\text{m}$ and $\omega_{\text{hori}} = 1390 \mu\text{m}$. The beam is then focalised by a lens with focal length $f = 200 \text{ mm}$, which is positioned such that the focal point coincides with the focal point of the imaging lens system (marked by a blue cross in figure 33). This lens system then collimates the beam, so that its shape stays constant while passing through the glass cell. An image of the beam shape at the position of the atoms and a measurement verifying its collimation is shown in figure 34. We measure a waist of the dimple beam at the position of the atoms of $\omega_x = 203.2 \mu\text{m}$ and $\omega_z = 90.0 \mu\text{m}$. The beam within the glass cell is well collimated at least $\pm 3 \text{ mm}$ around the position where the atoms are expected.

The maximum total power arriving at the atoms in the dimple beam is $\approx 7.4 \text{ W}$. Using the measured waists ω_x and ω_z this translates into a maximum trap depth of $U_0/h \approx 210 \text{ kHz}$, where h is the Planck constant. As a comparison, the roughly 2 W coming from the tweezer, focalised into a minimal waist of $28 \mu\text{m}$ has a maximum trap depth of $U_0/h \approx 4.9 \text{ MHz}$.³⁶

Measurements of the dimple trap frequencies A final characterisation was carried out by measuring the trap frequencies of the dimple. To do this a cloud of atoms was held in the crossed trap, with the power in the dimple beam set to a specific value P . With a pulsed magnetic gradient field that exerted a brief force in the z -direction, an oscillation of the center of mass of the cloud in the trap was induced. After an oscillation time t the trap was switched off, and the position of the cloud after a time of flight was recorded. Two examples of such recorded oscillations are shown in figure 35. According to equation (29) the trap frequency ω is proportional to the square root of the power P . Figure 35 also shows the measured dimple trap frequencies as a function of the total power in the beam, fitted by the function $A\sqrt{P}$. The measured slope gives $A = 64.5 \pm 1.2 \text{ s}^{-1}\text{W}^{-0.5}$. In order to compare this slope with the theoretical prediction formula (28) for the trap depth has to be changed for an anisotropic beam shape with waists ω_x and ω_z :

$$U_0 = -\frac{3c^2}{\omega_a^3 \omega_x \omega_z} \frac{\Gamma}{\delta} P \quad (52)$$

³⁶Taking into account the respective beam waists, the maximum trap depths of dimple and tweezer correspond to temperatures of $\approx 4 \mu\text{K}$ and $100 \mu\text{K}$ respectively.

5.3 Speckle setup

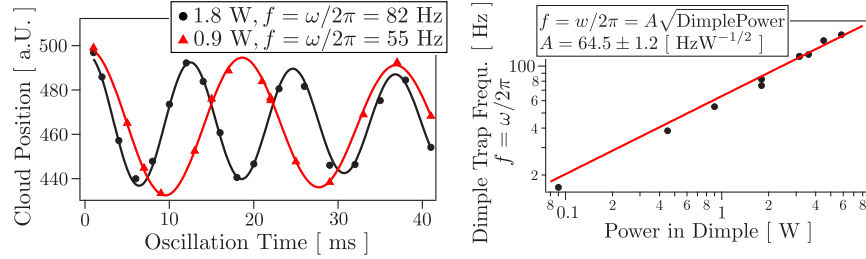


Figure 35: **Dimple trap frequencies.** The left hand graph shows two examples of the center of mass oscillations of the atomic cloud in the crossed optical dipole trap. The fits used are exponentially damped sine curves. For the black curve the power in the dimple beam is 1.8 W, and for the red curve the power is 0.9 W. The right hand graph shows the measured trap frequencies $f = \omega/2\pi$ as a function of the power P of the dimple beam, together with a fit, $f(P) = A\sqrt{P}$.

Together with equation (29) this predicts a slope A of $76.9 \text{ s}^{-1}\text{W}^{-0.5}$, when using the independently measured waists $\omega_x = 203.2 \mu\text{m}$ and $\omega_z = 90.9 \mu\text{m}$, which is in qualitative agreement with the measured slope given above.

5.3 Speckle setup

The optical speckle is a central part of our experiment, as it provides the disordered potential wherein the atoms are propagating. A theoretical introduction to speckles was already given in section 4, and in this section the setup we are using is presented. A previous configuration, detailed in the theses of A. Bernard and F. Jendrzejewski [19, 55], was built during the construction of our experiment, which was used to perform the experiments of Anderson Localisation and Coherent Backscattering. This setup, albeit working well, was limiting in the long run as it was lacking flexibility: Since future experiments will utilise another laser with a different wavelength we decided to revamp the existing setup completely. More precisely, the wavelength of the laser currently used for the creation of the speckle is 532 nm, which provides a far blue detuned repulsive potential (see section 3.3.1). We are currently working on implementing a laser with a tunable wavelength around 780 nm, which would allow us to change from attractive to repulsive potentials, and to work with disorder strengths that depend strongly on the spin-state of the atoms.

A whole optics table is now dedicated to the preparation of the laser beams for the speckle, with enough place to accomodate these two lasers, and with the flexibility to easily change between them. In the following the new setup is presented, which creates an anisotropic disordered potential configuration and was used in our experiments on Coherent Backscattering Revival. It is similar to the old configuration used for our studies of CBS (described in section. A crossed speckle with a reduced anisotropy as used in our experiments on Anderson Localisation is foreseen and can easily be implemented. After the presentation of the setup the characterisation of the crucial properties of this new configuration, the auto-correlation function of the speckle field, its temporal stability, and the intensity shining onto the atoms will be given.

5.3.1 Setup of the speckle

The new speckle setup was installed on an own dedicated optics table, which provides enough space to be much more flexible than the previous configuration. This table is situated close to the science chamber over the translation stage. To dampen any possible mechanical noise or vibration Sorbothane sheets³⁷ were placed between the supporting feet and the table. At the time of writing there are two lasers installed, a Verdi (VerdiTMV-18, 18 W @ 532 nm), and a Toptica (TA pro, 780 nm @ 1.1 W). For all experiments described in this thesis the far blue detuned light from the Verdi was used, whereas the Toptica laser with a frequency close to resonance of the atoms will be necessary for future experiments.

A schematic drawing of the new speckle setup, not including the Toptica laser, is shown in figure 36. In order to ensure a well defined and know polarisation axis the laser beam is first led through a glan. To switch it on and off, to regulate the power, and to reduce intensity noise a servo loop comprising an Acousto-Optical Modulator (AOM) in connection with a photo-diode is used. The second order reflection of a wedge, which separates roughly 4% of 4% from the total power, is directed onto this photo diode. The beam waist, which initially measures 1.1 mm, is enlarged by two telescopes to a final waist of ≈ 12 mm. A compromise has to be made here: Ideally one would like to have a homogeneous illumination of the diffusor in order to obtain very small speckle grains. A quasi-homogeneous illumination can be approximated by having a very wide (larger than the 1-inch diameter of the diffusor) laser beam incident on the diffusor. But this would let only a small

³⁷Thorlabs product number SB12B, with a thickness of 1/4 inch.

5.3 Speckle setup

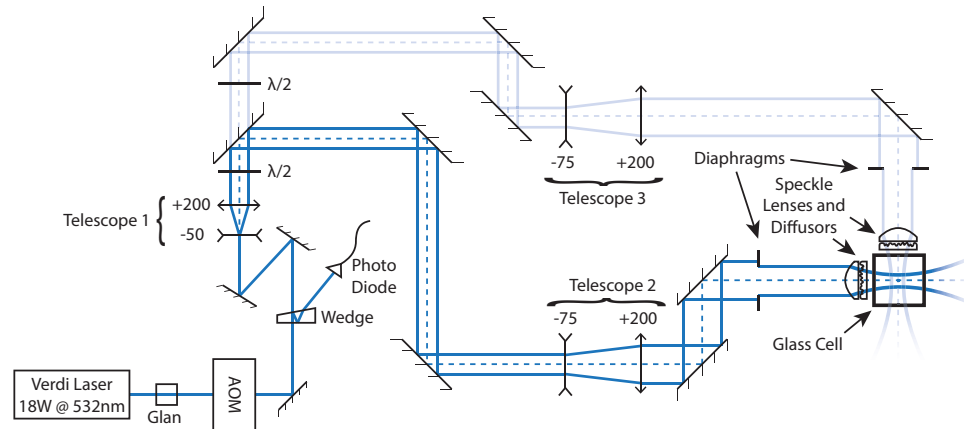


Figure 36: **Setup of the speckle.** For the speckle a Verdi Laser (18 W @ 532 nm) is used. To ensure a very well defined and known initial polarisation the beam is first led through a glan. A servo loop using an AOM in conjunction with a photo diode is employed to enable rapid switching of the laser power, its regulation to a set value, and to reduce intensity noise. Before reaching the diffusor the beam is magnified by two telescopes to a final waist of ≈ 12 mm. This is a compromise between wanting a homogeneous illumination of the diffusor, while still having a large fraction of the total power shining onto the atoms. With a diaphragm the effective numerical aperture of the speckle, and therefore its autocorrelation function, can be regulated. This setup can shine two independent speckle fields onto the atoms, both of which are indicated here. For the main results of this thesis only one arm was used (darker blue).

part of the total power pass to the atoms, whereas the rest is blocked by the finite aperture of the lens / diffusor. A waist of 12 mm is a sweet spot, taking into account both requirements. Nevertheless, the first (Telescope 1 in figure 36, magnification factor 4) can be easily exchanged if a different final beam waist incident on the diffusors is desired. At the moment of writing this manuscript we are only using one speckle arm as opposed to the crossed speckle configuration, and all the beam power is therefore diverted into this arm.³⁸ The beam is then enlarged a second time by a factor ≈ 2.7 to a final waist of about 12 mm.

We use standard broadband dielectric mirrors³⁹, which have a reflection coefficient of $\geq 99\%$ for both 532 nm and 780 nm. For the lenses a custom double anti-reflection coating from CVI Melles Griot was applied to uncoated Thorlabs lenses. The reflection coefficients of the broadband mirrors and the theoretical transmittance of the lenses are shown in figure 37. Both together ensure that a maximum of optical power can reach the atoms.⁴⁰

Finally, the light hits an aspheric lens and the diffusor.⁴¹ In order to have the focal point of the aspheric lens coincide with the position of the atoms at the center of the glass cell its flat face must be positioned ≈ 1.5 mm away from the glass cell. The thickness of the diffusor was therefore reduced from 3 mm to 0.5 mm by the institute's optics workshop.

We measured that a maximum power of 8.6 W exits the diffusor. The inner and outer surface of the glass cell each reflect about 4%, so that the maximum power shining onto the atoms is ≈ 7.9 W.

5.3.2 Characterisation of the speckle

Since the speckle is a crucial part of our experiment a considerable amount of time was spent to properly characterise the properties of the new setup. In particular we were looking into the auto-correlation function and the stability of the speckle field. To do so, the lens and the diffusor at the end of the beam line were installed such that a measurement setup could be

³⁸Optionally the beam can be divided using a polarising beam splitter and fed through two arms. This configuration was so far only used with the previous setup for our experiments on Anderson Localization.

³⁹Thorlabs coating E02.

⁴⁰It has to be noted that the anti-reflection coating was optimised for the N-BK7 substrate, which is used for all the lenses except for the last one just before the diffusor. This lens is made of a different substrate (B270). It was verified experimentally that the anti-reflection coating still works well.

⁴¹The lens is a plano-convex aspheric (Thorlabs ACL2520) with a nominal focal distance of 20 mm.

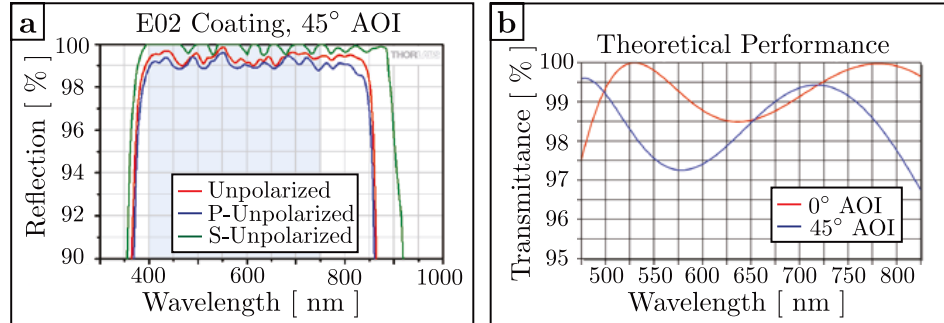


Figure 37: **Reflection and transmission coefficients.** Panel **a** shows the reflection coefficients of Thorlabs dielectric broadband mirrors with E02 coating. This image was taken from the Thorlabs catalogue. In panel **b** the theoretical transmittance of the custom double anti-reflection coating on N-BK7 substrate from CVI Melles Griot is given. Both work well for 532 nm and 780 nm light.

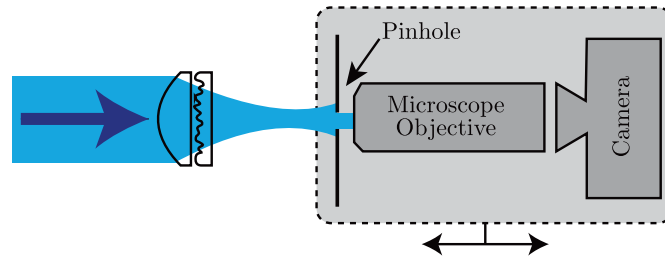


Figure 38: **Setup to measure the spatial structure and stability of the speckle.** The light coming from the focalising lens and the diffuser is first fed through a pinhole to avoid parasitic reflections on the inside of the microscope objective. The objective is necessary to be able to resolve the small scale structures of the speckle, which are on the order of $0.1 \mu\text{m}$. The pinhole, the objective, and the camera are mounted on a computer controlled translation stage that can move the ensemble parallel to the optical axis of the speckle system. The camera can either take one image, or it can take a rapid succession of images. The latter mode is used to either verify the stability of the speckle field (translation stage is fix), or in conjunction with the moving translation stage to reconstruct a 3D image of the speckle field.

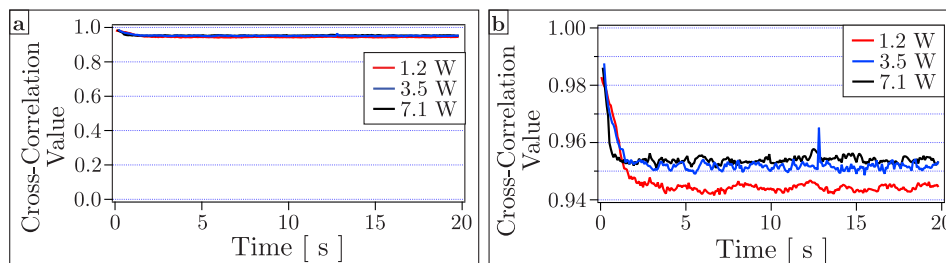


Figure 39: **Stability measurement of the speckle field.** Using a series of images the stability of the speckle field was measured by calculating the cross-correlation with a reference image. This reference image is the one recorded just after switching on the speckle beam. The value 1 corresponds to perfect correlation, and lower values indicate a change of the speckle field. This measurement was repeated for three different values of the beam power, as measured behind the diffuser. Panel **a** and **b** show the same data using different scales on the y -axis.

mounted where usually the atoms would be, as shown schematically in figure 38: Since the transverse spatial structures of the speckle field have a size of the order of $0.1 \mu\text{m}$, much too small to be resolved directly by the camera, it must first be magnified by a microscope objective. The light behind the focal point of the lens-diffuser is strongly diverging, which would lead to reflections inside of the objective. In order to avoid these most of the beam is blocked by a $50 \mu\text{m}$ diameter pinhole, placed in front of the microscope. It has the additional practical advantage of serving as a reference point when adjusting the focal plane of the microscope. The magnified image of the speckle is then detected with a camera. The ensemble of pinhole, objective, and camera can be moved along the optical axis of the system to measure the spatial structure of the speckle field as a function of the distance from the lens / diffuser. The camera can be operated in two modes, either taking a single, or a rapid series of images.⁴² The latter mode was used with a fixed position of the translation stage to verify the stability of the speckle field over time, or with the translation stage moving to obtain the full 3D autocorrelation function of the speckle.

⁴²The maximum frame rate of this camera is 12.7 fps.

Stability of the speckle field In our experiments it is paramount that the speckle stays constant during the propagation time of the atoms since fluctuations either in its amplitude, or in its spatial configuration can lead to decoherence, and therefore to the suppression of localization. Unsteadiness of the disorder amplitude is caused by intensity noise of the laser beam, which in our setup is suppressed by the servo loop. Possible reasons for changes of the spatial configuration of the speckle are poynting fluctuations of the laser beam, mechanical noise affecting the optical components (mirrors and lenses), and heating effects. Poynting fluctuations can be induced by air currents in the beam path, and we therefore closed the whole beam line off from the environment. Great care was taken to achieve a mechanically stable setup that would prevent vibrations, and finally elements heating up due to the beam being dumped on them were placed such as not to influence the beam line.

To verify the stability of our setup the following procedure was used: The camera took a series of images with a frame rate of 12.7 fps for about 20 seconds. While the camera was already recording we switched on the speckle using the AOM. In this way we were sure to capture any eventual effects happening right after the switch-on of the laser beam.⁴³ The first image in the series that showed the speckle, that is, the first one recorded after the speckle laser had been switched on, serves as the reference to which all following images were compared. The cross-correlation between the reference and all the other images was calculated using the Matlab *normxcorr2* routine. This function returns values ranging from -1 to 1, with 1 corresponding to perfect correlation.

Figure 39 shows the result of these measurements for three different powers of the laser beam (measured behind the diffusor). An initial decrease of the cross-correlation value lasting about 2 seconds is observed, after which it stays constant at around 0.94-0.96. It is not entirely clear at this point what causes this change of the speckle field, but the time scale of two seconds and the fact that later the cross-correlation stays constant suggests heating by the laser beam as cause. To put this decrease of the cross-correlation value into perspective we compared two numerically calculated independent speckle configurations in the same manner, and found the value to lie between 0.20 and 0.24. We therefore assess that the observed change of the speckle is very small.

⁴³Due to the limiting frame rate of our camera we were not able to observe any eventual changes of the speckle at the millisecond to 10-millisecond scale.

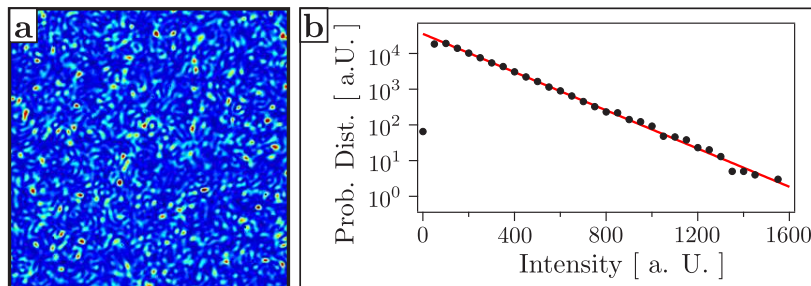


Figure 40: **Experimental image of a speckle.** Panel **a** shows an experimentally obtained image of the speckle. Values of high intensity are yellow to red, and low intensities are painted blue. In panel **b** the intensity distribution of this image is plotted, together with an exponential fit.

Intensity distribution and spatial structure of the speckle field

Figure 40 shows an image of a speckle realisation obtained in the way described above. It also shows the experimental confirmation of the exponential intensity distribution, which was already introduced theoretically in the introduction of this chapter (compare with figure 28 and equation (50)). The deviation from the exponential form for very low intensities in panel **b** is due to the finite resolution of the imaging system used to measure the speckle.

By taking images like this for different distances between the camera and the diffuser the 3-dimensional speckle field can be recorded. This is shown in panel **a** of figure 41: The anisotropy of the speckle grains is clearly visible, and is quantified by calculating the autocorrelation of the speckle field. Panel **b** shows the longitudinal and the transverse plot of this autocorrelation function of the experimentally measured speckle. As laid out in section 4 the longitudinal profile is well approximated by a lorentzian, and the transverse profile by a gaussian. We use these functions to fit and extract the longitudinal and transverse correlation lengths, finding the longitudinal FWHM of the speckle to be $\sigma_{\parallel} = 2.77 \pm 0.2 \mu\text{m}$ and the transverse RMS $\sigma_{\perp} = 0.235 \pm 0.007 \mu\text{m}$.

5.4 *Vaccum / LIAD*

The atomic cloud is held in a vacuum of extremely low pressure, on the order of $\sim 10^{-11}$ mbar, which is necessary to ensure that it is well isolated from the environment. A limitation is the remaining background pressure, which

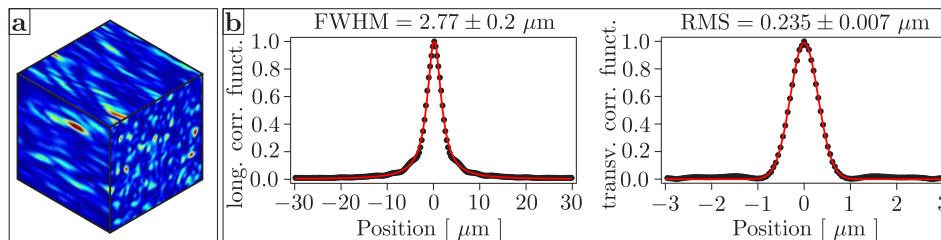


Figure 41: **Autocorrelation of the speckle field.** Panel **a** shows a portion of the experimentally obtained speckle field. From this data one can calculate the autocorrelation function: The longitudinal and transverse speckle autocorrelation functions are shown in panel **b** (black points), together with a fit (lorentzian and gaussian, respectively). Note that the scales of the position axes differ by a factor 10, and that the longitudinal correlation function is much broader than the transverse.

is due to atoms and molecules thermalised to the ambient temperature of about 300 K. Since their thermal energy is very high compared to the depth of the trapping potential used to confine the atoms, a collision between a background gas particle and an atom in the cooled cloud leads to the loss of the atom from the ensemble. To maintain a low pressure several vacuum pumps are installed in different places on our experiment (see figure 11 and [19] for more details on the design of the vacuum system).

In addition, we illuminate the glass chamber in which our experiments take place every night with energetic blue light.⁴⁴ This leads to a cleaning of the inner surface of the glass cell from any rubidium atoms that have stuck to it over the course of a day. This effect is known as Light Induced Atomic Desorption (LIAD). Even though the exact mechanism(s) by which it works are still not fully understood, experimental characterisations exist (see for example [61] for an investigation with parameters very close to our setup).

Before having implemented the LIAD method the lifetime of our atoms in the science chamber had decreased down to ≈ 10 seconds. After having illuminated the glass cell with the energetic light the lifetime went up to 20-30 seconds. We attribute this dramatic increase in lifetime to the fact that during the experimental cycle a beam of atoms emanating from the oven directly hits the glass cell of the science chamber and pollutes its surface. For

⁴⁴To produce the light we are using LEDs from *Roithner Laser Technik*, *LED395-66-60*, with a wavelength of 395 nm.

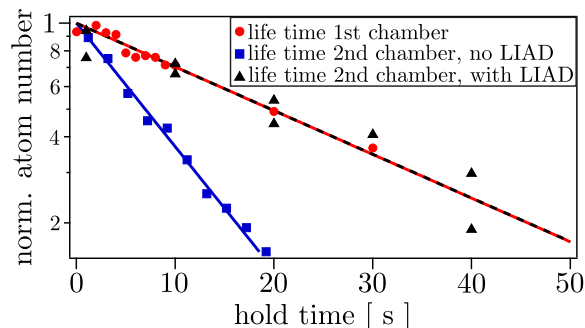


Figure 42: **Lifetime of the atoms in the tweezer.** The normalised number of atoms in the tweezer is shown as a function of the hold time. We observe an increase of the lifetime in the second chamber after the application of LIAD (see text) from about 10 seconds to about 30 seconds. For comparison the same measurement was carried out in the first chamber, which gave an equally slow decay. Also included in the plot are the exponential fits (straight lines), which overlap for the dataset in the first chamber and the dataset in the second chamber after LIAD.

atoms that are only weakly bound to the glass the thermal energy is enough to slowly let them break free and contaminate the vacuum. By illuminating the glass cell with the blue light at least these weakly bound atoms are cleaned off the surface, thereby eliminating this source of pollution.

Figure 42 shows three measurements of the lifetime: The number of atoms in the tweezer in the second chamber was recorded as a function of the hold time t and fitted with an exponential $A \exp(-t/\tau)$. Whereas before the illumination with blue light the lifetime τ was 10 seconds it increased to 28 seconds after LIAD. For comparison a dataset taken in the first chamber is also included, which also gives 28 seconds.

A similar experiment was carried out while holding the atoms in the magnetic trap in the first chamber, which also resulted in a lifetime of ≈ 30 seconds. This implies that the limiting factor is indeed the background pressure of the vacuum, and not a loss mechanism related to the tweezer like intensity or pointing fluctuations.

6 3D Anderson localization

In a classical picture a particle performs a random walk in a medium with a random assortment of scatterers, leading to diffusive propagation. It was already discussed in section 2 that this description is insufficient, and that the quantum mechanical wave nature of particles can in fact lead to the complete halt of propagation. This was first postulated in 1958 by P. W. Anderson [11] under the title “Absence of Diffusion in certain random lattices”, describing the halt of the motion of a spin in a disordered lattice. Originating in the field of condensed matter physics Anderson localization was also observed experimentally with classical waves such as light [120, 110, 102, 67], microwaves [27], and acoustic waves [53]. Open questions like the position of the mobility edge in 3D, the critical behaviour around the mobility edge, and the interplay of interactions between an ensemble of particles and the disorder still remain though due to the complexity of the theory. Ultracold atoms offer the prospect of investigating some of them.

Our experiment was built for the express purpose to observe and study Anderson localization in 3D, and after the completion of the setup the first step was to show that it is indeed capable to localize atoms. It builds on the observation of Anderson localization with ultracold atoms in a 1D configuration, which was carried out in 2008 in our group [20].⁴⁵ In this section the results of this experiment, which were published in [56], are discussed. This work was executed at the beginning of this thesis, and is already described in detail in the PhD thesis of Fred Jendrzejewski [55]. Only a short description of our findings will therefore be given here. We worked in close collaboration with Marie Piraud and Luca Pezzé of the theory group of Laurent Sanchez-Palencia at our institute. Details to the theoretical work can be found in [91] and in the PhD thesis of Marie Piraud [90]. Our results came in parallel with works in the group of Brian DeMarco [62].⁴⁶ Recently there was another observation at the LENS laboratory, which took inspiration of our setup, but used a different atomic species (^{39}K) enabling a control over the inter-atomic interactions via a Feshbach resonance [103]. Previously Anderson localization had also been studied with ultracold atoms in a kicked rotor configuration [82, 28, 71, 75].

6.1 Experimental sequence

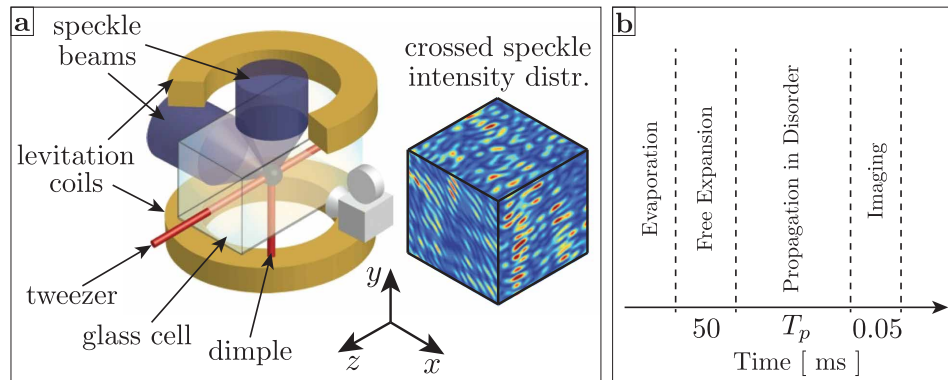


Figure 43: **Overview of the experimental setup and sequence for 3D Anderson localization.**

6.1 Experimental sequence

The experimental sequence starts with the production of a BEC as explained in section 3, and its final steps are sketched in panel **b** of figure 43.⁴⁷ A schematic drawing of the experimental setup is shown in panel **a**. During the whole duration of the experiment there are no outside forces acting on the atoms, as gravity is cancelled by the magnetic levitation (see section 3.3.4). The BEC is released from the trap and first expands freely for 50 ms during which time the interaction energy between the atoms is converted into kinetic energy. The cloud can then be seen as an ensemble of independent, non-interacting atoms with a RMS size of about $30 \mu\text{m}$. At this stage the speckle is switched on rapidly (within 0.1 ms), and the atoms start propagating in the disorder, with the disorder amplitude V_R left constant. A nearly isotropic disorder configuration was used for these experiments, which is obtained by the coherent superposition of two speckle fields (see section 4.2). After a propagation time in the disorder T_p the speckle is switched off rapidly, followed immediately by the imaging of the atomic cloud. An image therefore records the atomic density distribution $n(\vec{r}, T_p)$, integrated once along the optical axis of the imaging system, as a function

⁴⁵A simultaneous experiment was performed in the group of Massimo Inguscio at the LENS laboratory in Florence, Italy [97].

⁴⁶See [83] for a recent discussion of their findings.

⁴⁷At the time this experiment was conducted we had not yet implemented the delta-kick cooling technique. The energy spread of the BEC cloud is therefore determined by its chemical potential of 40 Hz.

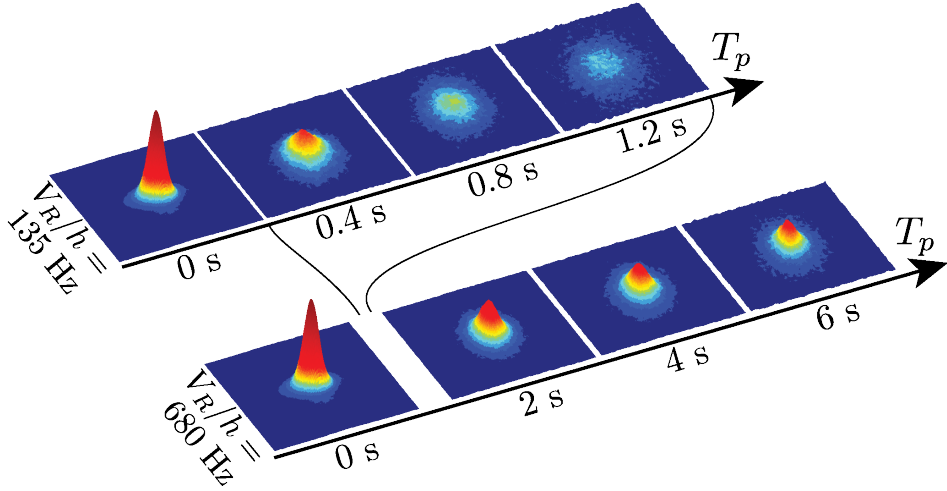


Figure 44: **Evolution of the atom cloud for two weak and strong disorder.** The evolution of the atomic cloud, starting from the same initial conditions, is shown for two different disorder strengths: For weak disorder ($V_R/h = 135 \text{ Hz}$) observation is only possible for a little longer than one second, after which the cloud has expanded so much as to make the density no longer detectable. For strong disorder on the other hand ($V_R/h = 680 \text{ Hz}$) observation is possible up to six seconds.

of the propagation time T_p and the disorder amplitude V_R .

Figure 44 shows the thus recorded evolution of the density distribution for two different strengths of the disorder. Due to the levitation we are able to observe the cloud for up to several seconds.

6.2 Expected behaviour of the system

The atomic cloud at the instant before the speckle is switched on has a certain energy distribution that stems from the interaction energy between the atoms μ_{in} . The kinetic energy associated with the maximum velocity in this distribution is approximately $E_k^{\max} = mv_{\max}^2/2 \approx 2\mu_{in}$, with $\mu_{in}/h \approx 40 \text{ Hz}$ for this experiment. Compared with the typical disorder amplitudes on the

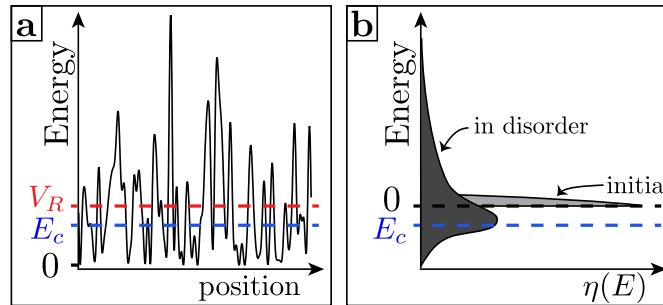


Figure 45: **Energy diagrams.** Panel **a** shows a speckle potential indicating the rough position of the disorder amplitude V_R and the mobility edge E_c . Indicated in panel **b** are sketches of the energy distribution of the atom cloud before and after the rapid switch on of the speckle. The perturbed energy distribution extends to both sides around the mobility edge, such that only a fraction of the atoms is localized. Note that in panel **b** the energy distribution is shifted by V_R such that the average disorder amplitude $\langle V \rangle$ is equal to zero.

order of $V_R/h = 100$ Hz and correlation energy $E_R/h = 6.5$ kHz this initial energy distribution is very narrow. The rapid switch on of the disordered potential modifies this distribution: Qualitatively it can be thought to be shifted by the average amplitude of the disorder V_R and broadened to a width on the order of V_R^2/E_R in the case of quantum disorder. For a strong disorder $V_R^2/E_R \gg \mu_{in}$ the energy distribution of the atoms in the disorder is completely determined by this perturbation. Figure 45 shows qualitatively the position of the disorder amplitude and the broadening of the energy distribution.

According to the scaling theory of localization [1] in 3D systems there exists a threshold energy separating diffusive from localized states. This threshold, the mobility edge E_c , is also predicted to be located in the vicinity of V_R [38] (see figure 45).⁴⁸ Due to the modification of the energy distribution by the rapid switch on of the speckle potential a part of the atoms will fall into the localized regime, whereas the rest will diffuse [107, 123]. Two competing factors, the increase of the mobility edge for increasing disorder

⁴⁸The reference given is a very recent (2014) result coming from numerical simulations. It agrees qualitatively with results from the so-called method of “self-consistent theory of localization”, which was employed by M. Piraud to theoretically confirm our experimental findings [90, 91].

amplitude and the more and more violent perturbation of the energy distribution for increasing disorder amplitude result in a maximum fraction of atoms that fall into the localized regime. It has previously been qualitatively estimated using the self-consistent theory of localization to be about 60% for an isotropic speckle potential [123].

The density of the atom cloud in the disorder $n(\vec{r}, T_p)$ can therefore be separated into two parts, the localized part $n_l(\vec{r})$ and the diffusive part $n_d(\vec{r}, T_p)$. For energies far below the mobility edge the localization length is predicted to be on the order of $1 \mu\text{m}$ [64, 91], which we cannot resolve with our imaging system.⁴⁹ For atoms with energies close to the mobility edge the localization length diverges, but theoretical analysis shows that the number of atoms with localization lengths much larger than $1 \mu\text{m}$ is negligible in our experimental conditions [91, 90]. Within our experimental accuracy the localized fraction of the atoms therefore should be a replica of the atom density distribution at the moment the disorder is switched on:

$$n_l(\vec{r}) = f_l \cdot n(\vec{r}, T_p = 0) \quad (53)$$

Here, $n(\vec{r}, T_p = 0)$ is the density distribution of the cloud at the moment the speckle is switched on, and f_l is the fraction of localized atoms.

Atoms with an energy above the mobility edge are diffusive, their diffusion constant being dependent on their energy $D = D(E)$. Using the Ioffe-Regel criterion $kl^* \approx 1$ (see section 2.6) in conjunction with the definition of the diffusion constant $D = vl^*/3 = \hbar/(3m)kl^*$ (see section 2.4) it is possible to estimate an order of magnitude of the diffusion constant for energies close to the mobility edge:

$$D \approx \frac{\hbar}{3m} \approx 250 \mu\text{m}^2/\text{s} \quad (54)$$

In order for atoms propagating with this diffusion constant to cover distances greater than the initial size of the cloud ($\approx 30 \mu\text{m}$) it is therefore necessary to allow for propagation times on the order of seconds, which is a formidable experimental challenge and only possible due to our magnetic levitation. As described in section 2.6 the diffusion constants close to the mobility edge tend towards zero.

6.3 Experimental observations

The evolution of the density distribution was measured for different disorder strengths V_R while leaving all other parameters equal. Figure 44 shows

⁴⁹The final resolution obtained in our data is estimated to be about $15 \mu\text{m}$.

6.3 Experimental observations

two examples, an evolution in weak ($V_R/h = 135$ Hz) and one in strong disorder ($V_R/h = 680$ Hz). Qualitatively two differences are apparent: First, the observation in weak disorder is limited by the vanishing density as the cloud becomes larger, whereas in strong disorder a longer observation time is possible. Second, in strong disorder a pronounced peak remains, but in weak disorder the cloud continuously spreads out over larger and larger volumes.

In order to quantify these observations we measured the diffusion constant by monitoring the RMS width of the cloud Δu for increasing propagation times. The increase of the size is then given by $\Delta u^2(T_p) = 2\langle D \rangle T_p$. Due to the large broadening of the energies the measured diffusion constants are necessarily an average,

$$\langle D \rangle = \int_{E_c}^{\infty} dE D(E) \eta(E), \quad (55)$$

where $\eta(E)$ is the distribution of energy in the disorder. This method and the results are shown in figure 46. We observe that for a disorder amplitude $V_R/h \geq 500$ Hz the diffusion constant is of the order of the diffusion constant close to the mobility edge as given in equation (54), and $kl^* \approx 4$. This constitutes a strong hint that here the atoms are at least close to the localized regime.

To extract the information whether a fraction of the atoms are localized we employ a phenomenological model for the evolution of the recorded central column density at the center of the cloud $\tilde{n}(0, T_p)$.⁵⁰ This model is based on the decomposition of the density into a localized, and a diffusive part:

$$\tilde{n}(\vec{r}, T_p) = \tilde{n}_l(\vec{r}, T_p) + \tilde{n}_d(\vec{r}, T_p) \quad (56)$$

Panel **a** of figure 47 shows that this central density asymptotically tends towards a finite value. After normalising with respect to the initial central column density $\tilde{n}(0, 0)$ we fit this behaviour with a function

$$\tilde{n}(0, T_p)/\tilde{n}(0, 0) = f_{\text{loc}} + \frac{C}{T_p}, \quad (57)$$

with some constant C . A decrease inversely proportional to the propagation time is expected from diffusive behaviour where the density in 3D falls as \sim

⁵⁰The full three-dimensional density was previously denoted by $n(\vec{r}, t)$. Taking an image automatically integrates this density over the x -axis, and we show this by adding a tilde, $\tilde{n}((y, z), t) = \int dx n(\vec{r}, t)$. The central column density of the distribution therefore is $\tilde{n}(0, t)$.

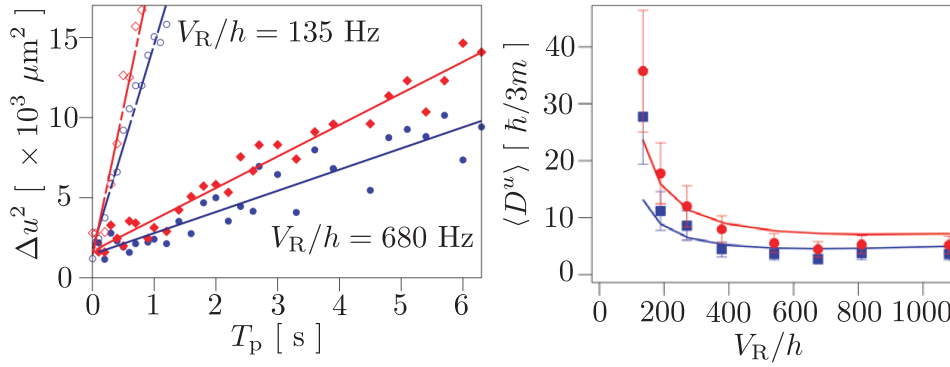


Figure 46: **Diffusion constants.** To measure the average diffusion constants $\langle D \rangle$ we monitor the mean square width of the cloud Δu^2 as a function of the propagation time, as shown on the left hand graph. The blue points are the size along z , and the red diamonds along y . The straight lines are linear fits. These diffusion constant are shown on the right hand graph as a function of the disorder amplitude V_R . They are normalised with respect to the typical diffusion constant close to the mobility edge $\hbar/3m$ from equation (54). The remaining anisotropy of the speckle potential leads to a slight anisotropy of the diffusion. The lines stem from theoretical calculations (see text).

6.3 Experimental observations

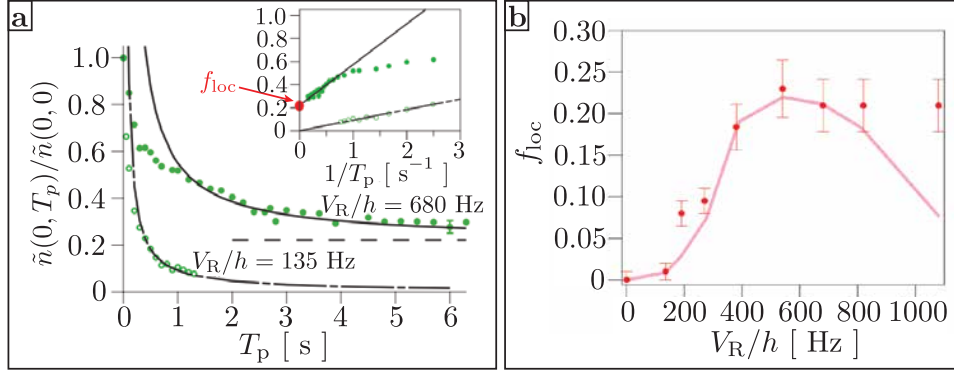


Figure 47: **Extraction of the localized fraction.** Panel **a** shows the evolution of the normalised central density as a function of the propagation time T_p for two disorder amplitudes $V_R/h = 135$ Hz and $V_R/h = 680$ Hz. The inset shows the same data, only this time as a function of the inverse propagation time, $1/T_p$. Using a fit it is possible to extract the localized fraction f_{loc} (see equation (57)). Panel **b** shows the localized fraction of the atoms as a function of the disorder strength. The results of the theoretical calculations are plotted as a straight line (see [56, 91]).

$T_p^{-3/2}$. The $1/T_p$ behaviour then follows from integrating over one spatial direction.

The fit-parameter f_{loc} is interpreted as the localized fraction of the atoms, and their value as a function of the disorder strength is shown in panel **b** of figure 47. The central result of this experiment is the thus extracted localized fraction as shown in panel **b**. We observe a steady increase until f_{loc} saturates at around 20-25%. We attribute this saturation to the fact that the increasing disorder strength also increases the broadening of the atoms' energy distribution: For increasing V_R one expects an increase of the localized fraction, as observed for $V_R/h \leq 400$ Hz. But above $V_R/h \approx 500$ Hz the induced broadening of the energy distribution seems to counter-balance this effect. There is a discrepancy between theory and experimental results for high disorder strengths, which prompts for a more elaborate theoretical description.

6.4 Conclusions

The work presented here constitutes a first observation of 3D Anderson localization of ultracold atoms. We monitored the expansion of an atomic cloud in a quasi-isotropic optical speckle disorder, and observed a diffusive as well as a localized fraction. These two fractions respectively correspond to atoms above, and below the mobility edge. The full experimental observations, the diffusive behaviour, the localized fraction, and the overall evolution of the density distribution are in good agreement with a self-consistent theoretical approach adopted to our experimental parameters.

In the setup presented here the energy of the atoms in the disorder cannot be very well controlled, since for strong disorder it is entirely determined by the disorder induced spread. An ongoing work is the development of a technique to precisely control the energy of the atoms, which would open up the possibility to study the critical behaviour around the mobility edge.

6.4 Conclusions

7 Coherent Backscattering

The transport of classical particles in a disordered medium can be modelled by a random walk. This random walk is the microscopic picture underlying the macroscopic diffusive transport. As laid out in chapter 2, coherent wave propagation in disordered media differs from this classical description by interference corrections. These corrections can ultimately lead to the complete halt of propagation, resulting in the so called Anderson Localisation (see sections 2.6 and 6). Preceding the localisation of waves are first order corrections of the propagation, namely Weak Localisation (WL) and Coherent Backscattering (CBS). WL and CBS are related as they both rely on the interference between multiply scattered counter-propagating paths. WL results in an increased probability to return to the same spatial point during a random walk, whereas CBS leads to an increased directly backscattered intensity. Both effects have been investigated thoroughly for several decades, with notable examples for CBS being the first theoretical descriptions [117, 112, 4] which were going hand in hand with the first laboratory controlled experimental observations [63, 113, 122]. These first explorations were carried out using electromagnetic waves, but just like Anderson localization, Coherent Backscattering is a very general effect for waves in disordered media. It has also been observed for acoustic waves [16, 111], and seismic waves [68]. Figure 48 portrays an example of the coherent backscattering enhancement as recorded previously by another experiment using electromagnetic waves [121].

In this section the first observation of Coherent Backscattering of ultracold atoms is presented. We took inspiration from a theoretical proposal by N. Cherroret *et al.* in [29]. It suggested to launch atoms with a well defined momentum into a disordered potential in a 2D configuration, and to monitor the ensuing evolution of the atoms' momentum space distribution. Figure 49 shows numerical simulations of the momentum distribution for two propagation times in the disorder, reproduced from [29]. In it the coherent contribution to the propagation, the CBS peak, is clearly visible on top of the incoherent contribution, which forms a ring structure. This clear signal provides a telltale sign of phase coherent transport of cold atoms in disordered media. Also it was noted that the momentum space evolution would make it possible to directly measure two fundamental transport parameters, the mean scattering time and the transport time.

Our experimental results were published in [57], and are also described in the PhD thesis of F. Jendrzejewski [55]. It provides the context for our experiments on the Coherent Backscattering Revival, which will be treated

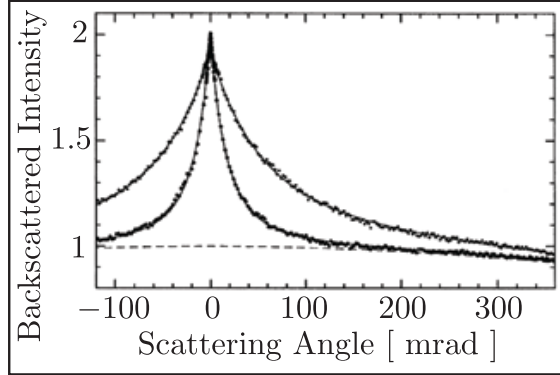


Figure 48: **Example of the Coherent Backscattering enhancement.** Shown here is the CBS peak of light incident on fine powders, reproduced from [121] (the two data sets correspond to two different samples with different mean free paths). It showcases the enhancement by a factor 2 relative to the incoherent background (dashed line).

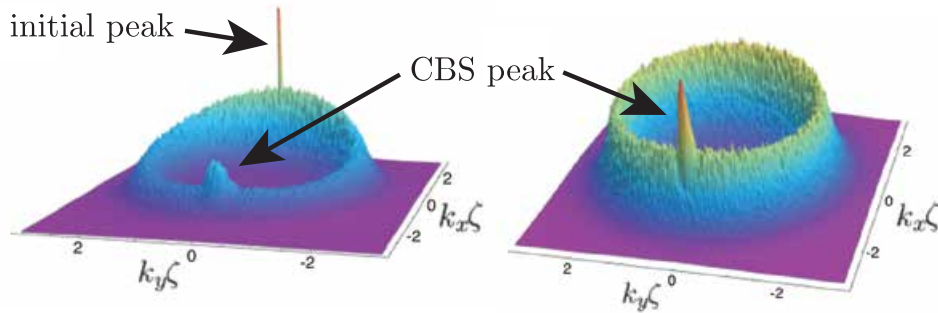


Figure 49: **Evolution of the momentum-space distribution in 2D.** From an initially well defined momentum state the atoms are elastically scattered by the disordered potential and populate momenta on a ring centered around zero. The left hand picture shows the beginning of the formation of this ring, while a small number of atoms still remain unscattered in the initial momentum state (initial peak). The CBS peak starts to form in backscattering direction and remains the only feature for longer propagation times in the disorder (right image). This figure is reproduced from [29].

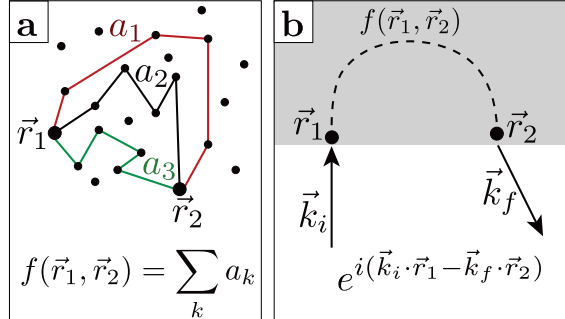


Figure 50: Panel **a** shows different paths between two fixed points, \vec{r}_1 and \vec{r}_2 . Each path is associated with a complex amplitude a_k , and the total amplitude $f(\vec{r}_1, \vec{r}_2)$ corresponding to the propagation from \vec{r}_1 to \vec{r}_2 is the sum of the amplitudes of all individual paths. The phase accumulated during the propagation outside the disorder depends on the wavevectors of the incoming and outgoing wave \vec{k}_i and \vec{k}_f as shown in panel **b**. Without loss of generality it can be written as $\exp[i(\vec{k}_i \cdot \vec{r}_1 - \vec{k}_f \cdot \vec{r}_2)]$.

in section 8.

7.1 The Coherent Backscattering mechanism

In order to investigate the mechanism underlying Coherent Backscattering we will follow the approach given in [3], which is based on looking at individual paths along which the wave can propagate in the disorder. The disorder itself is modelled as an ensemble of point scatterers with random positions, and all scattering events are supposed to be completely elastic.

In order to understand the mechanism leading to coherent backscattering we are investigating the complex amplitude that is associated with a plane wave with wavevector \vec{k}_i that scatters in the disordered medium into a final state \vec{k}_f . First, the wave can take different paths within the disorder. Shown in figure 50 **a** are different paths connecting an initial scattering point \vec{r}_1 with a final point \vec{r}_2 . Each path is associated with a complex amplitude $a_k = |a_k|e^{i\delta_k}$, and the total amplitude $f(\vec{r}_1, \vec{r}_2)$ describing the propagation between these points is the sum over all paths, $f(\vec{r}_1, \vec{r}_2) = \sum_k a_k$. We also have to take into account the phase accumulated due to the propagation outside the disorder. Without loss of generality for the further calculations this phase can be written as $\exp[i(\vec{k}_i \cdot \vec{r}_1 - \vec{k}_f \cdot \vec{r}_2)]$, resulting in a total

7.1 The Coherent Backscattering mechanism

amplitude

$$A(\vec{k}_i, \vec{k}_f, \vec{r}_1, \vec{r}_2) = f(\vec{r}_1, \vec{r}_2) e^{i(\vec{k}_i \cdot \vec{r}_1 - \vec{k}_f \cdot \vec{r}_2)} \quad (58)$$

Since the waves are extended many starting and end points are possible, and we sum to arrive at the total amplitude that connects the given initial wave with a given outgoing wave:

$$\begin{aligned} A(\vec{k}_i, \vec{k}_f) &= \sum_{\vec{r}_1, \vec{r}_2} A(\vec{k}_i, \vec{k}_f, \vec{r}_1, \vec{r}_2) \\ &= \sum_{\vec{r}_1, \vec{r}_2} f(\vec{r}_1, \vec{r}_2) e^{i(\vec{k}_i \cdot \vec{r}_1 - \vec{k}_f \cdot \vec{r}_2)} \end{aligned} \quad (59)$$

The intensity of the backscattered wave is proportional to the square of the absolute value of this amplitude:

$$\begin{aligned} I(\vec{k}_i, \vec{k}_f) &= A(\vec{k}_i, \vec{k}_f) A^*(\vec{k}_i, \vec{k}_f) \\ &= \sum_{\vec{r}_1, \vec{r}_2} \sum_{\vec{r}_3, \vec{r}_4} \sum_k \sum_l |a_k| |a_l| e^{i(\delta_k - \delta_l)} e^{i[\vec{k}_i \cdot (\vec{r}_1 - \vec{r}_3) - \vec{k}_f \cdot (\vec{r}_2 - \vec{r}_4)]} \end{aligned} \quad (60)$$

So far the intensity is the result of a sum of many complex amplitudes with random phases. This was already treated in section 4 and leads to a speckle, where the intensity is a random function with exponential distribution. The speckle depends on the distribution of the scatterers so that each disorder configuration leads to a different speckle. One expects that averaging the intensity over many different disorder configurations leads to a featureless function of the intensity, but surprisingly this is not the case: The phase of the term $|a_k| |a_l| \exp[i(\delta_k - \delta_l)]$ in equation (60) is equal to 1 for any disorder configuration if the paths k and l are either the same, or if they are time-reversed counterparts. These two possibilities are shown in figure 51. In the first case the end points of the paths are equal and one has $\vec{r}_1 = \vec{r}_3$ and $\vec{r}_2 = \vec{r}_4$, whereas in the second case one has $\vec{r}_1 = \vec{r}_4$ and $\vec{r}_2 = \vec{r}_3$. Since, at least to first order, all except these two classes of paths vanish when averaging over different disorder configurations we are able to rewrite equation (60) in the simpler form (the averaging is denoted by $\langle \dots \rangle$):

$$\begin{aligned} \langle I(\vec{k}_i, \vec{k}_f) \rangle &= \left\langle \sum_{\vec{r}_1, \vec{r}_2} \sum_k |a_k|^2 \left(1 + e^{i(\vec{k}_i + \vec{k}_f) \cdot (\vec{r}_1 - \vec{r}_2)} \right) \right\rangle \\ &= \left\langle \sum_{\vec{r}_1, \vec{r}_2} |f(\vec{r}_1, \vec{r}_2)|^2 \left(1 + e^{i(\vec{k}_i + \vec{k}_f) \cdot (\vec{r}_1 - \vec{r}_2)} \right) \right\rangle \end{aligned} \quad (61)$$

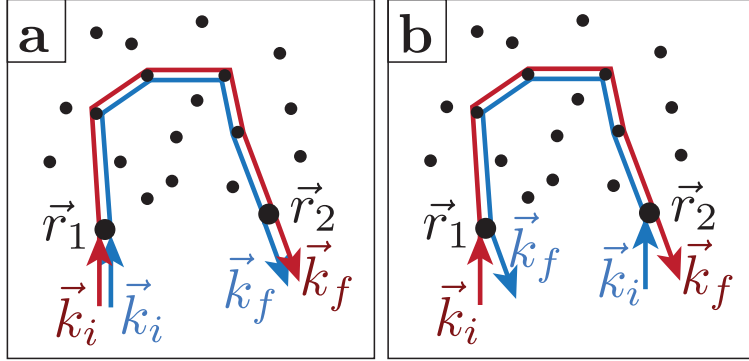


Figure 51: When averaging over many disorder configurations two classes of paths contribute to the average intensity: Both follow the same sequence of scatterers, either in the same (panel **a**) or in counter-propagating directions (panel **b**). The second class of paths are responsible for the Coherent Backscattering signal.

The constant term corresponds to the pair of paths that traverse the disorder in the same direction, and we will refer to it as the “classical” term. The second term depends on the incoming and the outgoing wavevectors, and is equal to 1 when $\vec{k}_i = -\vec{k}_f$, that is in direct backscattering direction. We have therefore identified the mechanism leading to coherent backscattering as the constructive interference between counter-propagating paths. It ideally leads to an increase in the intensity by a factor 2 compared to only the classical term.

It should be noted here that the same line of arguments leads to the description of weak localisation (see section 2.5): In equation (61) an increase of the intensity (probability) can also be achieved by setting $\vec{r}_1 = \vec{r}_2$. In this case the paths form closed loops, with the paths either circulating in the same or in opposite directions. Weak localisation is then an increase in the return probability due to the interference of counter-propagating loops.

7.2 Experimental sequence

In order to realise an experiment to observe the coherent backscattering peak with ultracold atoms in 2D we follow a theoretical proposal by Cherroret *et al.* [29], which suggested the study of CBS in momentum space: A cloud of atoms is prepared with a well defined initial mean momentum $\hbar\vec{k}_i$ and a

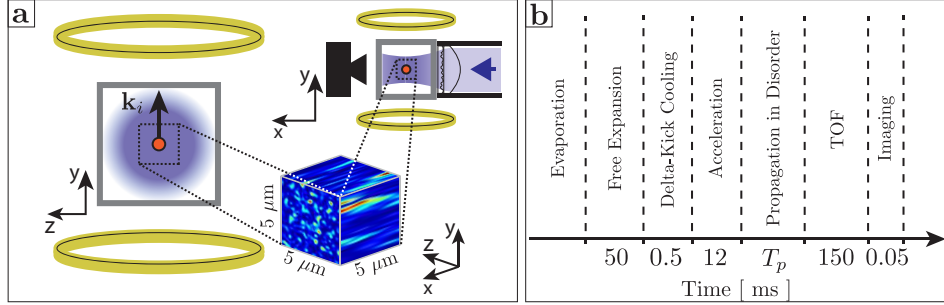


Figure 52: **Experimental setup and sequence.** Panel **a** shows the experimental setup, with the levitation coils (yellow), the glass cell (gray square), the speckle field (shaded blue), and the atomic cloud (orange point). A 2D representation is chosen, since all relevant dynamics happen in the $y - z$ plane (see text). The anisotropic speckle intensity distribution is indicated. On the upper right hand of the panel a side-view of the setup ($x - y$ plane) is shown, including the speckle arm and the camera. Panel **b** shows the different steps of the experimental sequence.

small momentum spread. This assures that we are close to the theoretical description in the previous section, where we assumed an incoming plane wave. Also, any interactions between the atoms should be eliminated, since we assumed that the evolution of the wave function is linear.

The experimental setup and the sequence are shown in figure 52. The initial preparation of a Bose-Einstein condensate and the reduction of the velocity spread of the cloud using the delta-kick cooling technique follows the steps laid out in section 3. Gravity can be neglected throughout the experiment due to the magnetic levitation (see section 3.3.4). We then accelerate the atoms with an additional magnetic gradient field along y for 12 ms to a velocity of 3.3 ± 0.2 mm/s ($|\vec{k}_i| \approx 4.5 \mu\text{m}^{-1}$).

Thus prepared we expose the atoms to the disorder by abruptly (within 0.1 ms) switching on the optical speckle described in section 4. We choose the anisotropic speckle configuration generated by only one laser beam. The initial velocity is perpendicular to the optical axis of the speckle, leading to a quasi 2-dimensional dynamics (see section 7.3.1). The atoms are allowed to propagate in the disorder for a controlled time T_p before the speckle is switched off. After having switched off the speckle we let the atoms fly freely for 150 ms before taking a picture. During this time of flight the velocity distribution is converted into a position distribution, so that the image that

Quantity	Value
Initial Velocity	$v_i = 3.3 \pm 0.2$ mm/s
Corresponding Wavevector	$k_i = 4.5$ μm^{-1}
Disorder Amplitude	$V_R/h = 975 \pm 80$ Hz
Speckle Autocorr. Function Transverse Size	$\sigma_{\perp} = 0.2$ μm (RMS)
Speckle Autocorr. Function Longitudinal Size	$\sigma_{\parallel} \approx 1$ μm (HWHM)
Mean Scattering Time (Transverse)	$\tau_S = 0.33 \pm 0.02$ ms
Transport Time (Transverse)	$\tau^* = 0.4 \pm 0.05$ ms

Table 1: **Key parameters for the CBS experiments.**

we take of the density distribution in real space corresponds directly to the density distribution in momentum space. The key parameters for this experiment are combined in table 1.

7.3 Expected dynamics

In this section the expected dynamics of the system are laid out. We first argue that, even though we do not have a 2D confinement for the atoms, we can treat the dynamics as being 2-dimensional. The resolution in momentum space that we can achieve is briefly introduced before the expected dynamics of the CBS peak is laid out.

It will be discussed in section 7.4.1 that we are able to determine the key transport parameters τ_S and τ^* , the mean scattering time and the transport time. Together with the initial velocity, the disorder amplitude, and the autocorrelation function of the speckle we have a complete characterisation of the system.

7.3.1 Quasi 2D dynamics

The atoms are exposed to an anisotropic speckle field, whose features are large in the longitudinal direction x and comparatively short in the transverse plane $y - z$ (see figure 52). As discussed in section 4 this speckle is created by a single laser beam passing through a diffusive plate and focussed onto the atoms by a lens. The optical axis of the speckle is x . The initial velocity of the atoms is perpendicular to the optical axis of the speckle, and the redistribution of the momenta is strongly influenced by the anisotropy of the disorder (see figure 53):

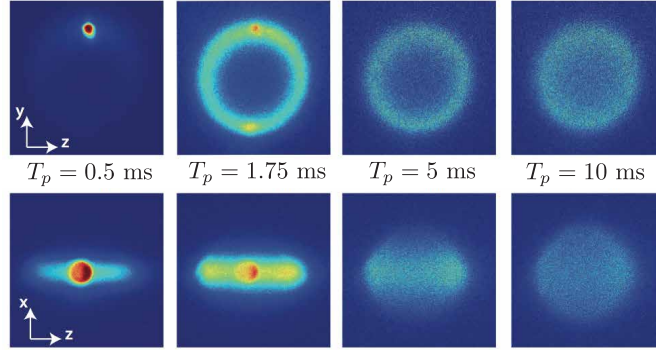


Figure 53: **Momentum isotropisation in the anisotropic speckle.** The anisotropy of the disordered speckle potential has an effect on the redistribution of the momenta. The atoms, with an initial velocity along y , are redistributed in the $y - z$ plane on the time scale of a single scattering event, since the typical size of a speckle grain in this plane is small (on the order of the deBroglie wavelength). This is shown in the top row. Along x on the other hand the size of the speckle grains is larger and it takes several scattering events to completely redistribute the momenta. The images in the bottom row indicate that the redistribution along x becomes important only for propagation times larger than ≈ 5 ms (about $15 \tau_S$ or $13 \tau^*$). The bottom row images are blurred since most of the atoms are situated outside the focal plane of this imaging system. The experimental parameters for these images are the same as the ones used for our experiments on CBS (see table 1).

In the transverse plane $y - z$ the typical size of the speckle grains is $\sigma_{\perp} \approx 0.2 \mu\text{m}$ and therefore smaller than the deBroglie wavelength of the atoms: $\sigma_{\perp} k_i \approx 0.9 < 1$. This implies a nearly isotropic scattering in the transverse plane, that is, a single scattering event is enough to completely redistribute the momenta in this plane.

Longitudinally the typical size of a speckle grain is larger, and we have $k_i \sigma_{\parallel} \approx 4.5 > 1$. Therefore the scattering is directed mainly in the forward direction, and it takes several scattering events to completely redistribute the momenta along x .

The anisotropy of the disorder therefore leads to quasi 2-dimensional dynamics for short propagation times up to ≈ 5 ms: Even though we do not have a 2D confinement for the atoms, as long as the redistribution along x is negligible we are able to treat the dynamics as 2D.

7.3.2 Momentum space resolution

The resolution that we obtain in our velocity (momentum) space measurements is determined by several factors: The long but still finite time of flight TOF , the initial size of the cloud Δr , and the initial velocity spread of the cloud Δv_i . They are combined to give the velocity resolution

$$\Delta v_{res} = \sqrt{\Delta v_i^2 + \frac{\Delta r^2}{TOF^2}}. \quad (62)$$

In our experiments the time of flight is $TOF = 150$ ms, the initial size of the cloud is $\Delta r \approx 30 \mu\text{m}$ (gaussian fit RMS), and the initial velocity spread is $\Delta v_i = 0.12$ mm/s, leading to a resolution of $\Delta v_{res} = 0.23$ mm/s that is mainly limited by the initial size of the cloud.

7.3.3 Dynamics of the CBS peak

In our experiments we are observing the evolution of the momentum space distribution. The shortest time-scale of our system, the mean scattering time $\tau_S = 0.33$ ms is long enough to be resolved easily, allowing us to monitor the CBS peak after a precisely determined propagation time in the disorder. Similar experiments, where the time-evolution of the CBS peak was recorded using femtosecond laser pulses and acoustic waves [116, 111].

Two quantities are of interest here: the contrast of the CBS peak, that is its amplitude with respect to the amplitude of the incoherent momentum space contribution, and its width. We are giving here again equation (61), since the discussion of the dynamics of the CBS peak will be based on it.

7.3 Expected dynamics

Instead of the disorder averaged intensity $\langle I(\vec{k}_i, \vec{k}_f) \rangle$ depending on the initial and final wave vectors \vec{k}_i and \vec{k}_f we will write here the disorder averaged momentum space density $\langle n(\vec{k}_f) \rangle$ depending only on the final momentum state since the initial momentum is fixed by the preparation of the atomic cloud:

$$\begin{aligned} \langle n(\vec{k}_f) \rangle &\propto \langle I(\vec{k}_i, \vec{k}_f) \rangle \\ &\propto \sum_{\vec{r}_1, \vec{r}_2} |f(\vec{r}_1, \vec{r}_2)|^2 \left(1 + e^{i(\vec{k}_i + \vec{k}_f) \cdot (\vec{r}_1 - \vec{r}_2)} \right) \end{aligned} \quad (63)$$

For the further discussion we will use the convention to call the incoherent momentum space contribution $\langle n_{incoh}(\vec{k}) \rangle$ (described by the first constant term in equation (63)), and the coherent contribution $\langle n_{coh}(\vec{k}) \rangle$ (the second exponential term). The contrast is then defined as $C(\vec{k}) = \langle n_{coh}(\vec{k}) \rangle / \langle n_{incoh}(\vec{k}) \rangle$. According to equation (63) the contrast in direct backscattering direction $C(\vec{k}_f = -\vec{k}_i)$ should always be equal to one. One caveat is that in order to be able to speak about counter-propagating loops there have to be at least two scattering events. For short propagation times $T_p \leq 2\tau_S$ it is therefore not yet appropriate to talk about coherent backscattering since single scattering is predominant.

The width of the CBS peak is determined by the gradual dephasing between the counter-propagating paths when looking in directions that differ from the direct backscattering direction $\vec{k}_f = -\vec{k}_i$. The rate of this dephasing is determined by the average distance between the first and the last scattering point after a propagation time T_p : $\langle d \rangle_{T_p} = \langle |\vec{r}_1 - \vec{r}_2| \rangle$. Writing explicitly the average phase difference between the counter-propagating paths $\Delta\Phi_{CBS}$ we have:

$$\Delta\Phi_{CBS} = \langle d \rangle_{T_p} |\vec{k}_i + \vec{k}_f| \quad (64)$$

It is well known that the average distance travelled for diffusive motion is $\langle d \rangle_{T_p}^{diff} = \sqrt{2DT_p}$, where D is the diffusion constant. But here again we have to take into account that we can probe very short propagation times where the number of scattering events is on the order of one. Taking a path with two scattering points as an example it is clear that the propagation between them is not diffusive but ballistic. This leads to $\langle d \rangle_{T_p}^{ball} \sim v_i T_p$. A theoretical treatment of this initial ballistic propagation in [49] gives $\langle d \rangle_{T_p}^{ball} = v_i T_p / 3$.

Setting the limit of the dephasing in equation (64) to 1 we can therefore

extract the evolution of the width of the CBS peak:

$$|\vec{k}_i + \vec{k}_f| \sim \frac{1}{\langle d \rangle_{T_p}} = \begin{cases} \frac{3}{v_i T_p} & \text{ballistic} \\ \frac{1}{\sqrt{2DT_p}} & \text{diffusive} \end{cases} \quad (65)$$

We therefore expect the width to decrease as $1/T_p$ for small times before there is a transition to diffusive propagation when the width decreases as $1/\sqrt{T_p}$. The time this transition takes place should be on the order of the transport time τ^* . The shape of the CBS peak in momentum space at time T_p is the Fourier transform of the 2D real space density distribution at the same time. For diffusive propagation both are gaussian, an approximation that we find to be also in good agreement in our data treatment for the ballistic regime.

7.4 Experimental results

Figure 54 shows some representative examples of the experimentally obtained momentum-space densities for different propagation times.⁵¹ Initially all atoms are located in a peak around the initial momentum $\vec{p}_i = \hbar\vec{k}_i$. For increasing propagation times they are scattered out of this initial state and start populating other momenta located on a ring with $|\vec{k}| \approx |\vec{k}_i|$. The CBS peak is clearly visible above the incoherent background at $\vec{k} = -\vec{k}_i$ as soon as there is an appreciable amount of atoms in this backscattered region.

As described in the next section we can use the evolution of the initial peak and the redistribution of the momenta to extract the mean scattering time τ_S and the transport time τ^* , which were already introduced in section 2.3. The extraction of the CBS dynamics are detailed in section 7.4.2. For both measurements we extract the angular density profile of the momentum-space distribution as indicated in figure 55.

7.4.1 Determination of the mean scattering and the transport time

The mean scattering time The mean scattering time τ_S reveals itself in the exponential decay of the number of atoms in the initial momentum state k_i [29]:

$$n(k_i, T_p) = n(k_i, 0) e^{-\frac{T_p}{\tau_S}} \quad (66)$$

⁵¹The similarity with those of numerical simulations, shown in figure 49, is striking.

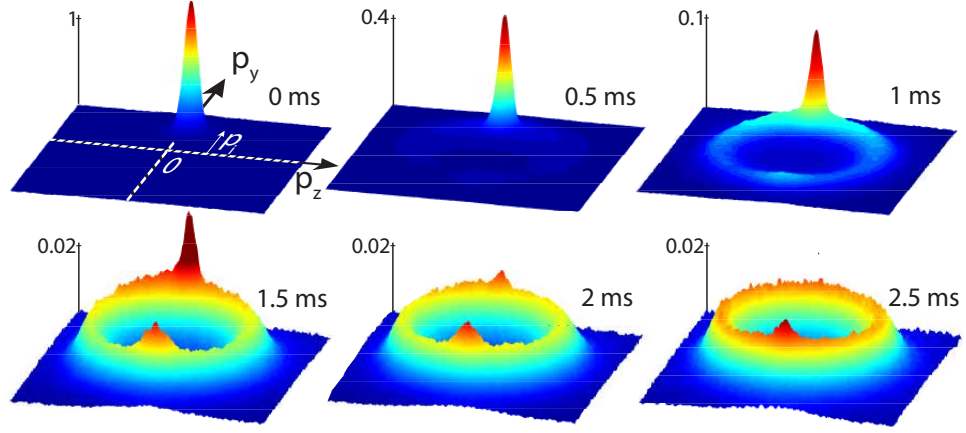


Figure 54: **Momentum space density evolution.** The recorded momentum space density is shown for different propagation times. Initially all atoms are concentrated in a peak at $\vec{p}_i = \hbar\vec{k}_i$. As the propagation time increases the atoms are scattered out of the initial k -mode and start populating all states with $|\vec{k}| = |\vec{k}_i|$. As soon as the ring is established the CBS peak becomes visible at $\vec{k} = -\vec{k}_i$.

We extract this decrease using a heuristic lorentzian fit of the initial peak in the angular profile for different propagation times as shown in figure 56. For the parameters used in this experiment we obtain $\tau_S = 0.33 \pm 0.02$ ms, which implies a mean free path of $l_S = v_i\tau_S = 1.1 \mu\text{m}$. This experimental result is in agreement with numerical simulations, but is about a factor 2 larger than a theoretical result obtained from perturbative calculations [91]. The latter discrepancy can be explained by the fact that we are not fully in the weak disorder regime ($k_i l_S \approx 5$).

The scattering time is linked to the energy distribution of the atoms in the disorder, which reveals itself in the radial width of the ring in momentum space (see figure 55). In the weak disorder limit this spread is a lorentzian with HWHM $\Delta E = \hbar/\tau_S$, which we find to be in qualitative agreement with our data.

The transport time The transport time is, loosely speaking, the time scale after which the incoherent momentum distribution becomes fully isotropic, and the propagation becomes diffusive. In our data treatment it is therefore roughly the time after which the angular profile becomes flat, neglect-

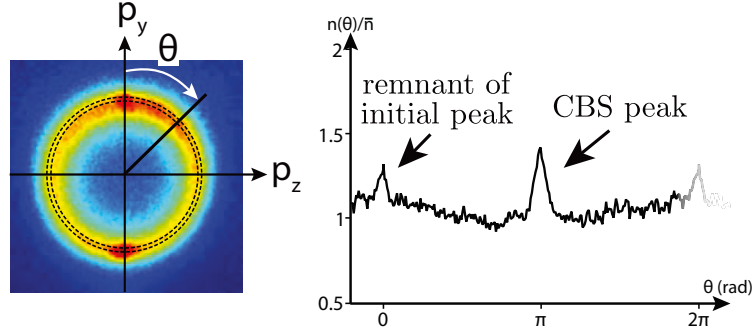


Figure 55: **Extraction of the angular profile of the momentum space distribution.** The picture on the left hand side shows the recorded momentum distribution after a propagation time of 2 ms. A radial integration over a small strip, indicated by the dashed lines, is performed and results in an angular profile, shown on the right side. In this angular representation the decay of the initial peak, the redistribution of the momenta, and the evolution of the CBS peak can be monitored. The thus extracted profiles are normalised such that for long propagation times the flat background distribution has a value equal to 1.

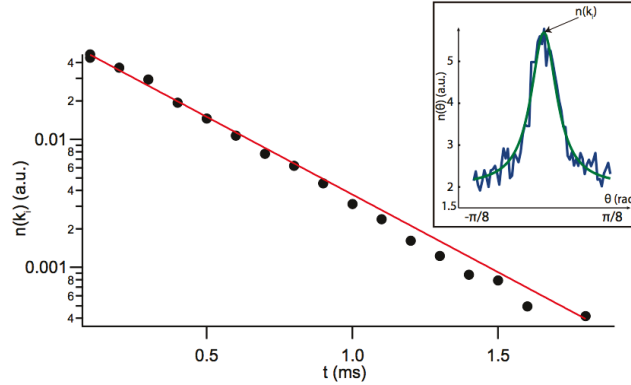


Figure 56: **Extraction of the mean scattering time.** The decrease of the initial peak is shown together with an exponential fit used to extract the mean scattering time (see equation 66). The inset shows an example of the heuristic lorentzian fit function used to extract the amplitude of the initial peak from the angular profile of the momentum space density.

7.4 Experimental results

ing the persisting CBS peak (see figure 57). Its quantitative value can be calculated from the decomposition of the angular profile into its Fourier components [93]:

$$n(\theta, T_p) = \sum_{m=0}^{\infty} n_m(T_p) \cos(m\theta) \quad (67)$$

The first Fourier component $n_1(T_p)$ decays exponentially with its characteristic time being the transport time:

$$n_1(T_p) = n_1(0)e^{-\frac{T_p}{\tau^*}} \quad (68)$$

We find $\tau^* = 0.4 \pm 0.05$ ms, which implies a transport path of $l^* = v_i\tau^* = 1.32 \pm 0.17 \mu\text{m}$. The transport time is only slightly larger than the scattering time since for this experiment the scattering is nearly isotropic ($k_i\sigma_{\perp} = 0.9$). Inspecting the angular profiles we find that the momentum distribution is isotropic for propagation times longer than about $2.5 \text{ ms} \approx 6\tau^*$.

7.4.2 CBS dynamics

Following from equation 63 the CBS peak is a gaussian in the diffusive regime. The incoherent background distribution is expected to be a smooth function [93], and can locally be approximated by a parabola. We are therefore led to the following function, used to extract the contrast and the width of the CBS peak in the region around $\theta = \pi$ of the angular profiles:

$$f(\theta) = A_1 + A_2(\theta - \theta_0)^2 + A_3e^{-(\theta - \theta_0)^2/(2\sigma_{\theta}^2)} \quad (69)$$

The width of the CBS peak here is given by σ_{θ} , and the peak contrast is easily extracted by $C(-\vec{k}_i) = A_3/A_2$. Figure 57 shows the angular profiles of some propagation times including this fit, and figure 58 shows the thus extracted evolution of the contrast and width of the CBS peak.

To compare the evolution of the width with theoretical predictions we must take into account the finite momentum space resolution $\Delta\theta_{\text{res}} = \Delta v_{\text{res}}/v_i = 0.07$ (see section 7.3.2). The black line in panel **b** represents a convolution of this resolution with the CBS width in the diffusive regime $\sigma_{\theta} = \Delta_{k,\text{CBS}}/k_i = 1/(k_i\sqrt{2DT_p})$ (compare with equation 65), where the diffusion constant is evaluated using the standard relation $D = v_i^2\tau^*/2$. This approach works well for propagation times larger than $\approx 4\tau^*$ when the propagation is diffusive, but does not fit the observations for shorter times. A similar calculation using the ballistic approximation of the propagation in formula 65, shown in

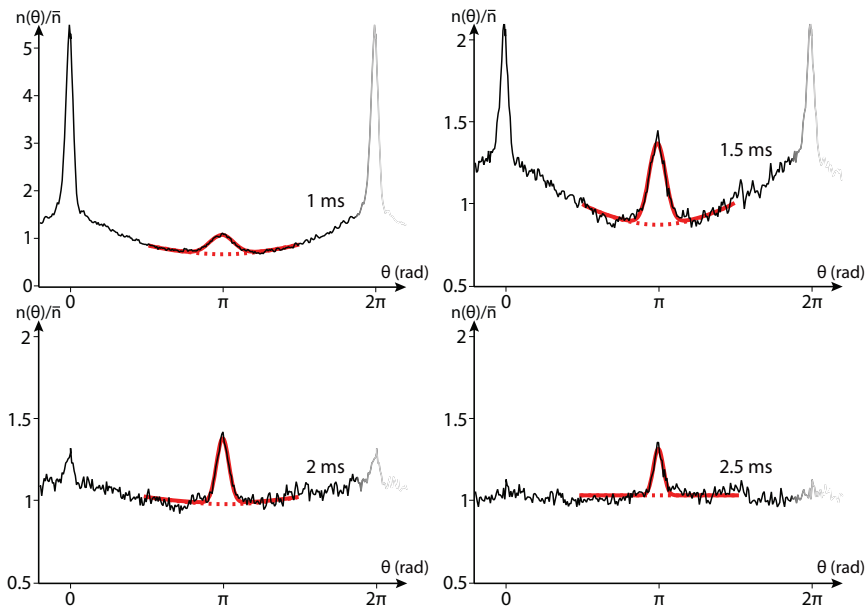


Figure 57: **Extraction of CBS contrast and width.** In the angular profiles the initial peak is located at $\theta = 0$, and the CBS peak is at $\theta = \pi$. The sum of a gaussian and a quadratic function, shown in red, are used to extract the contrast and the width of the CBS peak (see text).

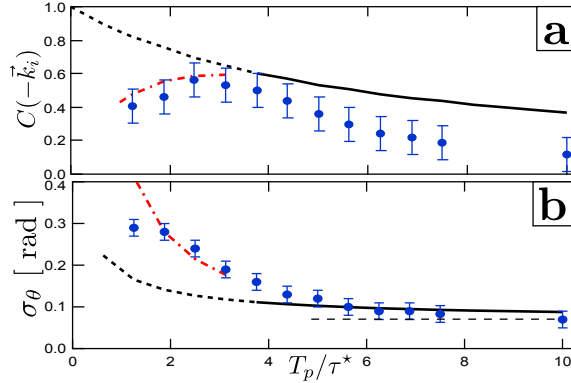


Figure 58: **Contrast and width of the CBS peak.** Panel **a** shows the evolution of the contrast, and panel **b** the evolution of the width of the CBS peak. The propagation time T_p is normalised with respect to the transport time τ^* . The experimental results (blue points) are shown together with the theoretical predictions for purely diffusive (black) and ballistic propagation (red).

red, where width is expected to decrease as $1/T_p$ on the other hand provides a good approximation to our observations.

The contrast, shown in panel **a**, is initially increasing. This can be explained by the fact that for coherent backscattering at least two scattering events are necessary, and for short times the probability of single scattering is not negligible. A theoretical treatment for isotropic scattering of light [49] predicts for times up to several τ_S an evolution of the contrast $C = (2T_p/\pi\tau_S)/(1 + 2T_p/\pi\tau_S)$. This short term evolution is plotted as a dashed red line in figure 58 **a**. We never see a contrast of one, which again is due to the necessary convolution with our finite resolution and was also observed in numerical simulations in [29]. The predicted evolution of the peak contrast is shown as a black line, and we observe a consistently lower contrast for longer propagation times. This is due the onset of the 3D isotropisation of the momenta, which increase the apparent incoherent contribution of the momentum distribution.

7.4.3 Inherent disorder averaging

We saw in section 7.1 in order to make the CBS peak clearly visible it is necessary to average over many different realisations of the disorder. In

principle this could be achieved in our experiment by rotating the diffusive plate that creates the speckle potential, but due to mechanical constraints this is hardly feasible. Fortunately we heuristically found that even without changing the disorder configuration we do not record a noisy speckle-like distribution, but rather one that already seems to be disorder-averaged. There are several tentative explanations for this observation:

- The data presented here are averaged about 20 times for each propagation time. Although the disorder configuration does not change, small variations in the initial conditions of the atomic cloud (for example its position) could make the atoms experience disorder configurations that differ from shot to shot.
- The resolution of the imaging system is larger than the typical size of a speckle grain ($\approx 3 \mu\text{m}$ compared to $\approx 0.2 \mu\text{m}$), which washes out any small fluctuations.
- It could be that the atoms' phase relation in the initial cloud changes between shots, since we perturb it with the delta-kick cooling method. The positions of the light and dark spots in a speckle depend on the configuration of the disorder, but equally they depend on any eventual phase relation of the incident waves so that averaging over several shots with different phase relations would have the same effect as a disorder averaging.
- The initial cloud is extended over several tens of microns in all directions, which is larger than the longitudinal size of the speckle grains (on the order of a micron). Different parts of the cloud therefore experience different disorder configurations. The imaging performs an integration along the longitudinal speckle axis, so that even within one shot one has an average over maybe as many as several tens of disorder configurations.

7.5 Conclusion

In this section the first observation of the CBS signal with ultracold atoms propagating in a disordered optical speckle potential was described. Due to the anisotropy of the speckle the dynamics of the atoms happen in a plane perpendicular to the speckle grains for short propagation times, and we can treat the system to be quasi 2-dimensional. In contrast to previous experiments where there is always a boundary between free space and disorder we are able to instantaneously immerse the waves in the scattering potential

simply by switching on the speckle. Also, we are able to directly observe the full evolution of the momentum space distribution. Next to the observation of the CBS peak this allows us to directly determine two fundamental transport parameters, the mean scattering time and the transport time.

We performed similar experiments to the ones described above while changing the disorder strength and the initial velocity of the atoms, which also led to the observation of CBS. Its maximum observed contrast did not change significantly while varying these parameters. The maximum width of the CBS peak on the other hand was found to increase with higher disorder amplitude and lower initial velocity. From the highest observed width of $\Delta\theta \sim 1.2$ rad we infer $k_i l_S \approx 1.2$, which indicates that we are not far from the strongly localized regime. But to observe Anderson localization longer propagation times than possible in this experimental setup would be necessary.

With the observations described in this section we showed that ultracold atoms are a powerful system to study the first order coherence corrections to wave transport in disordered media. Interesting further investigations include for example the effect of interactions on this problem: It was predicted that such non-linearities of the wave propagation can suppress the CBS peak, or even replace it with a dip, that is, a decreased probability to scatter in the backwards direction [51].

Other recent theoretical proposals transposed the scheme of observing the momentum space distribution to the strongly localized regime and predicted the appearance of another as yet unobserved peak in the forward direction, the Coherent Forward Scattering peak (CFS) [59, 79, 69, 46]. In numerical simulations it is shown to appear after the localization time, and to grow on the time scale of the Heisenberg time.⁵² A reproduction of a figure from [59] is given in figure 59.

Ultracold atoms also offer the possibility to study the underlying mechanism of CBS, namely the constructive interference of counter-propagating paths, which is based on the time-reversal symmetry of the wave propagation in the disorder. We performed such an experiment, which will be treated in the next chapter (Coherent Backscattering Revival - CBSR).

⁵²The Heisenberg time is connected to the localization volume l_{loc}^d and the average density of states per unit volume ν . Here, l_{loc} is the localization length and d is the dimensionality of the system. The Heisenberg time is given by $\tau_{\text{H}} = h\nu l_{\text{loc}}^d$, with h the Planck constant.

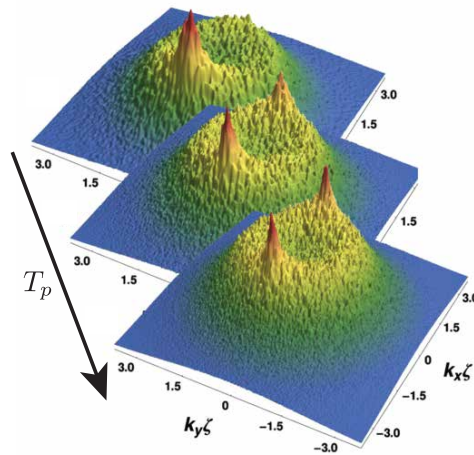


Figure 59: **Coherent Forward Scattering (CFS) in 2D.** For strong disorder the momentum space distribution reveals a second peak in forward scattering direction. Shown here is the reproduction of results of numerical calculations for increasing propagation time in the disorder [59].

8 Coherent Backscattering revival

It was already laid out in sections 2.5 and 7.1 that weak localisation (WL) and coherent backscattering (CBS) are the first order manifestations of coherent transport in disordered media. They are based on the constructive interference of counter-propagating paths, which acquire the same phase and therefore always interfere constructively. In the previous chapter our results of CBS were described, showing that with our experimental setup we are able to observe these quantum mechanical transport corrections. In this chapter the focus will be on the underlying symmetry between a pair of counter-propagating paths, which is at the heart of weak-disorder coherence effects. Namely, coherent backscattering and weak localisation can be observed if the propagation of waves in the disordered medium is symmetric with respect to time reversal, or more precisely if it obeys the weaker condition of reciprocity.⁵³

Indeed, one of the first experiments to observe the coherent quantum transport corrections used a controlled breaking of this symmetry to make the effect of weak localization visible: Sharvin and Sharvin [105] measured the resistance of a thin walled cylinder as a function of an applied magnetic field. The magnetic flux through the cylinder introduces a phase shift between counter-propagating paths. Since it does not introduce a decoherence between the different paths this leads to a periodic modulation of the weak localization correction, and consequently to a modulation of the measured resistance, see figure 60.⁵⁴

Following a theoretical proposal of T. Micklitz, C. Müller, and A. Altland [80] we attempted a new approach that benefits from the precise spatial and temporal control over the propagation of ultracold atoms in disorder: The experiment is very much like the one enabling us to observe the CBS peak described in the previous chapter. In contrast to the CBS experiment, here we deliberately introduce a dephasing between the counter-propagating paths without losing coherence. This dephasing is administered at a precise moment and only during a short time. As shown qualitatively in figure 61 the proposal predicted that this would lead to the suppression of the CBS peak for all times except for a moment when time-reversal symmetry is briefly re-established and the CBS peak briefly reappears.

This chapter will follow the following outline: A definition of the reci-

⁵³The difference between these two properties will be discussed in section 8.1.2. In the scope of our experiment they can be used interchangeably.

⁵⁴This oscillatory magnetoresistance behaviour was predicted by Altshuler, Aronov, and Spivak [7].

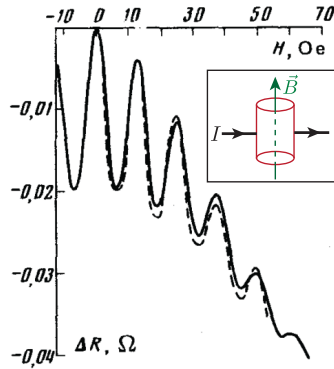


Figure 60: **Oscillations in resistance due to periodic dephasing.** This graph, reproduced from [8], shows the resistance to an electrical current I through a thin walled metal cylinder, as shown in the inset. The phase difference between counter-propagating closed electron loops around the cylinder is proportional to the strength of the magnetic field \vec{B} , leading to an oscillation of the resistance when the field strength is changed. The solid line are experimental data, and the dashed line is the theoretical prediction.

reciprocity and time-reversal symmetry for wave propagation in disordered media and their importance for WL and CBS is given in section 8.1. An overview of experiments that introduced a deliberate dephasing, that is a breaking of the reciprocity of the system, is given in section 8.2. The method by which we break time-reversal symmetry in our experiment is discussed in section 8.3, before a study of the expected dynamics of the system is given in 8.4. This is followed by the discussion of our experimental results in 8.5, which is complemented by numerical simulations shown in section 8.6.

8.1 Reciprocity and time reversal symmetry

It was already mentioned in section 7.1 that underlying the effects of Weak Localization and Coherent Backscattering is an inherent symmetry in the wave propagation in disordered media. Namely, it was necessary to make the assumption that two counter-propagating paths acquire the same phase and therefore interfere constructively. In this section this notion will be justified in a more precise manner. First, some basic notations regarding fundamental scattering theory is introduced. This lays the foundation on which the concept of *reciprocity* and its relation to *time reversal invariance*

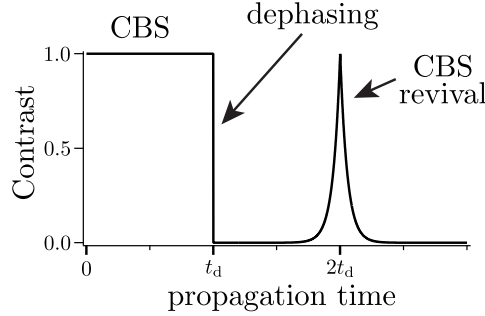


Figure 61: **Qualitative behavior of the CBS contrast with a brief dephasing pulse.** This graph shows the idealized evolution of the CBS contrast: Before the dephasing is administered ($t < t_d$) the contrast is at its usual value equal to 1. After the dephasing it is completely suppressed, except for a short time around $t = 2t_d$ when counter-propagating paths are again symmetric with respect to time reversal, and the CBS peak reappears.

in multiple scattering systems can be discussed.

8.1.1 Basic notations on scattering theory

In the following the very basic notions on scattering theory will be given. Full derivations of the results presented here can be found for example in [3]. We consider a simple system, depicted in figure 62 **a**, consisting of a plane wave incident on a single, localized obstacle described by a potential $V(\vec{r})$. The plane wave is characterised by a wave vector \vec{k}_i , and we are interested in a final state with a wave vector \vec{k}_f . In the far field, that is, for distances from the center of the scattering potential greater than its extent, the scattered wave will be spherical. Assuming that the center of the potential $V(\vec{r})$ is located at the origin the wave function can be written as:

$$\Psi(\vec{r}) = e^{i\vec{k}_i \cdot \vec{r}} + \frac{e^{ik_i r}}{r} f(\vec{k}_i, \vec{k}_f) \quad (70)$$

The first exponential describes the incoming plane wave. The second term is the spherical outgoing wave, multiplied by the scattering amplitude $f(\vec{k}_i, \vec{k}_f)$, that gives the amplitude of the scattering process into the final state \vec{k}_f . It is given by

$$f(\vec{k}_i, \vec{k}_f) = -\frac{m}{2\pi\hbar^2} \int d\vec{r} e^{-i\vec{k}_f \cdot \vec{r}} V(\vec{r}) \Psi(\vec{r}). \quad (71)$$

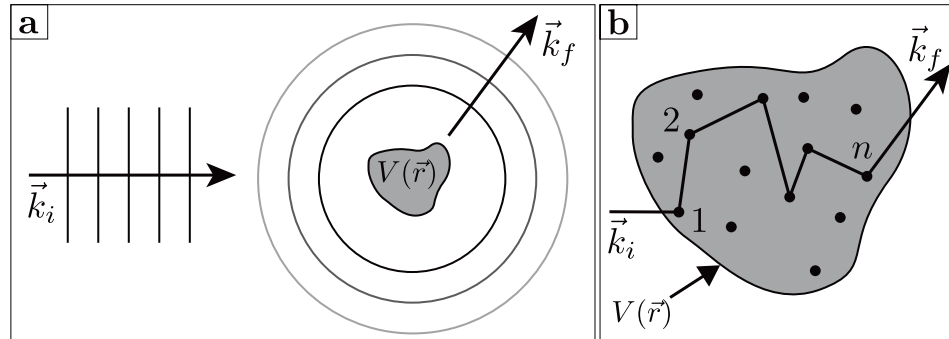


Figure 62: **Scattering process.** **a** An initial plane wave with wave vector \vec{k}_i is incident on a scattering potential $V(\vec{r})$. It is assumed that this obstacle is static and of finite size. Then, in the limit of distances greater than the size of the obstacle, the scattered wave will be spherical. The scattering amplitude (see text) links a final state \vec{k}_f to the initial state \vec{k}_i . **b** In the case of one particular multiply scattered path a final state \vec{k}_f is still linked to the initial state \vec{k}_i via a scattering amplitude. This scattering amplitude is only valid for the exact sequence of scattering events $1 \rightarrow n$.

Here, m is the mass of the particle associated with the quantum wave, and \hbar is the reduced Planck constant.⁵⁵ Since we have not specified the scattering potential $V(\vec{r})$ in any way other than that it should be zero as $|\vec{r}| \rightarrow \infty$, this solution already incorporates multiple scattering within the potential, which may be random. For the further discussion it is useful to single out one particular multiply scattered path, as shown in figure 62 **b**. In this case the final state \vec{k}_f will still be linked to the initial state \vec{k}_i by a scattering amplitude, but in addition to the initial and the final state it also depends on the sequence of the scattering events $\{1 \rightarrow n\}$ of this particular path, and will be denoted by $f(\vec{k}_i, \vec{k}_f, \{1 \rightarrow n\})$. The total scattering amplitude of equation 71 can be recovered by summing the partial scattering amplitudes of all multiple scattering paths that are involved in the process.

8.1.2 The reciprocity theorem

In very qualitative words, reciprocity of wave propagation means that “if I can see you, you can see me” [3, 115]. An example would be two people

⁵⁵The definition of the scattering amplitude is at the basis of the Born formalism of scattering.

separated by an absorbing fog: If person A can observe person B through the fog, then the reciprocal case of person B being able to observe person A is also true. An example of a non-reciprocal system is the optical isolator, a device that lets light pass only in one direction and blocks it in the other. A more precise definition of reciprocity is that the scattering amplitude defined in the previous section must be invariant when the inverse process is considered [3]:

$$f(\vec{k}_i, \vec{k}_f, \{1 \rightarrow n\}) = f(-\vec{k}_f, -\vec{k}_i, \{n \rightarrow 1\}) \quad (72)$$

On the left side the amplitude of the “direct” path is given, with initial state \vec{k}_i , final state \vec{k}_f , and scattering sequence $\{1 \rightarrow n\}$. On the right hand side the initial state is $-\vec{k}_f$, going through the inverse sequence of scattering events $\{n \rightarrow 1\}$, and ending up in the final state $-\vec{k}_i$ (compare with panel **b** in figure 62).

It is tempting to draw a parallel between reciprocity and time-reversal symmetry: Since the reversal of time transforms the momenta $\hbar\vec{k}$ into $-\hbar\vec{k}$ and inverts the sequence of scatterers it seems like the definition of reciprocity in equation (72) would be equivalent with the requirement of time-reversal symmetry of the wave propagation. In general, though, this is not the case: Employing again the example of the absorbing fog given above, the absorption breaks the time-reversal symmetry of the wave propagation, but it leaves reciprocity intact. In this case, a decrease of the wave’s amplitude due to absorption would be included in the scattering amplitude. Since the absorption would be the same for the direct and the reversed path the definition of reciprocity (72) is not violated.

In our experimental system there is no absorption. Under this circumstance it can be shown that reciprocity and time-reversal invariance are equivalent [3, 24]. In the following terms like “reciprocal path” and “time-reversed path” will therefore be used interchangeably.

8.1.3 Reciprocity and Coherent Backscattering

Reciprocity is the fundamental condition for Coherent Backscattering (and, equally, for Weak Localization). We have already argued in section 2.5 and 7.1 that the enhancement of the probability of direct backscattering (or the enhancement of the probability of return) comes from the constructive interference between multiply scattered, counter-propagating paths. We can now justify this by using the reciprocity theorem: Equation (72) is valid in a medium where reciprocity is observed. Combining it with the condition

8.2 Previous experiments on CBS and time-reversal invariance of wave propagation in complex media

of direct backscattering $\vec{k}_f = -\vec{k}_i$ gives:

$$f(\vec{k}_i, -\vec{k}_i, \{1 \rightarrow n\}) = f(\vec{k}_i, -\vec{k}_i, \{n \rightarrow 1\}) \quad (73)$$

This means that in a medium that observes reciprocity the scattering amplitudes of time-reversed paths are exactly the same. Since the initial and final states are the same these amplitudes have to be added, and since the acquired phase is the same the resulting interference is always constructive.

8.2 Previous experiments on CBS and time-reversal invariance of wave propagation in complex media

In order to provide the context for our experiments on the Coherent Backscattering Revival the following section contains an overview of related works by other groups. The common element of the experiments listed here is that they specifically view coherent transport phenomena with an emphasis on time-reversal symmetry. They can be combined into two groups:

- The time-reversal symmetry of propagation in complex and disordered media was tested with so called time-reversed mirrors, pioneered by the group of M. Fink. These record the response of a wave after propagation in a disordered potential, and can then generate a time-reversed wave form of this recording. This time-reversed wave then propagates through the same disorder and converges to recreate the initial wave form. Although conceptually quite similar to coherent backscattering, the counter-propagating wave packets in these experiments have different sources and don't propagate in the disorder at the same time.
- The other conceptual group of experiments are closer to our setup in that they observe real weak localisation or coherent backscattering. That is, in their setups the counter-propagating wave packets have the same source, propagate in the disorder at the same time, and interfere with each other. In these experiments the time-reversal symmetry between the counter-propagating paths is broken by methods appropriate to the system in question. This manifests itself in a dephasing or in decoherence, and therefore in a reduction of the constructive interference between these paths.

8.2.1 Time reversal mirrors

In a typical time-reversal mirror experiment first a short, broadband wave is generated at a point A . This wave then propagates and is scattered by

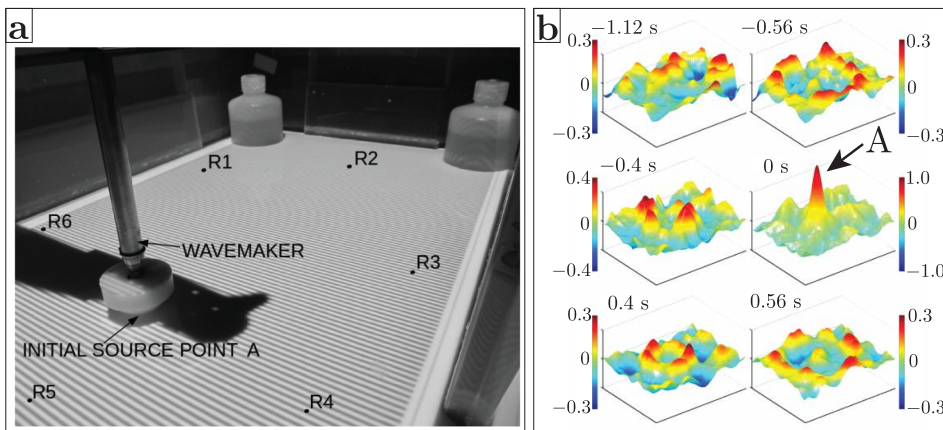


Figure 63: **Refocussing using Time Reversal Mirror** (Reproduced from [95].) Panel **a** shows the experimental setup: An initial surface water wave is produced by a wavemaker at point A, propagates in a reverberating cavity, and is recorded at points R1-R6. At these points the time-reversed recorded waveform is then re-emitted. The wave then retraces its evolution until it converges at its original source point A, shown in panel **b** (the temporal focus is at 0 s).

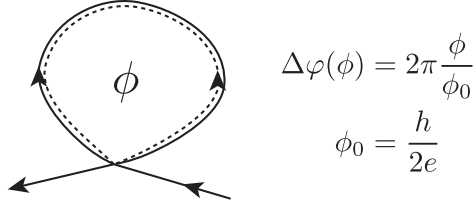


Figure 64: **Dephasing in weak localization of electrons due to an external magnetic field.** The phase difference $\Delta\varphi$ between a pair of counter-propagating loops is determined by the magnetic flux ϕ through the loop.

obstacles or the boundaries of a reverberating cavity, leading to a chaotic global wave form. This chaotic wave pattern is recorded at some fixed points R_i . When the wave form recorded at all points R_i is then time-reversed and re-emitted it will exactly retrace its evolution and recreate the short initial wave at point A . Since this initial wave is typically well defined in space and time one speaks of temporal and spatial focusing accomplished by time-reversal mirrors. An example is given in figure 63, where the evolution of a time-reversed water wave around the source point A is shown.

Such time-reversal experiments have been carried out using acoustic waves [39, 43, 65], electromagnetic waves [73], and surface water waves [95]. The topic of time-reversal mirrors has potential practical applications, for example in biomedicine [44] and telecommunications [73]. But it also carries a fundamental interest, since it shows the time-reversability of wave propagation even in complex media. Its connection with Coherent Backscattering is discussed in [37].

8.2.2 Previous experiments on the deliberate breaking of time-reversal symmetry

In this section an overview of experiments is presented that investigated the effect of time-reversal symmetry breaking on coherent backscattering or weak localisation. They are combined into groups, each one highlighting the mechanism by which the breaking of TRS was achieved.

Magneto-Resistance In electronic systems the electron wave function propagates in a lattice potential and is scattered for example by impurities

8.2 Previous experiments on CBS and time-reversal invariance of wave propagation in complex media

and dislocations in this crystal. In the presence of an external magnetic field the electrons couple to its magnetic vector potential \vec{A} , which induces an additional phase. This phase has opposite signs for the direct and the counter-propagating paths, showing that time-reversal symmetry is broken. The total phase difference induced by the magnetic flux is

$$\Delta\varphi = 2\pi \frac{\phi}{\phi_0}, \quad (74)$$

where $\phi_0 = h/(2e)$ with h the Planck constant and e the electron charge (see figure 64). It was already mentioned in the introduction of this chapter that this effect was observed in thin walled metallic cylinders [105, 8] (see figure 60). Here, the dephasing leads to a periodic modulation of the weak localization correction since the loops are geometrically confined to the cylinder and therefore enclose the same magnetic flux.⁵⁶ As a side note, it is a testament of the importance of Weak Localization that the exact same experiment was conducted nearly two decades later, only this time using carbon nano-tubes, and still gain a lot of traction [15].

An anomalous behaviour of the resistance is also observed in thin metallic films (see [18] and references therein). The impact is biggest if the magnetic field is perpendicular to the film, and WL corrections monotonically disappear with increasing field strength as shown in figure 9. The dependence of the resistance on the magnetic field here is not periodic since in the thin film loops of different sizes exist, each of which encloses a different magnetic flux for a given magnetic field strength.

Faraday Rotation A partial destruction of the Coherent Backscattering cone was observed in optical experiments making use of the Faraday Effect (FE): By the FE a rotation of the polarisation of light can be achieved by applying a magnetic field to a magneto-optically active material through which the light passes. This effect is employed for example in optical isolators, where the reciprocity breaking by the FE is very apparent: Light can

⁵⁶The origin of this phase is the Aharonov-Bohm effect [2]. In the original experiments on the AB effect, which were performed using an electron beam in vacuum where no scattering occurs, a period of h/e was observed [87]. This periodicity can persist even in scattering media, as shown by Webb *et al.*, where the resistance over a thin ring was measured as a function of the magnetic flux through the ring [118]. In the aforementioned experiments by Sharvin and Sharvin, and by Altshuler *et al.* the long cylinder can be thought of as an ensemble of independent rings, where where the inherent disorder averaging smoothes out the h/e periodicity and makes the $h/2e$ periodicity linked to weak localization apparent.

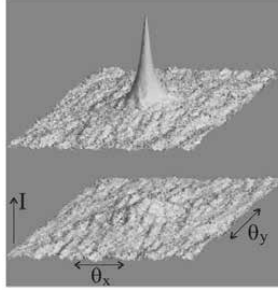


Figure 65: **Suppression of the CBS peak through the Faraday Effect.** In a magneto-optically active medium the time-reversal symmetry can be broken due to the Faraday Effect (see text). This was used in experiments to dephase counter-propagating paths with respect to each other, leading to a suppression of the CBS peak. The image is reproduced from [72]. On top, a fully developed CBS peak is obtained when no magnetic field is present and TR symmetry is observed. The bottom image shows the nearly complete suppression due to the breaking of the TR symmetry due to a present magnetic field.

pass the isolator only in one direction, whereas it is blocked when coming from the opposite direction. In other words, a given beam of light may pass, whereas its time-reversed counterpart is blocked. This is due to the fact that the induced rotation of the polarisation only depends on the direction of the magnetic field, and not the propagation direction of the light.

As first proposed by [47, 76] and experimentally observed by [40, 72], a circularly polarised light beam was sent into a magneto-optically active multiple scattering medium that exhibits the FE. The coherent backscattering peak was then measured for different strengths of the applied magnetic field permeating the medium. The time-reversal symmetry was (partly) broken since the phase-shifts induced by the FE have different signs for the counter-propagating paths. Short paths, which give the broad contribution to the CBS cone, are less affected by this dephasing. Long paths on the other hand, which interfere in a narrow peak, could be completely dephased.

Change of Refractive Index A different approach to break the TRS in optical systems was very recently taken by Muskens *et al.* [84]. Here, the setup consisted of a diffusive medium whose refractive index could be changed by shining a femto-second pulsed laser (pump) on it. The CBS

contrast of a second pulsed beam (probe) was measured as a function of the delay between the pump and the probe beam impinging on the medium.

The time during which the nonlinear medium changes its refractive index to the excited state is shorter than the typical dwell time of the probe beam photons in the medium. The time it takes the medium to relax to its initial state on the other hand is long compared to the dwell time of the probe photons. Time reversal symmetry breaking between counter-propagating paths was therefore achieved by changing the refractive index while the photons were already propagating in the medium. The maximum observed reduction of the CBS contrast was 12%.

The similarity between this experiment and our work is that there is a control over the time when the breaking of reciprocity is induced. But contrary to our experiments this disturbance happens during an appreciable part of the total propagation, whereas in our case it is shortly peaked. Moreover, the reciprocity breaking here is due to decoherence of the wave propagation, whereas in our case coherence is preserved.

8.3 Breaking of time-reversal symmetry by short perturbations

The novel approach in our experiments in regards of the breaking of time-reversal symmetry between counter-propagating paths is that the dephasing mechanism is applied during a time very short compared to all other time-scales of the experimental system, while leaving the medium unchanged at all other times. More specifically, the time-reversal symmetry is broken while preserving coherence by applying a shortly pulsed, position dependent potential. In general this leads to a destruction of the constructive interferences and a disappearance of the CBS peak. Time-reversal symmetry can be briefly re-established though when the dephasing potential is applied exactly halfway through the propagation. In this case the dephasing briefly vanishes and a revival of the coherent backscattering peak is expected. This procedure was proposed and brought to our attention by T. Micklitz, C. Müller, and A. Altland [80].⁵⁷

8.3.1 Perturbative picture

We first focus on a perturbative approach, where to first order the application of the dephasing potential does not alter the trajectories of the

⁵⁷The proposal also covers more involved sequences of dephasing pulses, which lead to the revival of higher order quantum corrections.

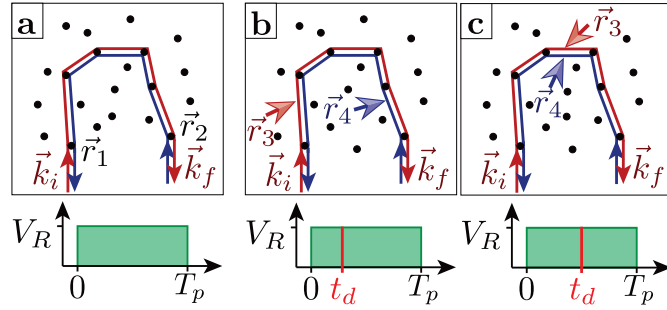


Figure 66: **TRS Breaking and Recovery.** Panel **a** shows the configuration without any dephasing between the counter-propagating paths (red and blue), where the CBS peak is visible. The direct path enters with an initial wave vector \vec{k}_i at \vec{r}_1 and exits the disorder at \vec{r}_2 after a propagation time in the disorder T_p with wave vector \vec{k}_f . Panels **b** and **c** show that when the short dephasing potential is applied at time t_d the direct and reciprocal paths are at positions \vec{r}_3 and \vec{r}_4 respectively. Whereas $\vec{r}_3 \neq \vec{r}_4$ in panel **b** and the time-reversal symmetry between the paths is broken, in panel **c** one has $\vec{r}_3 = \vec{r}_4$ and TRS is re-established. Experimentally, panel **b** shows a situation in which the CBS peak is suppressed, and panel **c** shows a situation in which the CBS peak reappears (CBSR). Below each panel the duration of the speckle potential with amplitude V_R and the moment of dephasing t_d is shown. TRS is re-established for $t_d = T_p/2$.

atoms and only has an impact on the quantum phases. Figure 66 shows the schematic representation of a pair of counter propagating paths in the disorder. Arbitrarily the red path will be called the direct, and the blue path will be called the reciprocal path. As indicated in panel **a** the direct path enters the disorder at time $t = 0$ and at the spatial point \vec{r}_1 , and exits it after the total propagation time T_p at \vec{r}_2 . The incoming wave is characterised by its wavevector \vec{k}_i , and \vec{k}_f is the wavevector of the outgoing wave. It was already pointed out in section 7.1 that in absence of any additional dephasing the phase-difference between these two paths is given by

$$\Delta\phi_{CBS} = \vec{q} \cdot (\vec{r}_1 - \vec{r}_2), \quad (75)$$

where \vec{q} is the sum between the incoming and the outgoing wavevectors, $\vec{q} = \vec{k}_i + \vec{k}_f$. In the pure CBS case depicted in panel **a** of figure 66, that is, without any additional dephasing, it suffices to require direct backscattering ($\vec{q} = 0$) to ensure zero phase difference and constructive interference.

The position dependent potential in our experiment is realised by a magnetic gradient field along the y-axis, $V_d = -Fy$, where F characterises the slope of the gradient, equal to the force experienced by the atoms. It is assumed that this gradient is homogeneous, that is, the force is constant and independent of position. The gradient is applied for a short delta-like pulse with length Δt , leading to a change of the momentum of the atoms of $\Delta\vec{p} = \hbar\Delta\vec{k} = F\Delta t\vec{e}_y$, where \vec{e}_y is the unit vector in y-direction.⁵⁸ As depicted in panels **b** and **c** of figure 66 the direct path is at some position \vec{r}_3 , and the reciprocal path is at position \vec{r}_4 when this gradient potential is applied. The phase that is acquired in the time Δt due to the potential V_d for the direct path is $V_d(\vec{r}_3)\Delta t/\hbar$, and analogously for the reciprocal path. Since the acquired phase is position dependent we therefore have a phase difference that depends on the momentary position of the direct and its reciprocal path:

$$\begin{aligned} \Delta\phi_{deph} &= [V_d(\vec{r}_4) - V_d(\vec{r}_3)]\Delta t/\hbar \\ &= \Delta\vec{k} \cdot (\vec{r}_3 - \vec{r}_4) \end{aligned} \quad (76)$$

In the perturbative regime the total phase difference between the counter-propagating paths is the sum of the normal CBS phase (75) and the dephasing (76):

$$\begin{aligned} \Delta\phi &= \Delta\phi_{CBS} + \Delta\phi_{deph} \\ &= \vec{q} \cdot (\vec{r}_1 - \vec{r}_2) + \Delta\vec{k} \cdot (\vec{r}_3 - \vec{r}_4) \end{aligned} \quad (77)$$

⁵⁸This momentum change serves to characterise the perturbative picture, which is valid if $\Delta p \ll \hbar k_i$.

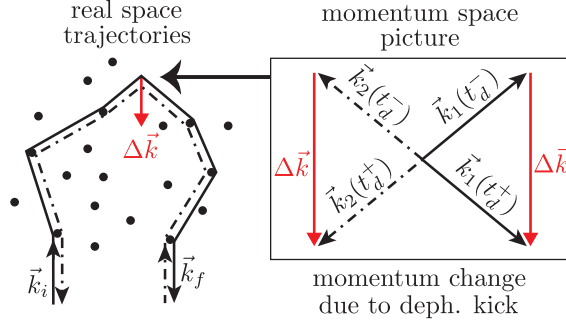


Figure 67: **Re-establishment of TRS for strong perturbations.** In the case of strong perturbations the trajectories are strongly altered by the dephasing potential as shown on the left hand side picture. Nevertheless there are still paths symmetric under time reversal at $T_p = 2t_d$ (see text). The momentum of the direct path just before the dephasing pulse denoted by $\vec{k}_1(t_d^-)$, and just after the pulse by $\vec{k}_1(t_d^+)$. Similarly the momenta for the reciprocal path are $\vec{k}_2(t_d^-)$ and $\vec{k}_2(t_d^+)$.

Contrary to the pure CBS case the backscattering condition $\vec{q} = 0$ is no longer sufficient to ensure that the phase difference becomes zero, and the constructive interferences that usually lead to the CBS peak are washed out. But by adding an additional constraint, $\vec{r}_3 = \vec{r}_4$, the phase difference again becomes zero. As shown in panel c of figure 66 this condition is naturally fulfilled when the dephasing potential is applied at exactly half the total propagation time in the disorder, $t_d = T_p/2$.

8.3.2 Extension to strong perturbations

For reasons that will be laid out later in section 8.5.2 our experiments are not performed in the perturbative regime. In fact, the change in momentum is on the order of the initial momentum, implying that the trajectories are strongly altered by the dephasing potential. Nevertheless the main arguments outlined above still hold. In particular, time-reversal symmetry between counter-propagating paths is re-established at $T_p = 2t_d$ as shown in figure 67 for paths whose absolute values of their momenta are not changed by the perturbation. Writing explicitly and using the notation in figure 67

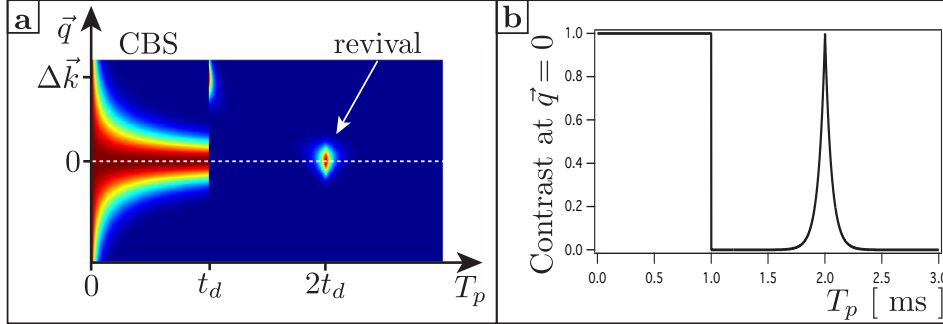


Figure 68: **Contrast as a function of \vec{q} and T_p .** Using equation (79) the evolution of the contrast as a function of the momentum \vec{q} and the propagation time T_p can be evaluated in the approximation of diffusive transport. Here, experimentally realistic parameters are used: The time of the dephasing pulse is $t_d = 1$ ms, the strength of the pulse is $\Delta\vec{k} = 2.5 \mu\text{m}^{-1}$, and the diffusion constant is $D = 2.88 \mu\text{m}^2/\text{ms}$. Panel **a** shows the contrast as a function of \vec{q} and T_p , whereas panel **b** shows the contrast only as a function of T_p for $\vec{q} = 0$ (“on-shell”). In order to show the evolution before the dephasing pulse the term $\Delta\vec{k}$ in equation (79) was set to zero for $T_p < t_d$.

this means that:

$$\begin{aligned} \vec{k}_1(t_d^-) + \Delta\vec{k} = \vec{k}_1(t_d^+) &= -\vec{k}_2(t_d^-) \\ \vec{k}_2(t_d^-) + \Delta\vec{k} = \vec{k}_2(t_d^+) &= -\vec{k}_1(t_d^-) \end{aligned} \quad (78)$$

A revival of the CBS peak is then also expected in the regime of strong perturbations of the trajectories.

8.4 Expected dynamics of the system

T. Micklitz, C. Müller, and A. Altland carried out a theoretical study of the dynamics of the coherent contribution to the momentum distribution in the perturbative regime described above [80]. These calculations were carried out under the assumption of diffusive propagation, where the average distance covered by an atom in the disorder in a time t is $\langle d \rangle_t = \sqrt{2Dt}$, with D the diffusion constant.⁵⁹ Therefore a discussion based on the diffusive approximation will be given here, which at least qualitatively reproduces all

⁵⁹Since our experiments are carried out on time scales on the order of the transport time, the propagation of the atoms is ballistic or in the transition regime between ballistic

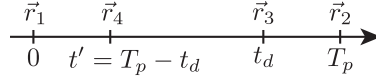


Figure 69: **Schematic of the spatial points and the corresponding times during the propagation.**

effects we observe. An exception is the evolution of the on-shell contrast ($\vec{q} = 0$), the central quantity we extract experimentally. For this instance we were able to derive an expression for the regime of ballistic propagation (see section 8.4.1).

The contrast of the coherent contribution to the momentum distribution (including CBS and CBS revival) as a function of the momentum $\vec{q} = \vec{k}_i + \vec{k}_f$ at total propagation time T_p is given by⁶⁰

$$C(\vec{q}, t') = e^{-D(2\vec{q}^2 t' + (\vec{q} - \Delta\vec{k})^2 |t_d - t'|)}. \quad (79)$$

The time t' is related to the total propagation time T_p and the time of the dephasing pulse t_d by $t' = T_p - t_d$. A plot of the contrast $C(\vec{q}, t')$, and a plot for the contrast at $\vec{q} = 0$ for experimentally realistic parameters is shown in figure 68.

Before analysing this equation we want to show how to derive it in a naïve way. First, the probability to diffuse from a spatial point \vec{r} to another point \vec{r}' within a time t is:⁶¹

$$P(\vec{r}, \vec{r}', t) = \frac{1}{4\pi Dt} e^{-\frac{(\vec{r} - \vec{r}')^2}{4Dt}} \quad (80)$$

Using the conventions shown in figure 66 we will assume that the direct path starts at time $t = 0$ at point \vec{r}_1 , and ends at point \vec{r}_2 after the total propagation time T_p (see also figure 69). The dephasing potential will be switched on in a delta-like pulse at time t_d . At this moment the direct path will be at some point \vec{r}_3 , and the reciprocal path at \vec{r}_4 . With these conventions we can piece together the evolution within the disorder going through the points \vec{r}_1 , \vec{r}_2 , \vec{r}_3 , and \vec{r}_4 as the product of the corresponding probabilities, $P(\vec{r}_1, \vec{r}_4, t') \cdot P(\vec{r}_4, \vec{r}_3, t_d - t') \cdot P(\vec{r}_3, \vec{r}_2, t')$. Assuming that the starting point of the direct path \vec{r}_1 is fix we have to integrate over all possible

and diffusive motion. A full theoretical treatment of our experimental situation is still lacking.

⁶⁰Private communications with T. Micklitz *et al.*

⁶¹It is assumed here that the system is 2D, as is the case in our experiments.

points $\vec{r}_2, \vec{r}_3, \vec{r}_4$ and multiply with the phase difference between the direct and the reciprocal path given in equation (77) to recover the contrast:

$$\begin{aligned} C(\vec{q}, t') &= A \int d\vec{r}_2 d\vec{r}_3 d\vec{r}_4 e^{-\frac{(\vec{r}_1 - \vec{r}_4)^2}{4Dt'}} e^{-\frac{(\vec{r}_4 - \vec{r}_3)^2}{4D(t_d - t')}} e^{-\frac{(\vec{r}_3 - \vec{r}_2)^2}{4Dt'}} e^{i\Delta\vec{k} \cdot (\vec{r}_3 - \vec{r}_4) + i\vec{q} \cdot (\vec{r}_1 - \vec{r}_2)} \\ &= e^{-D(2\vec{q}^2 t' + (\vec{q} - \Delta\vec{k})^2 |t_d - t'|)} \end{aligned} \quad (81)$$

The normalisation factors of the form $1/(4\pi Dt)$ in the first line are condensed into A , and they cancel out with the integrations.

8.4.1 Evolution of the contrast in direct backscattering direction

When looking at the direct backscattering direction $\vec{q} = 0$ formula (79) simplifies to (compare with panel **b** of figure 68)

$$\begin{aligned} C(\vec{q} = 0, t') &= e^{-D\Delta\vec{k}^2 |t_d - t'|} \\ &= e^{-|T_p - 2t_d|/\tau_R}, \end{aligned} \quad (82)$$

where the relation $t' = T_p - t_d$ was used. The characteristic time of the revival is $\tau_R = (D\Delta\vec{k}^2)^{-1}$. This means that the the phases of the counter-propagating paths, which are initially scrambled by the dephasing pulse, align again perfectly at the revival time $2t_d$. The contrast rises exponentially to its maximum value of one before falling exponentially again for longer propagation times.

This particular result, the evolution of the contrast at $\vec{q} = 0$, can also be understood intuitively starting from the phase difference between the counter-propagating paths $\Delta\Phi_{tot}$ given in equation (77): For $\vec{q} = 0$ one has $\Delta\Phi_{tot}|_{\vec{q}=0} = \Delta\vec{k} \cdot (\vec{r}_3 - \vec{r}_4)$. The positions \vec{r}_3 and \vec{r}_4 are where the direct and the reciprocal trajectories find themselves when the dephasing pulse is applied. The distance between these two points $\langle d \rangle$ and the time t it takes to propagate between them in the diffusive regime are related by $\langle d \rangle_t = \sqrt{2Dt}$. Assuming that the interference between the counter-propagating paths becomes appreciable when $\Delta\Phi_{tot}|_{\vec{q}=0} \leq 1$ leads to an estimation of the revival time:

$$\begin{aligned} \Delta\Phi_{tot}|_{\vec{q}=0} &= \Delta k \sqrt{2Dt} \leq 1 \\ \Rightarrow t &= (2D\Delta k^2)^{-1} \approx \tau_R \end{aligned} \quad (83)$$

This result for the characteristic time of the revival τ_R differs only by a factor 1/2 from the proper theoretical result given above.

We use this intuitive understanding to modify the behavior of the contrast around the revival time to obtain a description for ballistic propagation: Following the arguments given above one can write in general that

$$C(\vec{q} = 0, T_p) = e^{-\frac{1}{2}\Delta k^2 \langle d \rangle_{|T_p - 2t_d|}^2}. \quad (84)$$

In the diffusive case this reduces to equation (82). For ballistic propagation one has $\langle d \rangle_t \sim vt$, therefore leading to a gaussian evolution of $C(\vec{q} = 0, t')$ around the revival time. More precisely, a theoretical treatment of the initially ballistic propagation gives $\langle d \rangle_t = v_i t / 3$ [49], leading to

$$\begin{aligned} C(\vec{q} = 0, T_p) &= e^{-\frac{1}{18}\Delta k^2 v_i^2 (T_p - 2t_d)^2} \\ &= e^{-(T_p - 2t_d)^2 / (2\tau_R^2)} \end{aligned} \quad (85)$$

with τ_R again the characteristic time of the revival. Here though, it is the RMS width of a gaussian and given by $\tau_R = 3/(\Delta k v_i)$. We use this formulation later in the analysis and interpretation of our data.

8.4.2 Momentary shift of the momentum distribution

One can see in panel **a** of figure 68 that just after the kick the CBS peak is briefly shifted by $\Delta \vec{k}$.⁶² This behavior is evident when evaluating equation (79) just after the kick was applied at $T_p = t_d^+ \Leftrightarrow t' = 0^+$:

$$C(\vec{q}, t' = 0^+) = e^{-D(\vec{q} - \Delta \vec{k})^2 t_d} \quad (86)$$

The contrast, initially located at $\vec{k}_i + \vec{k}_f = \vec{q} = 0$ therefore momentarily has its maximum value at $\vec{q} = \Delta \vec{k}$. Following this momentary perturbation the incoherent momentum distribution will redistribute until it is symmetric around zero for longer propagation times (greater than some τ^*) in the disorder.

8.4.3 Evolution of the coherent contribution between dephasing and revival

The coherent peak moves from the initial position just after the dephasing pulse $\vec{q} = \Delta \vec{k}$ at $T_p = t_d^+$ to the position of its revival $\vec{q} = 0$ at $T_p = 2t_d$.⁶³

⁶²In fact, this shift applies to the whole momentum distribution and not just its coherent contribution. It can be clearly seen in our experimental data, see figure 73.

⁶³This is not obvious in figure 68 due to the choice of parameters.

To extract this movement the equation $\vec{\nabla}_{\vec{q}} C(\vec{q}, t') = 0$ has to be solved:

$$\begin{aligned} \vec{\nabla}_{\vec{q}} C(\vec{q}, t') &= C(\vec{q}, t') \left(-D \left(4\vec{q}t' + 2(\vec{q} - \Delta\vec{k})|t_d - t'| \right) \right) = 0 \\ \Rightarrow \vec{q}_{max} &= \Delta\vec{k} \frac{t_d - t'}{t_d + t'} \\ &= \Delta\vec{k} \frac{2t_d - T_p}{T_p} \end{aligned} \quad (87)$$

\vec{q}_{max} is the position where the effect of the dephasing is minimal, and the coherent contribution to the momentum distribution is maximal. Combining this result for the position of the maximum contrast \vec{q}_{max} with equation (79) gives the evolution of the maximum contrast at all propagation times:

$$\begin{aligned} C(\vec{q}_{max}, t') &= \exp \left(-2D\Delta\vec{k}^2 t' \frac{t_d - t'}{t_d + t'} \right) \\ &= \exp \left(-2D\Delta\vec{k}^2 (T_p - t_d) \frac{2t_d - T_p}{T_p} \right) \end{aligned} \quad (88)$$

In the framework of diffusive propagation that is employed here we see that the contrast drops rapidly after the dephasing pulse, reaching its minimal value at $T_p = \sqrt{2}t_d$.

8.4.4 Comparison between the CBS and the CBS Revival peak

One can compare the width of the CBSR peak in momentum space with the width of a CBS peak at the same time. It was shown in section 7.3.3 that the CBS peak in the diffusive approximation has a gaussian shape, with a width of $\sigma_{CBS}(T_p) = (2DT_p)^{-1/2}$. By setting $t' = t_d \Leftrightarrow T_p = 2t_d$ in equation (79) one gets

$$\begin{aligned} C(\vec{q}, t' = t_d) &= e^{-2Dt_d\vec{q}^2} \\ &= e^{-DT_p\vec{q}^2} \\ &= e^{-\frac{\vec{q}^2}{2\sigma_{CBSR}^2}}, \text{ with } \sigma_{CBSR}(T_p) = (2DT_p)^{-1/2}. \end{aligned} \quad (89)$$

The shape and width of the CBSR peak at the revival time is therefore exactly the same as that of the CBS peak after an equal propagation time. This can be understood intuitively, since at the revival time the dephasing that was induced between the counter-propagating paths vanishes. The situation then briefly resembles that of a pure CBS case.

8.4.5 Summary of the dynamics

To summarise, the CBS peak is momentarily shifted by $\Delta\vec{k}$ just after the dephasing pulse at time $T_p = t_d$. Next, the coherent peak moves from $\vec{q} = \Delta\vec{k}$ to $\vec{q} = 0$ within a time t_d . During this movement its contrast first decreases until reaching a minimum at time $T_p = \sqrt{2}t_d$, then increases again. Looking only at the position $\vec{q} = 0$ the evolution of the contrast is exponential, with a time constant τ_R that is proportional to the inverse of the diffusion constant D and to the inverse of the square of the strength of the dephasing pulse $\Delta\vec{k}$. For even longer propagation times the contrast decreases asymptotically towards zero, while continuing its motion.

It should be noted again that the dynamics presented here stem from calculations carried out in the perturbative regime $\Delta k \ll k_i$ and in the approximation of diffusive propagation. Both requirements are not fulfilled in our experiments, and the derived behavior therefore does not describe our experimental findings quantitatively. Nevertheless, the qualitative results of the dynamics of the coherent contribution to the momentum distribution, namely the existence of the CBS revival, the movement, and the decrease in contrast between the dephasing pulse and the revival still hold.

8.5 Experimental observation of the CBS Revival

After the theoretical investigations of the CBSR dynamics in the previous section we present here the experimental results we obtained. These experiments were carried out after the completion of the modifications of our experimental setup, which were described in section 5. Although no fundamentally new capabilities with respect to the previous setup were added, we nevertheless profited from increased flexibility. In particular, in the old setup it would have been difficult to implement the coil for the magnetic dephasing field due to mechanical constraints.⁶⁴

In the following the experimental sequence is laid out in section 8.5.1, after which we present the raw data and the analysis procedure employed to extract the coherent peak in section 8.5.2.

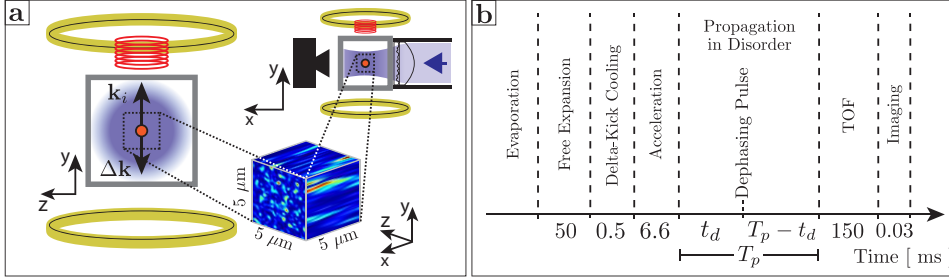


Figure 70: **CBS Revival experimental setup and sequence.** Panel **a** shows the experimental setup. Except for the additional dephasing coil (red, above the glass cell) it is similar to the setup we used for our experiments on CBS (see figure 52). In panel **b** the different steps of the CBS Revival experimental sequence are shown. The duration of each step are indicated on the time axis.

8.5.1 Experimental sequence

The experimental sequence employed to observe the revival of the coherent backscattering peak is nearly identical to the one for our CBS experiments, already detailed in section 7.2 (compare panels **b** of figures 52 and 70): We prepare a cloud of non-interacting atoms with a very well defined initial momentum $\vec{p}_i = \hbar\vec{k}_i$. This cloud is then exposed to the disordered potential by abruptly switching on the optical speckle (see section 4). As laid out in section 7.3.1, since the speckle is anisotropic the redistribution of the momenta for short propagation times happens mainly in the $y-z$ plane, perpendicular to the optical axis of the speckle. The dynamics can therefore be considered to be two dimensional. The momentum distribution after a propagation time T_p in the disorder is measured by a standard time of flight method, where the velocity distribution of the atoms at T_p is transformed into a position distribution and recorded via fluorescence imaging.

A sketch of the experimental setup is shown in panel **a** of figure 70. The modification compared with the pure CBS sequence is the application of a shortly pulsed magnetic gradient field $V_d(\vec{r})$ during the propagation in the disorder, produced by coils close to the atoms.⁶⁵ A current of > 100 A

⁶⁴The place where we installed this magnetic coil used to be occupied by the vertical speckle arm. This arm was physically connected to the horizontal arm, and removing one without the other would have proven difficult. In the new setup both arms are mechanically independent, and the vertical one was simply removed for this experiment.

⁶⁵The distance between the coil and the atoms is about 1-2 cm, limited by the dimensions

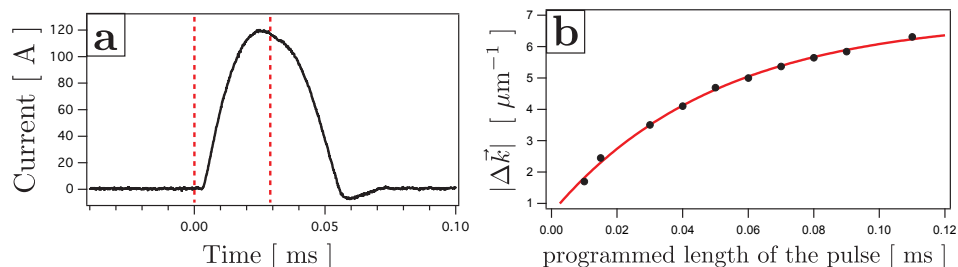


Figure 71: **Characterisation of the dephasing pulse.** Panel **a** shows the current flowing through the dephasing coil. The programmed length was $29 \mu\text{s}$, with the intended beginning and end indicated by the red dashed lines. There is a certain delay, and the pulse is broader than programmed. Panel **b** shows the strength of the dephasing pulse $|\Delta\vec{k}|$ as a function of its programmed length. A heuristic exponential fit $A \exp(t/\tau) + B$ is indicated in red. Since the current stems from the discharge of a capacitor the dephasing pulse becomes less effective for longer times as the capacitor becomes discharged and the current of the pulse tends towards zero.

could be switched on and off for a duration on the order of $10 \mu\text{s}$, providing a peak magnetic gradient of about 100 G/cm .⁶⁶ With the atoms in the $F = 2, m_F = -2$ hyperfine ground state this translates to an acceleration of about $10 g$ ($g \approx 9.81 \text{ m/s}^2$). The strength of the dephasing pulse $\Delta\vec{k}$ can be adjusted by changing the time for which current is running through the dephasing coil and the magnetic gradient field is acting on the atoms. The corresponding characterisation is shown in figure 71. There is a certain delay of about $20 \mu\text{s}$ until the current reaches its maximum value due to the interplay of the capacitor that serves as the power supply for the pulse, and the inductance of the circuit. The same delay is visible when switching the current off. There is a limit to its strength of $|\Delta\vec{k}| \approx 6 - 7 \mu\text{m}^{-1}$ for a pulse duration of $> 0.1 \text{ ms}$. This is due to the capacitor being depleted and the current running through the dephasing coil tending towards zero for long pulses.

of the vacuum glass cell containing the atoms.

⁶⁶This quick delivery of high currents was accomplished by closing the circuit consisting of the coil and precharged 1kV capacitors.

8.5.2 Presentation of the data and analysis

Motivation for the choice of the experimental parameters As explained in section 7.4 the time we are able to observe the CBS peak is limited due to the initial size and momentum spread of our atomic cloud, and the inevitable redistribution of the momenta out of the 2D plane for long propagation times. We therefore changed the key parameters that influence this maximum observation time to set ourselves in optimal conditions with the longest visibility.

Calling the characteristic limiting time due to the initial size and momentum spread of the atoms $\tau_{\Delta k}$, and the characteristic time of the redistribution of the momenta out of the 2D plane τ_{3D} we therefore strive to maximise the ratios $\tau_{\Delta k}/\tau^*$ and τ_{3D}/τ^* (τ^* is the 2D transport time). The influencing parameters which we can control experimentally are the disorder amplitude V_R , the initial momentum $\hbar k_i$, and finally the anisotropy of the speckle grains $\sigma_{\perp}/\sigma_{\parallel}$.

First, assuming a given anisotropy of the speckle, it is advantageous to be in the regime of isotropic scattering $k_i\sigma_{\perp} \approx 1$, which maximises τ_{3D}/τ^* . This fixes the initial velocity of the atoms. Second, in order to maximise $\tau_{\Delta k}/\tau^*$ a high disorder amplitude has to be chosen.⁶⁷

To change the anisotropy of the speckle we change the numerical aperture NA of the speckle system: Since the longitudinal size of the autocorrelation function of the speckle potential depends on the numerical aperture NA of the speckle system as $\sigma_{\parallel} \sim 1/NA^2$, whereas its transverse size changes as $\sigma_{\perp} \sim 1/NA$ a smaller numerical aperture leads to a bigger overall size of the speckle grains, and a higher anisotropy $\sigma_{\parallel}/\sigma_{\perp} = 1/NA$ (see section 4).⁶⁸

Experimentally we performed CBS experiments for different speckle numerical apertures while observing the considerations for $\tau_{\Delta k}$ and τ_{3D} given above. In each case the maximum CBS observation time was compared with the transport time, in order to find the configuration in which the momenta can be completely randomised in the 2D plane a maximum number of times without losing the visibility of the CBS peak.

Using this procedure for several configurations of the speckle potential we found the optimal experimental parameters, which are detailed in table 2 and are used for all data presented here. It turned out that a maximum

⁶⁷A high disorder amplitude leads to a short transport time, which in turn leads to a small diffusion constant, and the CBS width decreases as $\sim 1/\sqrt{2DT_p}$. An upper limit for the disorder amplitude is given when already the switching on of the speckle induces a significant broadening of the momenta outside the 2D plane.

⁶⁸In practise the numerical aperture was regulated with a diaphragm placed in front of the diffusor.

Quantity	Value
Initial Velocity	$v_i = 3.09 \pm 0.04$ mm/s
Wavevector corresponding to v_i	$ \vec{k}_i = 4.24 \pm 0.05$ μm^{-1}
Disorder Amplitude	$V_R/h = 660 \pm 60$ Hz
Scattering Time	$\tau_S = 0.22$ ms
Transport Time	$\tau^* = 0.6$ ms
Diffusion Constant	$D = \frac{1}{2}v_i^2\tau^* = 2.86$ $\mu\text{m}^2/\text{ms}$
Speckle autocorr. function	$\sigma_{\parallel} = 1$ μm (HWHM) $\sigma_{\perp} = 0.2$ μm (RMS)

Table 2: Key parameters for the CBSR experiments.

numerical aperture is most favorable. The observation of the CBS peak was possible up to ≈ 3.5 ms, which corresponds to about $16 \tau_S$ or $6 \tau^*$.

We took a set of data for the pure CBS case as a comparison with the same parameters. The key quantity extracted is the contrast of the coherent peak: The contrast of the CBSR peak at a given propagation time T_p will be compared to the contrast of the CBS peak at equal propagation time, and ideally the two will be equal at the revival time. Figure 72 shows the CBS contrast as a function of the propagation time.

Finally, in our choice of experimental parameters we can adjust the strength of the dephasing pulse. As shown in section 8.4.3 in the perturbative regime and for diffusive propagation the minimum contrast of the coherent contribution to the momentum distribution between the dephasing pulse and the revival depends on the strength of the kick. We found this conclusion to qualitatively hold true also in our experimental situation. In order to achieve a maximum suppression of the coherent contribution we therefore chose very strong kicks, where Δk is on the order of k_i .

Method of the data analysis Right after the dephasing pulse is applied the whole momentum distribution is shifted by $\Delta\vec{k}$, and subsequently relaxes towards a steady state symmetric around zero momentum (see figure 73). This redistribution of the incoherent part of the momentum distribution is taking place on the same time scale as the evolution of the CBSR peak, a direct consequence of the limited time we are able to observe the CBS peak. This constitutes a major complication in the data analysis, since it was not obvious how to extract the CBSR peak from an evolving background. In order to make the coherent peak visible we employed a specialised data

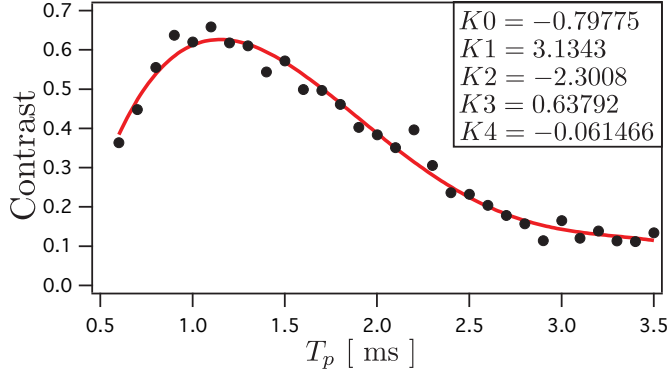


Figure 72: **CBS contrast evolution.** This CBS contrast was recorded under the same experimental conditions as the CBS revival experiments. In the following data treatment the CBSR contrast at a given propagation time is always normalised with respect to the CBS contrast at the same time. In order to exclude the noise that would be introduced in the normalisation by this measurement of the CBS contrast we use a heuristic polynomial fit, $K0 + K1 \cdot T_p + K2 \cdot T_p^2 + K3 \cdot T_p^3 + K4 \cdot T_p^4$ (red line).

treatment that aims to extrapolate the incoherent momentum distribution where the CBSR peak is expected. This treatment is explained in detail in Appendix B, and only the general idea is given here.

In broad terms, we cut out the region from $\vec{q} = \Delta\vec{k}$ to $\vec{q} = 0$ in which the evolution of the coherent contribution to the momentum distribution takes place. We recover the incoherent part of the distribution in this area by quadratically extrapolating the momentum distribution to the left and to the right into this region. Subtracting this extrapolation from the recorded data leaves only the coherent part, which is then easy to analyse. In order to get the contrast the extracted coherent distribution is divided by the extrapolated incoherent contribution. Finally, this contrast is then normalised with respect to the CBS contrast at the same propagation time.

Figure 73 shows an example of the momentum space evolution with and without dephasing pulse (CBSR and CBS configuration). In this case the dephasing pulse was applied at $t_d = 1$ ms with a strength of $\Delta k = 3.4 \mu\text{m}^{-1}$. Using the method described above the coherent part of the momentum distribution was extracted and normalised to retrieve the contrast evolution, and is displayed in a window around $\vec{q} = \vec{k}_i + \vec{k}_f = 0$, where the CBS peak is located and the CBSR peak appears around the revival time.

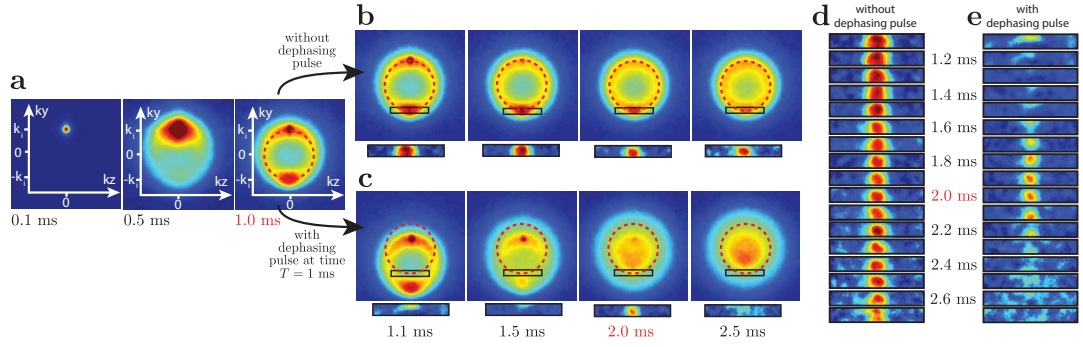


Figure 73: **Example of the evolution of the momentum space distribution in comparable CBS and CBSR configurations.** In **a** the initial evolution is shown, before at $t_d = 1$ ms the dephasing pulse ($\Delta k = 3.4 \mu\text{m}^{-1}$) is applied. The upper row (**b**) shows as a comparison the continued evolution of the pure CBS case, whereas in the lower row (**c**) the initial shift and subsequent redistribution of the momenta due to the kick are clearly visible. A circle with radius k_i centered around zero is given as reference for the on-shell momenta (red broken line). For each image the coherent contribution to the momentum distribution, normalised with respect to the CBS contrast in figure 72, is shown in a small window around $\vec{q} = 0$. The normalised coherent contribution in these windows are again given for more timesteps in **d** and **e**. The revival around $2t_d = 2$ ms in **e** is clearly visible.

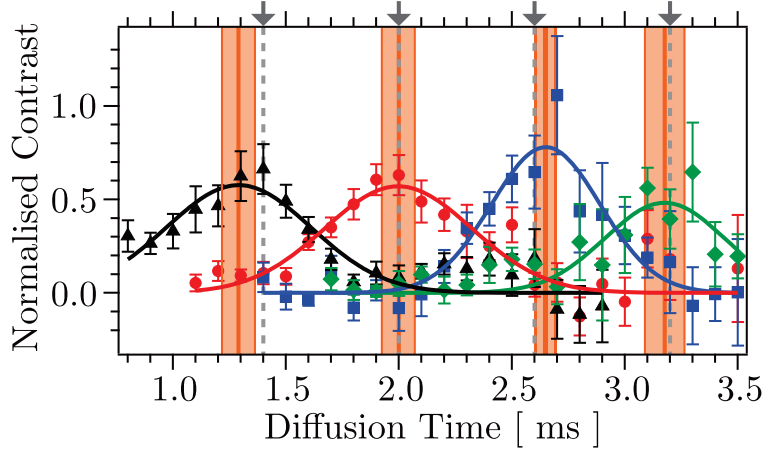


Figure 74: **CBSR contrast evolution.** Shown here are the evolution of the on-shell CBSR contrast for different times of the dephasing pulse t_d , while all other parameters are equal. The values for t_d are 0.7 ms (black), 1 ms (red), 1.3 ms (blue), and 1.6 ms (green). The expected revival times $2t_d$ are indicated by gray dashed vertical lines. To extract the time of the revival and its width the curves are fitted by gaussians with zero offset. The fitted revival time and corresponding error ($\pm 2 \times \text{RMS}$) is indicated by the vertical orange shaded bars. For a roundup of the extracted quantities see table 3.

Discussion of the Experimental Results The data presented in figure 74 are the central result of this experiment. They show the on-shell contrast evolution for different data sets, where all parameters except the time of the dephasing t_d are equal. As discussed in section 8.4 the shape of the revival in the diffusive and perturbative approximation should be an exponentially increasing / decreasing function $\sim \exp(-|T_p - 2t_d|/\tau_R)$ with $\tau_R = D\Delta k^2$. With the diffusion constant as given in table 2, and the strength of the dephasing pulse $\Delta k = 3.4 \mu\text{m}^{-1}$ in this set of experiments the predicted revival time equals to $\tau_R \approx 0.03$ ms. This is about an order of magnitude smaller than what we observe. Also the shape of the revival is not sharp enough to be described by the exponential.

Both these observations are readily explained by the fact that during the timescales that we observe the CBSR dynamics the propagation of the atoms is not diffusive, but ballistic, or at least in the cross-over regime between the two. The transport time τ^* gives the order of magnitude after which

measured quantity	t_d [ms]	value [ms]	
revival width	0.7	0.324 ± 0.040	mean value: 0.28 ± 0.04 ms
	1.0	0.325 ± 0.036	
	1.3	0.241 ± 0.023	
	1.6	0.264 ± 0.049	
revival time	0.7	1.290 ± 0.037	slope: 1.991 ± 0.029 ms
	1.0	1.997 ± 0.036	
	1.3	2.650 ± 0.023	
	1.6	3.177 ± 0.044	
peak contrast	0.7	0.574 ± 0.055	mean value: 0.60 ± 0.13
	1.0	0.570 ± 0.055	
	1.3	0.779 ± 0.063	
	1.6	0.482 ± 0.065	

Table 3: **Results of CBS revival measurements.** Extracted by gauss fits with zero offset from the data shown in figure 74. The errors given are the RMS fit errors.

the transport becomes diffusive, and here we have $\tau^* \approx 0.6$ ms. As detailed in section 8.4.1 in the ballistic regime the evolution of the CBSR peak is described by a gaussian $\sim \exp[-(T_p - 2t_d)^2/(2\tau_R^2)]$, with $\tau_R = 3/(\Delta kv_i)$. With our parameters we obtain $\tau_R = 0.28$ ms.

The width of the revival in the data set shown in figure 74 is therefore extracted using gaussian fits with zero offset. The individual values for the four different dephasing times, together with the other extracted parameters, are given in table 3. From this we calculate the average time of the width of the revival to be 0.28 ± 0.04 ms, which is in excellent agreement with our prediction in the ballistic regime.

The second quantity given by these fits is the measured time of the revival. These are shown in figure 75, together with a linear fit. The slope of the fit, measured to be 1.991 ± 0.029 , is very close to the predicted value of 2.

We can also compare the maximum contrast of the revival with the CBS contrast at the same time. The predicted behavior is that both are equal, but we find it to be consistently smaller. This might be due to the fact that we are far from the perturbative regime: The strength of the kick, and the resulting modification of the scattering paths could possibly lead to a reduction of the contrast. That being said, the clear existence of the revival

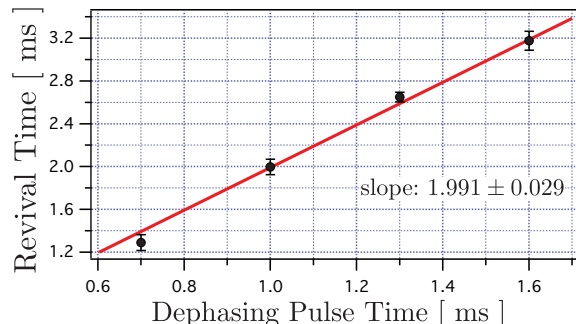


Figure 75: **Revival time as a function of the dephasing pulse time.** The fitted revival time of the data shown in figure 74 as a function of the dephasing pulse time t_d is given. The error bars indicate the fit error ($\pm 2 \times$ RMS). The red line is a linear fit without offset, giving a slope of 1.991 ± 0.029 , in perfect agreement with the predicted value of 2.

with an average peak contrast of 0.6 nevertheless shows that our method of time-reversal breaking preserves coherence at least to a large degree.

In another set of experiments all experimental parameters were left constant except for the strength of the dephasing pulse Δk . The widths of the revival τ_R were again extracted using gaussian fits, and a decrease of the revival width is expected for an increase in the dephasing pulse strength, as $\tau_R = 3/(\Delta k v_i)$ with v_i the initial velocity of the atoms. Figure 76 shows the results of this set of data. The experimental parameters are again the ones given in table 2, and the time of the dephasing pulse is $t_d = 1.3$ ms. We observe a relatively good agreement between the expected behavior and the experimental results. Note in particular that the aforementioned decrease of the revival width with increasing pulse strength is clearly visible, and that the theoretical curve does not contain any free parameters. The deviation from the prediction at the lowest dephasing pulse may be due to the fact that here the width of the revival is highest. Within the duration of the revival the ballistic propagation then transitions to diffusive propagation, for which the width is much more narrow.

8.6 Numerical simulations and investigations of arbitrary pulse shapes

In order to verify our understanding of the dynamics of the system, 2D numerical simulations of the Schrödinger equation were carried out. In par-

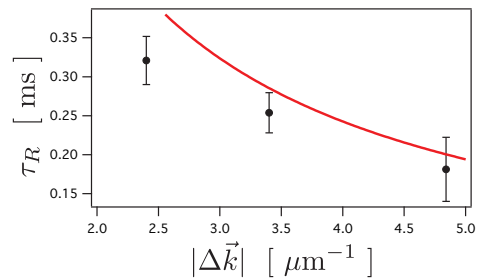


Figure 76: **Width of the revival as a function of the dephasing pulse strength.** In this data set all experimental parameters are constant except for the strength of the dephasing pulse Δk . The width of the revival τ_R is extracted using gaussian fits, and the error bars signify the uncertainty of the fit. The red line shows the theoretical prediction in the ballistic regime, $\tau_R = 3/(\Delta k v_i)$.

ticular we aimed to recreate the conditions in the calculations by T. Micklitz *et al.* in [80], which we could not achieve experimentally. These conditions are that the propagation is diffusive, and that the disturbance by the dephasing pulse is small. The results of these simulations are given in section 8.6.1.

We also investigated the effect of an arbitrary pulse shape on the CBS revival, which will be treated in section 8.6.2. This was done to verify that the finite length of our pulse does not have a negative impact on the maximum contrast of the CBS revival. It was also prompted by measurements of the magnetic field of the dephasing pulse, which was found to be not perfectly symmetric.

8.6.1 2D numerical simulation of the Schrödinger equation

Parallel to our first experimental investigations numerical simulations of the Schrödinger equation were carried out. The code was developed by Thomas Plisson, a former PhD student in our group, and a detailed description of it can be found in his thesis [92]. It uses the Crank-Nicolson algorithm, a finite difference method, to calculate the evolution of a wave packet in a 2D box. To avoid reflections of the wave function from the boundaries of the box absorbing boundary conditions are imposed.⁶⁹

⁶⁹These absorbing boundary conditions were implemented for the study Anderson localization in 2D, which necessitates long propagation times. Here, the wave function in

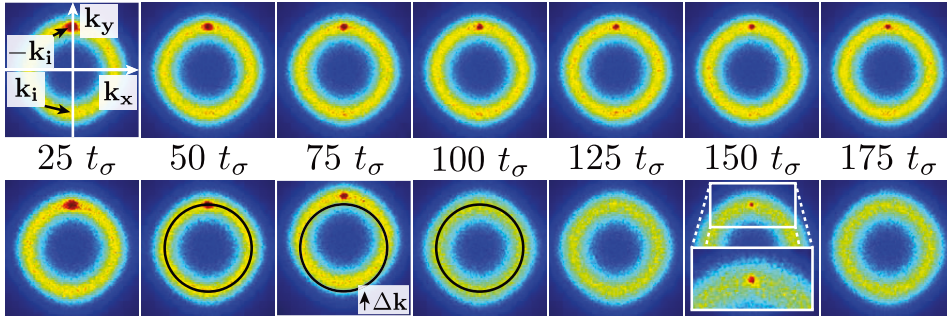


Figure 77: **2D Numerical Simulation of CBS and CBSR Dynamics.** Shown here is the momentum space evolution of a CBS and CBSR configuration (upper and lower row respectively). The parameters in this simulation are equal in both cases, and were chosen to highlight an “ideal” configuration, where the contrast of the CBS peak stays equal to 1, and the propagation times are much longer than the transport time (diffusive propagation). Up until $75 t_\sigma$ there is no difference between the CBS and the CBSR evolution. At $t_d = 75 t_\sigma$ a momentum kick $\Delta \vec{k}$ is given in the CBSR case, which shifts the distribution. The black circles with a radius of k_i around the origin at $50 t_\sigma$, $75 t_\sigma$, and $100 t_\sigma$ highlight this shift and the subsequent redistribution of the momenta. The coherent peak is suppressed except around the revival time $T_p = 2t_d = 150 t_\sigma$.

As in our experiments the initial wave function in momentum space is a gaussian centered around an initial momentum $\hbar\vec{k}_i$. A speckle potential is switched on abruptly, and the evolution of the momentum space density is recorded. We previously used this configuration to verify the scattering and the transport times, and the dynamics of the CBS peak [55]. The only change that was implemented to study the CBS revival dynamics was a dephasing at a specific time. To accomplish this the wave function was multiplied by the factor $\exp(i\Delta kx)$ at one point during the propagation, mirroring the effect of the dephasing due to a gradient field. The evolution is calculated for several realisations of the speckle potential, and then averaged. The code uses the natural units given by the size of the speckle autocorrelation function, as detailed in section 4.3. The results of the numerical simulations presented here will therefore be given in dimensionless quantities, renormalised to these natural units: wavenumber $\kappa = k/k_\sigma$, energy $\epsilon = E/E_\sigma$, and time $\tau = t/t_\sigma$.

In order to be in a configuration that recreates the behaviour predicted by Micklitz *et al.* we first had to choose a configuration where the diffusive approximation holds, that is where the observation of the CBS peak is possible for times much longer than transport time. Practically this can easily be achieved by having a very narrow initial momentum distribution.⁷⁰ Figure 77 shows the results of this simulation compared to the case of a pure CBS configuration. The parameters chosen were $V_R = E_\sigma/2$, $k_i = k_\sigma$, and $\Delta k = 0.2k_\sigma$, which leads to a mean scattering time of $\tau_S = 2.1 t_\sigma$. The diffusion constant was determined directly by monitoring the increase of the size of the real space distribution $\sim \sqrt{2DT_p}$, giving $D = 3.1 k_\sigma^{-2}t_\sigma^{-1}$. From this one can derive the transport time (see section 2.4) $\tau^* = 2D/v_i^2 \approx 6.2 t_\sigma$. The dephasing pulse was administered at $T_p = 75 t_\sigma$, leading to a revival of the CBS peak around $T_p = 150 t_\sigma$. Since the dephasing is applied after more than $10 \tau^*$ the propagation can safely assumed to be diffusive.

According to equation 82 the shape of the revival is a double exponential, with a characteristic time of $\tau_R = (D\Delta k^2)^{-1}$. By monitoring the contrast at $\vec{q} = 0$ (“on-shell”) we tested this prediction in our simulations with the parameters described above, as well as another data-set with a weaker de-

real space could propagate to the edges of the box and reflections from its boundaries could distort the results. They are of less importance in the simulations with relatively short diffusion times presented here.

⁷⁰The other experimentally limiting factor, the eventual 3D redistribution of the momenta, is not present in the 2D simulations. See section 7.4.2 for a discussion of these effects on the maximum observation time of the CBS peak.

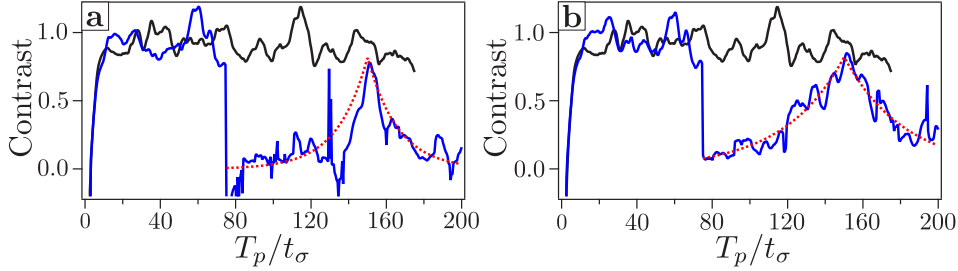


Figure 78: **Simulation of the CBSR on-shell contrast evolution.** The evolution of the contrast at $\vec{q} = 0$ (“on-shell”) is shown in two CBSR configurations with $\Delta k = 0.2 k_\sigma$ (panel **a**) and $\Delta k = 0.1 k_\sigma$ (panel **b**). Both are drawn in blue. The coherent peak is completely suppressed at $t_d = 75 t_\sigma$ (i.e. at the time of the kick), and reappears at $2t_d = 150 t_\sigma$. As comparison in each case the contrast of a pure CBS evolution is shown in black. The dotted red lines show the theoretical prediction of the shape of the revival, where only the amplitude was manually adjusted (see text).

phasing pulse $\Delta k = 0.1 k_\sigma$.⁷¹ The results are shown in figure 78, compared to the contrast of the pure CBS case. The noise in the data is a combined effect from the limited amount of averaging over different disorder configurations during the simulation, and uncertainties in the extraction of the contrast.⁷² In the stronger kick case in panel the noise is higher compared to the case of weaker kick. This may be explained by the fact that the momenta get redistributed over an interval from $k_i - \Delta k$ to $k_i + \Delta k$. For a weaker kick this interval is smaller, which increases the signal to noise ratio. The CBS contrast stays nearly constant over the whole duration of the simulated evolution, whereas the contrast falls to zero right after the dephasing pulse and only reappears around the revival time. Additionally the predicted behavior of the revival is shown, where all parameters except the amplitude are fixed. The latter was adjusted manually to accommodate for the slight decrease in the CBS contrast. The characteristic time of the re-

⁷¹The method used to extract the on-shell contrast is the same as for our experiments on CBS, that is we performed a radial integration over a thin ring with radius k_i to obtain an angular profile. The more involved method for the extraction of the contrast used in our experiments on the CBS revival was not necessary, since here the revival appears long after the redistribution of the momenta after the kick is complete.

⁷²All data presented here was averaged over 50 disorder configurations. It takes approximately one day to complete one data set on a fairly fast computer.

vival is $\tau_R \approx 16 t_\sigma$ for the stronger, and $\tau_R \approx 64 t_\sigma$ for the weaker dephasing pulse.

8.6.2 Arbitrary shape of the dephasing pulse

Experimentally it is impossible to create a true delta-like pulse of the dephasing potential. First, the pulse itself always has a finite length. On top of that we found that there is a perturbation of the levitation after the pulse such that for some time the overall magnetic potential is different compared to before the pulse.

In order to try to account for this experimental reality we analysed a theoretical description provided to us by T. Micklitz that is based on an arbitrary pulse shape. This description is, again, valid in the perturbative regime of weak kicks, and in the diffusive limit of propagation. Since on the relevant time scales our experiment is situated in the ballistic regime, or in the transitional regime between ballistic and diffusive propagation, it cannot be directly compared to our results. Nevertheless we studied it to at least get qualitative figures of how the evolution of the coherent peak is modified by a non delta-like dephasing pulse.

The contrast as a function of the momentum \vec{q} and the total propagation time T_p in the case of an arbitrary pulse is given by:⁷³

$$\begin{aligned}
 C(\vec{q}, T_p) &= \exp \left[-D \left(T_p \vec{q}^2 + 2\chi_0(T_p) \vec{q} \cdot \Delta \vec{k} + \chi_1(T_p) \Delta \vec{k}^2 \right) \right] \\
 \chi_0(T_p) &= \int_0^{T_p} ds (T_p - 2s) p(s) \\
 \chi_1(T_p) &= \int_0^{T_p} ds_1 \int_0^{T_p} ds_2 (|T_p - s_1 - s_2| - |s_1 - s_2|) p(s_1) p(s_2)
 \end{aligned} \tag{90}$$

Here, $p(t)$ is the normalised shape of the dephasing pulse: $\int p(t) dt = 1$. For a delta-like pulse $p(t) = \delta(t - t_d)$ this set of equations reduces to formula (79).

First one can investigate what happens for a pulse shape $p(t)$ that has a finite width but is evenly symmetric around its center t_d , that is for a pulse that observes $p(t - t_d) = p(t_d - t)$. In particular, it is tempting to assume that such a symmetric pulse would still lead to a revival at the position $\vec{q} = 0$ and at the time $T_p = 2t_d$ with a contrast of one, since both the direct and the reciprocal paths would acquire the same phase due to the dephasing potential. To verify this we set $\vec{q} = 0$ and $T_p = 2t_d$ in equation (90), and expand the pulse shape $p(t)$ in a Taylor series, $p(t) = \sum_n \alpha_n (t - t_d)^{2n}$, where

⁷³Private communications with T. Micklitz, C. Müller, and A. Altland.

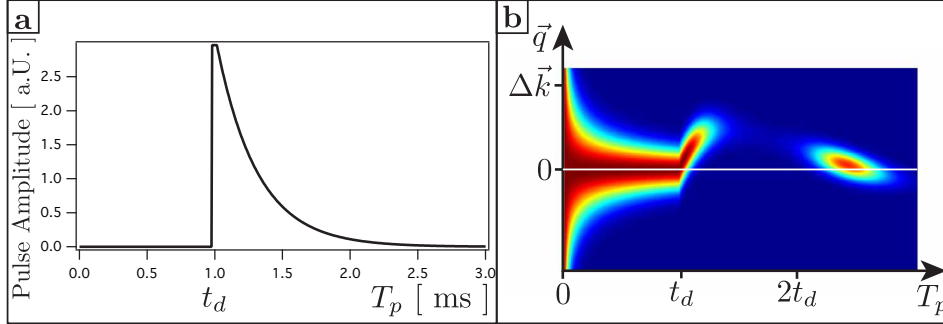


Figure 79: **Dynamics with an asymmetric pulse.** Using equation (90) the effect on the CBSR dynamics were explored for an asymmetric pulse. The pulse shape used here is shown in panel **a**. It starts at 1 ms and decreases exponentially with a time-constant of 0.2 ms. All relevant parameters are equal to the ones used to compute the behavior with a delta-like pulse, shown in figure 68: The strength of the dephasing pulse $\Delta\vec{k} = 2.5 \mu\text{m}^{-1}$, and the diffusion constant $D = 2.88 \mu\text{m}^2/\text{ms}$. The contrast as a function of the position \vec{q} and the propagation time T_p is shown in panel **b**. One observes that the position of the highest contrast of the revival is no longer at $\vec{q} = 0$, and also not at $T_p = 2t_d$. The highest contrast is also reduced to ≈ 0.84 .

$n = 0, 1, 2, \dots$. With this power series that is by definition symmetric around t_d one can then show that $\chi_1(T_p = 2t_d) = 0$, and therefore

$$\begin{aligned} C(\vec{q} = 0, T_p = 2t_d) &= \exp \left[-D\chi_1(2t_d)\Delta\vec{k}^2 \right] \\ &= 1. \end{aligned} \quad (91)$$

Using the Taylor expansion one can also show that any asymmetric term of the Taylor expansion of the pulse shape leads to $\chi_1(2t_d) \neq 0$, and therefore to a contrast $C(\vec{q} = 0, T_p = 2t_d) \neq 1$. Although not a stringent proof, this is at least an indication that in order to achieve a contrast of one at the revival time the pulse shape should be symmetric.

To show the effects of an asymmetric pulse shape, formula (90) was solved numerically for a short pulse with an exponentially decreasing tail, shown in figure 79. The parameters for this simulation are the same as the ones used to compute the contrast in figure 68: The time of the dephasing pulse is $t_d = 1$ ms, its strength (integrated over its whole duration, including the

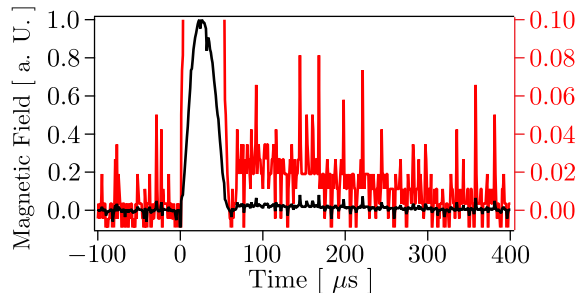


Figure 80: **Magnetic field of a dephasing pulse close to the atoms.** The magnetic field of a dephasing pulse with a programmed length of $29 \mu\text{s}$ was recorded about 2 cm from the atoms with a Hall probe. The black and red lines show the same data, with the red line magnified by a factor 10. In the magnified plot a perturbation lasting several hundred μs is visible. According to numerical simulations this tail does not affect the dynamics of the CBS revival (see text).

exponential decrease) is $\Delta\vec{k} = 2.5 \mu\text{m}^{-1}$, and the diffusion constant is $D = 2.88 \mu\text{m}^2/\text{ms}$. The pulse decreases as $\exp(-T_p/\tau)$ with $\tau = 0.2 \text{ ms}$. There are four notable changes with respect to the ideal case shown in figure 68. The time the highest contrast appears is at $T_p \approx 2.4 \text{ ms}$, it is situated at $\vec{q} \approx 0.13 \mu\text{m}^{-1}$, and its maximum contrast is $C_{max} \approx 0.84$. Finally the displacement of the CBS peak naturally does not happen instantaneously at $t_d = 1 \text{ ms}$ for this very long pulse.

This is an example of a very asymmetric pulse shape, and serves just to illustrate qualitatively the effects. We wanted to quantify whether the aforementioned asymmetry in our experimental setting has an appreciable influence on the position and the maximum contrast of the revival. In order to do this we recorded the magnetic field with a hall probe just above the glass cell, with a distance $\approx 1\text{-}2 \text{ cm}$ from the atoms. An example of such a curve is shown in figure 80. Solving again numerically equation (90) with the recorded pulse shapes used in our experimental studies we found no appreciable deviation from the ideal behavior.

8.7 Conclusion

In conclusion, we have studied the underlying symmetry of wave propagation in disordered media that leads to Coherent Backscattering and Weak Local-

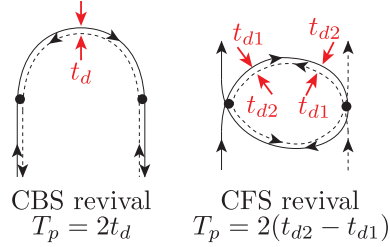


Figure 81: **Extension to higher order corrections.** With a sequence of several timed pulses of the same strength higher order corrections to coherent transport can be probed. On the left hand side a schematic drawing of the CBS real space trajectories is given. A pulse at t_d leads to a revival after the propagation time $T_p = 2t_d$. On the right hand side the diagram leading to the coherent forward scattering peak (CFS) is shown. This contribution is revealed by a sequence of two pulses at t_{d1} and t_{d2} with a revival at $T_p = 2(t_{d2} - t_{d1})$.

ization. The basis of these fundamental corrections to coherent transport of waves is the constructive interference of counter-propagating paths due to the time-reversal symmetry of the propagation. Owing to the precise spatial and temporal control over the potential landscape that is available for cold atom systems a dephasing between the pairs could be introduced, leading to the suppression of interference, and therefore the suppression of the CBS peak. Since the dephasing is applied during a short time and does not destroy coherence we observe a short revival of the CBS peak. In this sense our experiments perform a loop spectroscopy, isolating specific diagrams in the multiple scattering process.

We observed the revival of the CBS peak after a propagation time $T_p = 2t_d$ when the dephasing pulse was administered at time t_d . In their publication T. Micklitz *et al.* propose that higher order corrections can be probed by applying multiple pulses at times t_{d1}, t_{d2}, \dots [80]. For example, a revival of the Coherent Forward Scattering peak [59, 79, 69, 46] is expected at time $T_p = 2(t_{d2} - t_{d1})$ (see figure 81). Such a study would provide insight into the processes that eventually lead to Anderson localization.

We did not experimentally try techniques other than the application of a magnetic gradient to achieve the dephasing. But numerical simulations suggest that a revival of the CBS peak could also be observed by a short modulation of the disorder amplitude.

9 Conclusion and outlook

The present manuscript contains our work on coherent transport phenomena in disordered potentials. Since several decades this field has been intensely investigated, both theoretically and experimentally. Early experiments used electronic systems, which were later joined by optical, acoustical, and other waves. A relatively recent addition, the study of the propagation of ultracold atoms in optical speckles, was pioneered in our group and led to the observation of 1D Anderson localization [20]. Amongst others, this system offers the advantage of having precise control over the disordered potential, and to be able to directly image the evolution of the density distribution either in real, or in momentum space.

During the course of this thesis several major upgrades in the experimental setup were carried out. These include, but are not limited to, an improvement of the imaging system, and the complete overhaul of the speckle system. The sum of these changes make the experiment more flexible, and run better than ever.

In the first experiment described in this manuscript we were able to observe 3D Anderson localization by monitoring the evolution of the real space density of the atoms in a strong disorder. A maximum localized fraction of about 20% was observed, which puts the localization beyond any reasonable doubt, but a limitation in our experimental scheme is the lack of control over the energy distribution in the disorder. This experiment is among the first two to observe 3D Anderson localization with ultracold atoms, and paves the way to a study of the critical regime around the mobility edge.

In our second experiment we exploited the possibility to record the evolution of the momentum distribution to perform the first observation of Coherent Backscattering with ultracold atoms. Preparing the atoms with a well defined initial velocity we are able to observe the full evolution of the momentum space distribution. The contrast and width of the CBS peak were measured and shown to be in good agreement with theory.

Next to the observation of CBS this experiment allows us to directly measure two fundamental transport parameters, the mean scattering time and the transport time. An experimental study of these transport parameters for different momenta and disorder strengths was carried out during this thesis, but their analysis and interpretation is still under way. The parameters ranged from weak to strong disorder, which provides a good opportunity for a comparison with theory.

In the third experiment we were using the precise spatial and temporal

control over the atoms to observe a novel effect, predicted by T. Micklitz *et al.*, the revival of the Coherent Backscattering Peak [80]. Through a deliberate breaking of the time-reversal symmetry of the wave propagation the CBS peak is suppressed, except for a brief moment when the symmetry is re-established and the CBS peak reappears. This TRS breaking is accomplished by the application of a shortly pulsed magnetic gradient field.

Efforts are currently underway to upgrade our experiment with an optical speckle whose frequency can be tuned around the resonance of the atoms. This would allow us to create a state-dependent disorder and precisely control the energy of the atoms. For instance, the laser wavelength could be tuned to a so called “magic wavelength”, where the dipolar interaction is cancelled for one state and not for the other. With a precisely controlled energy in the disorder a study of the critical regime around the mobility edge in a 3D Anderson localization experiment would be possible.

An exciting extension of the CBS experiments would certainly be the observation of the CFS peak. This novel effect, first predicted in 2012 by T. Karpiuk *et al.* [59], is believed to be a direct signature of Anderson localization. It already has initiated several theoretical works, but has not yet been seen in experiments.

Finally, the scheme to use a short dephasing pulse to single out the quantum corrections responsible for the CBS peak can be expanded to higher order corrections. It would therefore be possible, albeit experimentally very challenging, to repeat this experiment in the Anderson localized regime and observe a revival of the aforementioned CFS peak.

A Ensemble view of the experiment

Figure 82 shows a photograph of the entire experimental apparatus. In figure 83 the same view is given schematically, pointing out the position of different components of the experiment. They are to be compared with figure 11, which shows only the various components of the vacuum system (the viewpoint is on the backside of the experiment when compared to the images given here). Note that at the time the picture was taken the new speckle setup was still under construction.

The entire room is temperature controlled to 21.5° C. A deviation by only some degrees leads to misalignments, most notably of the various trap and cooling laser beams, which render the operation of the experiment impossible.

The experiment rests on vibration damping supports, which in turn are positioned on a vibration damped part of the floor.

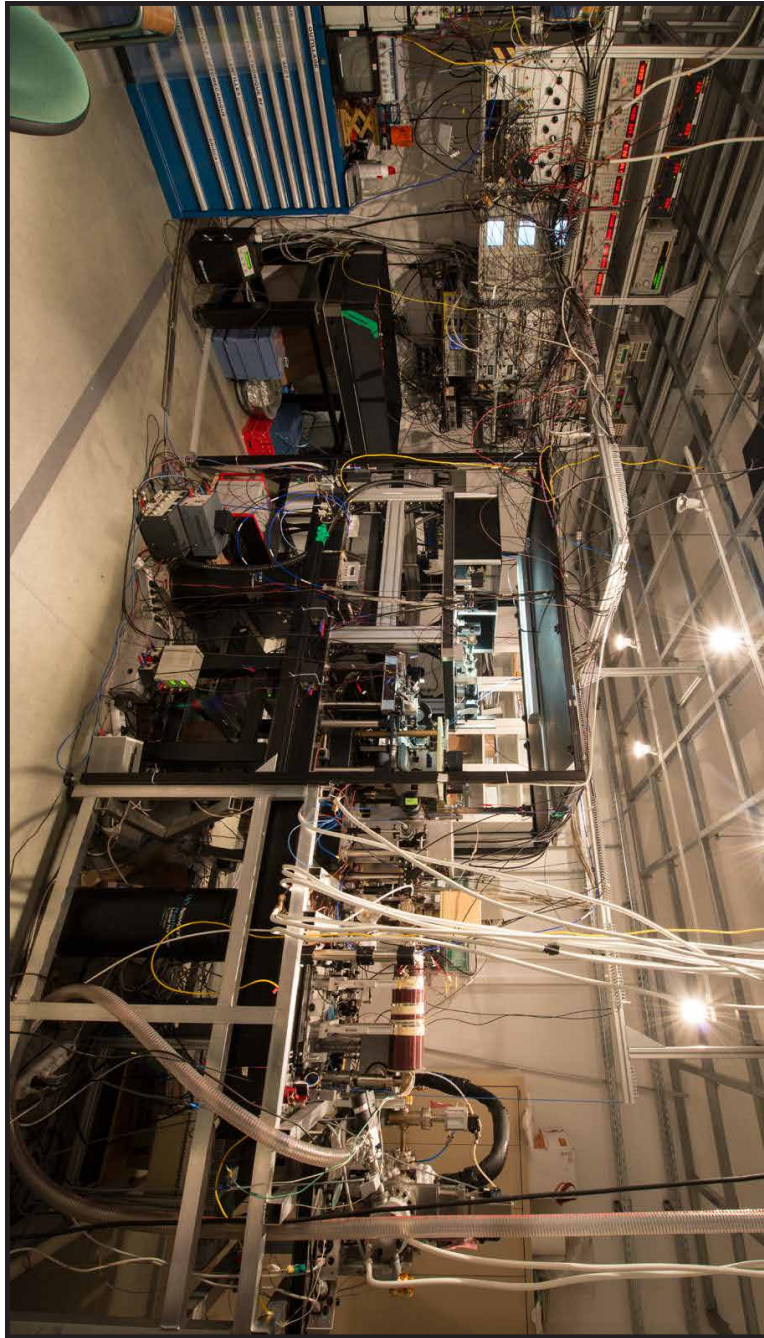


Figure 82: View of the entire experiment.

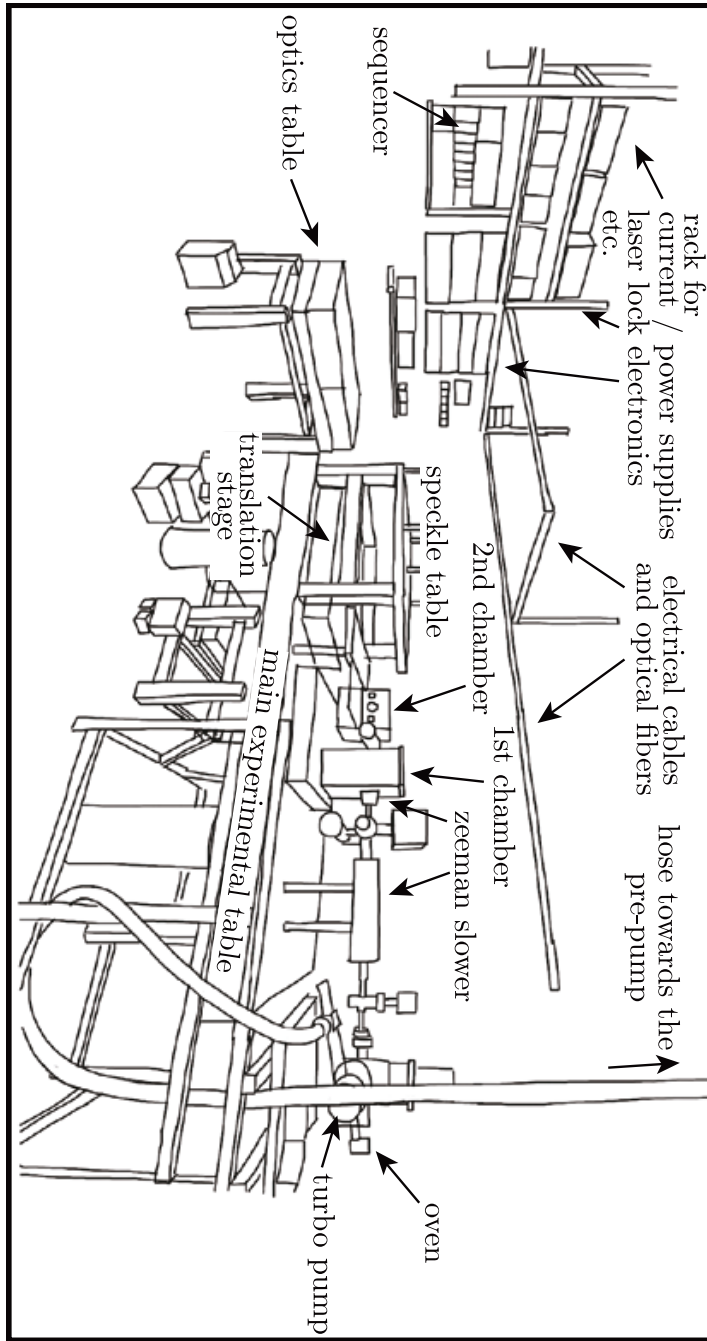


Figure 83: View of the entire experiment - schematic.

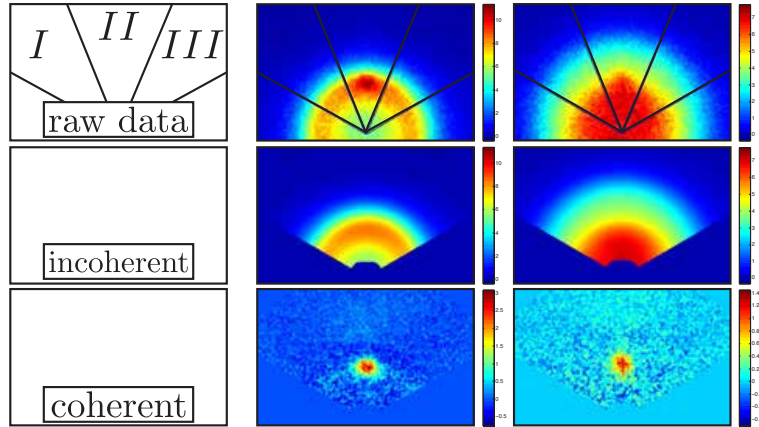


Figure 84: **Extraction of the coherent part of the momentum distribution.** The top row shows the raw data of CBS and CBSR momentum distribution (center and right column respectively). The image is cut into three regions: Region I and III are used to extrapolate the incoherent momentum distribution into region II, where the coherent peak is located. The second row shows the result of this extrapolation. The third row shows the coherent part of the momentum distribution, obtained by subtracting the incoherent part (second row) from the raw data (first row).

B CBSR data treatment

The CBSR data treatment posed considerable difficulties, which mainly stem from the fact that the signal we are looking for is sitting on an evolving background: The incoherent part of the momentum distribution is still in the process of evolving towards its symmetric equilibrium state after its perturbation due to the dephasing pulse while the CBSR peak appears. This is a direct consequence of the fact that in our experiment it is possible to observe the CBS peak for a limited amount of time, on the order of several τ^* , where τ^* is the transport time. The transport time gives the time scale it takes for the momenta to redistribute.

In order to extract the coherent part of the momentum distribution we developed a method that extrapolates the incoherent momentum distribution into the region where the CBS or the CBSR peak is located. The code used can be found at the end of this section.

Figure 84 shows the general idea of the treatment for the CBS and the

CBSR configuration. The experimental parameters are the ones described in table 2, the diffusion time is 2 ms, and the time of the dephasing pulse is 1 ms. The raw data is separated into three regions I, II, and III. Regions I and III do not contain any coherent contribution to the momentum distribution, which is located entirely in region II. The incoherent part of the momentum distribution in region II is extrapolated using the fit routine given at the end of this chapter. The coherent part is then obtained by subtracting this extrapolated incoherent contribution from the raw data.

In parallel to this method for the extraction of the coherent part of the momentum distribution Vincent Denechaud, a master student in our group, explored a different approach: We are able to measure the momentum distribution right after the dephasing pulse, at $T_p = t_d^+$. As was pointed out earlier, this distribution is equal to the CBS distribution at T_p shifted by $\Delta\vec{k}$. The atoms therefore populate momenta roughly in the range of $[|\vec{k}_i| - |\Delta\vec{k}|, |\vec{k}_i| + |\Delta\vec{k}|]$. In a separate set of experiments we measured the scattering times τ_s and the transport times τ^* in this momentum range. With the knowledge of these quantities and the initial state just after the pulse it is in principle possible to predict the momentum space evolution [93]. The thus predicted evolution of the momentum space density does not take into account interference effects and therefore only represents the incoherent part. Subtracting this computed distribution from the recorded data then should leave only the coherent contribution.

At the moment of writing this thesis first positive results were achieved using this method. Its main inconvenience is though that it does not take into account the inevitable 3D isotropisation of the momenta which is taking place for longer diffusion times. This introduces a systematic difference between the predicted and the recorded distribution. Since the signal we are seeking to extract is small, on the order of 10%, even a small error of the same magnitude then falsifies the results.

```

1 function [IncohImg] = RadialQuadraticFit(img,mask1,mask2,
      centerRingCol,centerRingRow)
2
3 % Definition of the fit function:
4 radquadfun=@(a,b,c,x0,y0,x,y) ...
5     a+b*((x-x0).^2+(y-y0).^2)+c*sqrt((x-x0).^2+(y-y0).^2);
6
7 % Only a part of the image is used for the fit - select it with
      mask1 and mask2:
8 imgcut=img.*mask1.*mask2;
9
10 CountMat=zeros(1000,1000); % Counter
11 IncohImg=zeros(1000,1000); % This matrix will hold the
      extrapolated incoherent momentum distribution.
12 width=20;
13 [colMatrix,rowMatrix]=meshgrid(1:1000,1:1000);
14 radiusmat=sqrt((colMatrix-centerRingCol).^2+(rowMatrix-
      centerRingRow).^2);
15
16 for k=1:10:round(centerRingCol-2*width);
17     disp(['start fit region' num2str(k) ' ...'])
18     % These are additional pixels that are excluded from the fit
19     :
20     vec1=find(abs(radiusmat-(centerRingCol-k))>round(width/2));
21     % And these include the region where the fit is valid:
22     vec2=find(abs(radiusmat-(centerRingCol-k))<round(width/2));
23     ROIimg=imgcut;
24     ROIimg(vec1)=0;
25     % Perform the fit:
26     sf=fit([colMatrix(:),rowMatrix(:)],ROIimg(:),radquadfun, ...
27         'Exclude',ROIimg(:)==0,'StartPoint',[0,0,0,500,500])
28     IncohImg(vec2)=IncohImg(vec2)+sf(colMatrix(vec2),rowMatrix(
29         vec2));
30     CountMat(vec2)=CountMat(vec2)+1;
31     disp(' ... done')
32 end
33 IncohImg=IncohImg./CountMat;

```

Code 1: Analysis code used to extrapolate the incoherent momentum distribution into the region of the Coherent Backscattering Revival peak.

C Properties of Rubidium 87

Rubidium 87 is an element of the alkali metal group. With its single valence electron and its otherwise filled orbitals its electronic level structure resembles that of hydrogen. The electron spin $S = 1/2$ can combine with the nuclear spin of $I = 3/2$ to a total angular momentum $F = 1$ and $F = 2$ in the $5^2S_{1/2}$ ground state. The degeneracy between these states is lifted by the hyperfine splitting of $\Delta E_{\text{hfs}}/h \approx 6.8$ GHz. Transitions to the $5^2P_{1/2}$ and $5^2P_{3/2}$ excited states are respectively called the *D1* and *D2* lines, with transition wavelengths of 795 nm and 780 nm. The *D2* line transition $F = 2 \leftrightarrow F' = 3$ forms a cycling transition that is used for imaging (see section 3.1) and cooling via the radiation force (see section 3.2.2). The light necessary to drive this transition can conveniently be obtained by inexpensive diode lasers. The *D2* hyperfine level structure of ^{87}Rb is shown in figure 86.

The scattering length $a = 5.3$ nm describes the effective size of the atoms for s-wave scattering, which is important for cooling via evaporation.

These properties make ^{87}Rb favorable for cold atom experiments, and indeed one of the first realisations of Bose-Einstein condensation used this atomic species [10].⁷⁴ The following table summarises some of the physical properties of ^{87}Rb , which are collected from [109]. The same reference also contains more detailed information about the electronic level structure.

Quantity	Symbol	Value
Mass	m_{Rb}	1.44×10^{-25} kg
Nuclear Spin	I	3/2
Melting Point	T_M	39.30 °C
D2 Transition Wavelength (Vacuum)	λ	780.241 nm
D2 Transition Wavelength (Air)	λ_{air}	780.033 nm
$5^2P_{3/2}$ Lifetime	τ	26.23 ns
$5^2P_{3/2}$ Decay Rate Natural Line Width (FWHM)	Γ	$2\pi \times 6.07$ MHz
D1 Transition Wavelength (Vacuum)	λ	794.979 nm
D1 Transition Wavelength (Air)	λ_{air}	794.767 nm
$5^2P_{1/2}$ Lifetime	τ	27.68 ns
$5^2P_{1/2}$ Decay Rate Natural Line Width (FWHM)	Γ	$2\pi \times 5.75$ MHz

⁷⁴Two other experiments published the observation of a BEC in the same year using other elements in the alkali metal group, sodium [35] and Lithium 7 [21].

D Optical setup for laser cooling, trapping, and imaging

As described in sections 3.1 and 3.2.2 we use laser beams resonant with hyperfine transitions of the D2 line of ^{87}Rb to cool, trap, and image the atoms. In total we have three lasers, L1 (“probe”), L2 (“repumper”), and L3 (“trap”) at our disposal. They are mounted on a dedicated optics table, separated from the rest of the experiment, in order to avoid vibrations.⁷⁵ These lasers are extended cavity lasers, originally designed at the Observatoire de Paris (SYRTE), with a wavelength of about 780 nm and a spectral width of about 30 kHz, each producing an output power of 20 – 30 mW. Their frequency can be adjusted over a maximum range of 1.5 GHz (the free spectral range of the laser) by changing the cavity length with a piezo. A description of their design can be found in [5, 19].

Figure 85 shows a schematic overview of the optics table, and figure 86 shows the frequencies of the lasers together with the $D2$ hyperfine level structure. Both images represent the state of the optics table at the writing of this manuscript. Some minor changes were effectuated during the course of this thesis, namely the addition of the transverse molasses and the optical pumping, and modifications of some frequencies in figure 86. For a description of the previous setup see [19].

The probe beam is frequency locked on the $F' = 2 \times 3$ cross over of the $5^2\text{P}_{3/2}$ manifold using saturated absorption. Increasing its frequency by 2×66 MHz using an AOM double pass it is resonant with the $F = 2 \rightarrow F' = 3$ transition. It is then fed into an optical fiber (“absorption fiber” in figure 85) and used for absorption imaging in the first chamber.

L2 and L3 are frequency locked with the fixed frequency of L1 using the beat signal recorded by fast photodiodes (“PD”).

In order to bridge the 6.8 GHz gap between the $F = 1$ and $F = 2$ hyperfine levels the beat signal between L1 (offset by an AOM by 200 MHz) and L2 is mixed with an RF frequency of a dielectric resonant oscillator (“DRO”) at 6.587 GHz. The command value of the servo loop controlling the frequency of L2 is -203 MHz. A final AOM shifts the frequency by 117 MHz such that L2 is resonant with the $F = 1 \rightarrow F' = 2$ transition.

L3 is resonant with the $F = 2 \rightarrow F' = 3$ cycling transition. Its frequency chain is similar to the one of L2, but does not necessitate a mixing of frequencies with the DRO.

⁷⁵The mechanical shutter and the translation stage induce vibrations to the table on which the experiment is mounted.

For both L2 and L3 the command value, which is shown at its standard value of 203 MHz and 200 MHz respectively, can be changed during the experimental cycle between 0 and 512 MHz. This is the case for the molasses and depumping phase.

Except for the optical pumping, L2 and L3 are always used in combination. They are therefore combined before sending them towards the experiment via the fluo fiber (for fluorescence imaging), the trap fiber (for the MOT), the transv. molasses fiber, and the zeeman slower beam. Since the optical power coming directly from L2 and L3 is not sufficient for the needs of our experiments it is amplified using two tapered amplifiers (“MOPA 1” and “MOPA 2”).

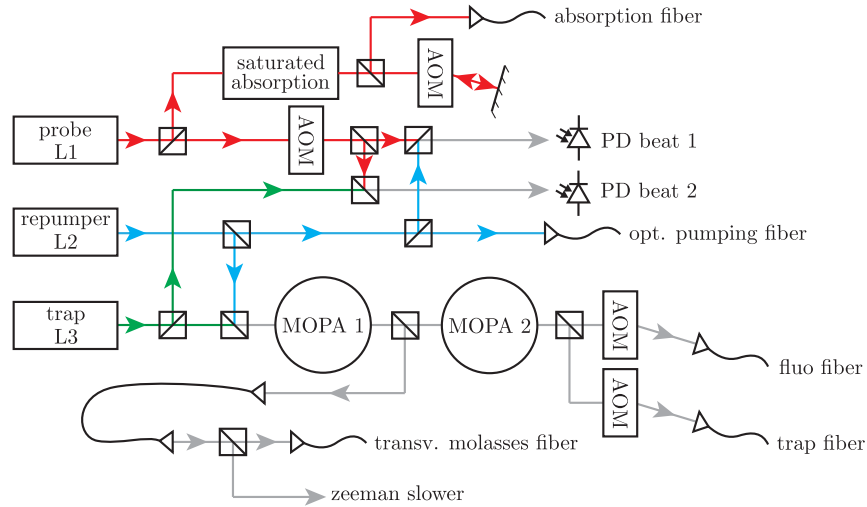


Figure 85: **Schematic view of the optic table.**

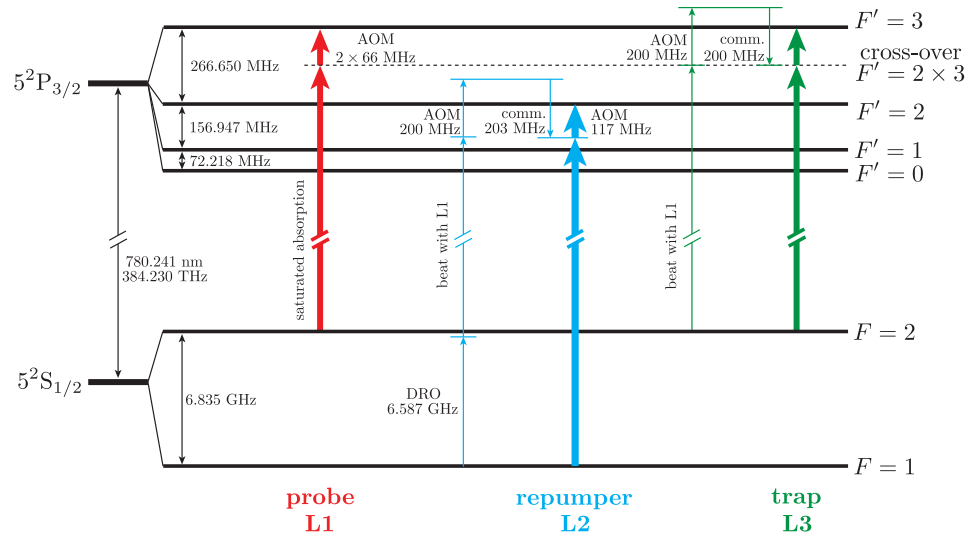


Figure 86: **Frequency chain of the lasers on the optics table.** The relative hyperfine shifts and frequencies are shown to scale in the $5^2S_{1/2}$ and $5^2P_{3/2}$ manifolds. Note though that the scale for each manifold is different.

References

- [1] E. Abrahams, P.W. Anderson, D.C. Licciardello, and T.V. Ramakrishnan. Scaling Theory of Localization: Absence of Quantum Diffusion in Two Dimensions. *Physical Review Letters*, 42(10):673–676, 1979.
- [2] Yakir Aharonov and David Bohm. Significance of electromagnetic potentials in the quantum theory. *Physical Review*, 115(3):485, 1959.
- [3] E. Akkermans and G. Montambaux. *Mesoscopic Physics of Electrons and Photons*. Cambridge University Press, 2011.
- [4] Eric Akkermans, P.E. Wolf, and R Maynard. Coherent Backscattering of Light by Disordered Media: Analysis of the Peak Line Shape. *Physical review letters*, 56(14):1471–1474, 1986.
- [5] F Allard, I Maksimovic, M Abgrall, and Ph Laurent. Automatic system to control the operation of an extended cavity diode laser. *Review of scientific instruments*, 75(1):54–58, 2004.
- [6] Wolfgang Alt, Dominik Schrader, Stefan Kuhr, Martin Müller, Victor Gomer, and Dieter Meschede. Single atoms in a standing-wave dipole trap. *Physical Review A*, 67(3):033403, 2003.
- [7] B. L. Alt’shuler, A. G. Aronov, and B. Z. Spivak. *Pis’ma Zh. Eksp. Teor. Fiz.*, 33(101), 1981 [JETP Lett. 33, 94 (1981)].
- [8] B. L. Altshuler, A. G. Aronov, B. Z. Spivak, D. Yu. Sharvin, and Yu. V. Sharvin. Observation of the Aaronov-Bohm effect in hollow metal cylinders. *JETP Letters*, 35(11):588–591, 1982.
- [9] Hubert Ammann and Nelson Christensen. Delta Kick Cooling: A New Method for Cooling Atoms. *Physical Review Letters*, 78(11):2088–2091, March 1997.
- [10] M. H. Anderson, J. R. Ensher, M. R. Matthews, C. E. Wieman, and E. A. Cornell. Observation of Bose-Einstein Condensation in a Dilute Atomic Vapor. *Science*, 269(5221):198–201, 1995.
- [11] P.W. Anderson. Absence of diffusion in certain random lattices. *Physical Review*, 109(5):1492–1505, 1958.
- [12] P.W. Anderson. Local moments and localized states. *Reviews of Modern Physics*, 50(2):191–201, 1978.

REFERENCES

- [13] PW Anderson, D J Thouless, T.V. Ramakrishnan, Peter Wölfle, Dieter Vollhardt, KB Efetov, and Sudip Chakravarty. *50 Years of Anderson Localization*. 2010.
- [14] Alain Aspect and Massimo Inguscio. Anderson localization of ultracold atoms. *Physics Today*, 62(8):30, 2009.
- [15] Adrian Bachtold, Christoph Strunk, Jean-Paul Salvetat, Jean-Marc Bonard, Laszlo Forro, Thomas Nussbaumer, and Christian Schöneberger. Aharonov - Bohm oscillations in carbon nanotubes. *Nature*, 397(6721):673–675, 1999.
- [16] G. Bayer and T. Niederdränk. Weak Localization of Acoustic Waves in Strongly Scattering Media. *Physical review letters*, 70(25):3884–3887, 1993.
- [17] Gordon Baym and C J Pethick. Ground-State Properties of Magnetically Trapped Bose-Condensed Rubidium Gas. *Physical Review Letters*, 76(1):6–9, 1996.
- [18] Gerd Bergmann. Weak localization in thin films: a time-of-flight experiment with conduction electrons. *Physics Reports*, 107(1):1–58, 1984.
- [19] A. Bernard. *Transport quantique dondes atomiques ultrafroides*. PhD thesis, Université Pierre et Marie Curie, 2010.
- [20] Juliette Billy, Vincent Josse, Zhanchun Zuo, Alain Bernard, Ben Hambrecht, Pierre Lugan, David Clément, Laurent Sanchez-Palencia, Philippe Bouyer, and Alain Aspect. Direct observation of Anderson localization of matter waves in a controlled disorder. *Nature*, 453(7197):891–894, June 2008.
- [21] C. C. Bradley, C. A. Sackett, J. J. Tollett, and R. G. Hulet. Evidence of Bose-Einstein Condensation in an Atomic Gas with Attractive Interactions. *Physical Review Letters*, 75(9):1687–1690, 1995.
- [22] Jean-Philippe Brantut, Jakob Meineke, David Stadler, Sebastian Krinner, and Tilman Esslinger. Conduction of ultracold fermions through a mesoscopic channel. *Science*, 337(6098):1069–1071, 2012.
- [23] G. Breit and I. I. Rabi. Measurement of Nuclear Spin. *Physical Review*, 38(11):2082–2083, 1931.

-
- [24] R. Carminati, J. J. Saenz, J.-J. Greffet, and M. Nieto-Vesperinas. Reciprocity, unitarity, and time-reversal symmetry of the S matrix of fields containing evanescent components. *PRA*, 62(012712):1–7, 2000.
- [25] Y. Castin. Bose-einstein condensates in atomic gases: Simple theoretical results. In R. Kaiser, C. Westbrook, and F. David, editors, *Coherent atomic matter waves*, volume 72 of *Les Houches - Ecole d'Ete de Physique Theorique*, pages 1–136. Springer Berlin Heidelberg, 2001.
- [26] Y Castin and R Dum. Bose-Einstein Condensates in Time Dependent Traps. *Physical Review Letters*, 77(27):5315–5319, 1996.
- [27] AA Chabanov, M Stoytchev, and AZ Genack. Statistical signatures of photon localization. *Nature*, 404(6780):850–853, 2000.
- [28] Julien Chabé, Gabriel Lemarié, Benoît Grémaud, Dominique Delande, Pascal Szriftgiser, and Jean Claude Garreau. Experimental observation of the anderson metal-insulator transition with atomic matter waves. *Physical review letters*, 101(25):255702, 2008.
- [29] Nicolas Cherroret, Tomasz Karpiuk, and A M Cord. Coherent backscattering of ultracold matter waves : Momentum space signatures. *Physical Review A*, 85(1), 2012.
- [30] D Clément, A F Varón, J A Retter, L Sanchez-Palencia, A Aspect, and P Bouyer. Experimental study of the transport of coherent interacting matter-waves in a 1D random potential induced by laser speckle. *New Journal of Physics*, 8(165):1–25, August 2006.
- [31] Claude Cohen-Tannoudji. Manipulating atoms with photons. *Physica Scripta*, 1998(T76):33, 1998.
- [32] J. C. Dainty. *Laser Speckle and Related Phenomena*. Springer, 1975.
- [33] Franco Dalfovo, Stefano Giorgini, Lev P Pitaevskii, and Sandro Stringari. Theory of Bose-Einstein condensation in trapped gases. *Reviews of Modern Physics*, 71(3):463–512, 1999.
- [34] J. Dalibard and C. Cohen-Tannoudji. Laser cooling below the Doppler limit by polarization gradients: simple theoretical models. *Journal of the Optical Society of America B*, 6(11):2023–245, November 1989.
- [35] K. B. Davis, M.-O. Mewes, M. R. Andrews, N. J. Van Druten, D. S. Durfee, D. M. Kurn, and W. Ketterle. Bose-Einstein Condensation in

REFERENCES

- a Gas of Sodium Atoms. *Physical Review Letters*, 75(22):3969–3973, 1995.
- [36] Kb Davis, Mo Mewes, Ma Joffe, Mr Andrews, and W Ketterle. Evaporative cooling of sodium atoms. *Physical review letters*, 74(26):5202–5205, June 1995.
- [37] Julien De Rosny, Arnaud Tourin, Arnaud Derode, Bart Van Tiggelen, and Mathias Fink. Relation between time reversal focusing and coherent backscattering in multiple scattering media: A diagrammatic approach. *Physical Review E*, 70(4):046601, 2004.
- [38] Dominique Delande and Giuliano Orso. Mobility edge for cold atoms in laser speckle potentials. *arXiv preprint arXiv:1403.3821*, 2014.
- [39] Arnaud Derode, Philippe Roux, and Mathias Fink. Robust Acoustic Time Reversal with High-Order Multiple Scattering. *Physical Review Letters*, 75(23):4206–4210, 1995.
- [40] F. A. Erbacher, R. Lenke, and G Maret. Multiple Light Scattering in Magneto-optically Active Media . *Europhysics Letters*, 21(5):551–556, 1993.
- [41] M. Fauquembergue. *Réalisation d’un dispositif de condensation de Bose-Einstein et de transport d’un échantillon cohérent d’atomes*. PhD thesis, Université Paris XI Orsay, 2004.
- [42] Marcel Filoche and Svitlana Mayboroda. Universal mechanism for Anderson and weak localization. *Proceedings of the National Academy of Sciences of the United States of America*, 109(37):14761–6, September 2012.
- [43] Mathias Fink, Didier Cassereau, Arnaud Derode, Claire Prada, Philippe Roux, Mickael Tanter, Jean-louis Thomas, and François Wu. Time-reversed acoustics. *Rep*, 63:1933–1995, 2000.
- [44] Mathias Fink, Gabriel Montaldo, and Mickael Tanter. Time-reversal acoustics in biomedical engineering. *Annual review of biomedical engineering*, 5(1):465–497, 2003.
- [45] M. Gehm, K. OHara, T. Savard, and J. Thomas. Dynamics of noise-induced heating in atom traps. *Physical Review A*, 58(5):3914–3921, November 1998.

-
- [46] S Ghosh, N Cherroret, B Grémaud, C Miniatura, and D Delande. Coherent forward scattering in 2D disordered systems. pages 1–12, 2014.
- [47] A. A. Golubentsev. Suppression of interference effects in multiple scattering of light. *Sov. Phys. JETP*, 59(1):26–32, 1984.
- [48] J W Goodman. Some fundamental properties of speckle*. *J. Opt. Soc. Am.*, 66(11):1145–1150, 1976.
- [49] E E Gorodnichev and D B Rogozkin. Coherent backscattering of a light pulse by a slab of disordered medium. *Waves in Random Media*, 4(1):51–57, January 1994.
- [50] Rudolf Grimm, Matthias Weidemüller, and Yurii B Ovchinnikov. Optical dipole traps for neutral atoms. pages 1–39, 1999.
- [51] Michael Hartung, Thomas Wellens, Cord Müller, Klaus Richter, and Peter Schlagheck. Coherent Backscattering of Bose-Einstein Condensates in Two-Dimensional Disorder Potentials. *Physical Review Letters*, 101(2):1–4, July 2008.
- [52] C. Henkel, J.-Y. Courois, and A. Aspect. Atomic diffraction by a thin phase grating. *J. Phys. II France*, 4:1955–1974, 1994.
- [53] Hefei Hu, a. Strybulevych, J. H. Page, S. E. Skipetrov, and B. a. van Tiggelen. Localization of ultrasound in a three-dimensional elastic network. *Nature Physics*, 4(12):945–948, October 2008.
- [54] AF Ioffe and AR Regel. Non-crystalline, amorphous and liquid electronic semiconductors. *Prog. Semicond*, 4:237–291, 1960.
- [55] F. Jendrzejewski. *Quantum Transport of Ultracold Atoms in Disordered Potentials: Anderson Localization in Three Dimensions, Coherent Backscattering*. PhD thesis, Université Paris XI, 2012.
- [56] F. Jendrzejewski, a. Bernard, K. Müller, P. Cheinet, V. Josse, M. Piraud, L. Pezzé, L. Sanchez-Palencia, a. Aspect, and P. Bouyer. Three-dimensional localization of ultracold atoms in an optical disordered potential. *Nature Physics*, 8(3):1–6, March 2012.
- [57] F Jendrzejewski, K Müller, J Richard, A Date, T Plisson, P Bouyer, A Aspect, and V Josse. Coherent Backscattering of Ultracold Atoms. *Physical Review Letters*, 195302(November):1–5, 2012.

REFERENCES

- [58] Yu. Kagan, E. L. Surkov, and G. V. Shlyapnikov. Evolution of a Bose gas in anisotropic time-dependent traps. *Physical Review A*, 55(1):18–21, 1997.
- [59] T. Karpiuk, N. Cherroret, K. Lee, B. Grémaud, C. Müller, and C. Miniatura. Coherent Forward Scattering Peak Induced by Anderson Localization. *Physical Review Letters*, 109(19):1–5, November 2012.
- [60] Wolfgang Ketterle, D S Durfee, and D. M. Stamper-Kurn. Making, probing and understanding Bose-Einstein condensates. In *Proceedings of the International School of Physics "Enrico Fermi"*, pages 67–176, 1999.
- [61] K. Kitagami, K. Hosumi, K. Goto, and a. Hatakeyama. Quantitative measurements of light-induced desorption of rubidium atoms from quartz substrates. *Physical Review A*, 85(6):062901, June 2012.
- [62] S S Kondov, W. R. McGehee, J. J. Zirbel, and B. DeMarco. Three-Dimensional Anderson Localization of Ultracold Matter. *Science*, 334(6052):66–68, 2011.
- [63] Yasuo Kuga and Akira Ishimaru. Retroreflectance from a dense distribution of spherical particles. *Journal of the Optical Society of America A*, 1(8):831, August 1984.
- [64] R C Kuhn, O Sigwarth, C Miniatura, D Delande, and C A Müller. Coherent matter wave transport in speckle potentials. *New Journal of Physics*, 9(6):161–161, June 2007.
- [65] W A Kuperman, William S Hodgkiss, Hee Chun Song, and Darrell R Jackson. Phase conjugation in the ocean: Experimental demonstration of an acoustic time-reversal mirror a). *Journal of Acoustical Society of America*, 103(1):25–40, 1998.
- [66] Ad Lagendijk, Bart van Tiggelen, and Diederik S. Wiersma. Fifty years of Anderson localization. *Physics Today*, 62(8):24, 2009.
- [67] Yoav Lahini, Assaf Avidan, Francesca Pozzi, Marc Sorel, Roberto Morandotti, Demetrios N Christodoulides, and Yaron Silberberg. Anderson localization and nonlinearity in one-dimensional disordered photonic lattices. *Physical Review Letters*, 100(1):013906, 2008.

-
- [68] E. Larose, L. Margerin, B. van Tiggelen, and M. Campillo. Weak Localization of Seismic Waves. *Physical Review Letters*, 93(4):1–4, July 2004.
- [69] Kean Loon Lee, Benoît Grémaud, and Christian Miniatura. Dynamics of localized waves in 1d random potentials: statistical theory of the coherent forward scattering peak. *arXiv preprint arXiv:1405.2979*, 2014.
- [70] Anthony J Leggett. Bose-Einstein condensation in the alkali gases : Some fundamental concepts. *Reviews of Modern Physics*, 73(April):307–356, 2001.
- [71] G. Lemarié, B. Grémaud, and D. Delande. Universality of the Anderson transition with the quasiperiodic kicked rotor. *EPL (Europhysics Letters)*, 87(3):37007, August 2009.
- [72] R Lenke and G Maret. Magnetic field effects on coherent backscattering of light. *The European Physical Journal B*, 17:171–185, 2000.
- [73] G. Lerosey, J. de Rosny, A. Tourin, A. Derode, G. Montaldo, and M. Fink. Time Reversal of Electromagnetic Waves. *Physical Review Letters*, 92(19), May 2004.
- [74] Paul D Lett, Richard N Watts, Christoph I Westbrook, William D Phillips, Phillip L Gould, and Harold J Metcalf. Physical review. *Physical Review Letters*, 61(2):169–173, 1988.
- [75] Matthias Lopez, Jean-François Clément, Pascal Szriftgiser, Jean Claude Garreau, and Dominique Delande. Experimental Test of Universality of the Anderson Transition. *Physical Review Letters*, 108(9):095701, February 2012.
- [76] F. C. MacKintosh and S. John. Coherent backscattering of light in the presence of time-reversal-noninvariant and parity-nonconserving media. *Physical Review B*, 37(4):1884–1897, 1988.
- [77] H J Metcalf and P van der Straten. Laser cooling and trapping of atoms. *J. Opt. Soc. Am. B*, 20(5):887–908, 2003.
- [78] Harold J Metcalf and Peter Van der Straten. *Laser cooling and trapping*. Springer, 2002.

REFERENCES

- [79] T. Micklitz, C. a. Müller, and A. Altland. Strong Anderson Localization in Cold Atom Quantum Quenches. *Physical Review Letters*, 112(11):110602, March 2014.
- [80] T Micklitz, CA Müller, and A Altland. Echo spectroscopy of anderson localization. *arXiv preprint arXiv:1406.6915*, 2014.
- [81] C Miniatura, RC Kuhn, D Delande, and CA Müller. Quantum diffusion of matter waves in 2d speckle potentials. *The European Physical Journal B-Condensed Matter and Complex Systems*, 68(3):353–364, 2009.
- [82] F. L. Moore, J. C. Robinson, C. Bharucha, P. E. Williams, and M. G. Raizen. Observation of Dynamical Localization in Atomic Momentum Transfer: A New Testing Ground for Quantum Chaos. *Physical Review Letters*, 73(22):2974–2977, 1994.
- [83] Cord A Müller and Boris Shapiro. Diffusive density profiles in a cold-atom expansion experiment. *arXiv preprint arXiv:1406.5107*, 2014.
- [84] Otto L. Muskens, Paul Venn, Timmo van der Beek, and Thomas Wellens. Partial Nonlinear Reciprocity Breaking through Ultrafast Dynamics in a Random Photonic Medium. *Physical Review Letters*, 108(22):1–4, May 2012.
- [85] Timo Bastian Ottenstein. *A New Objective for High Resolution Imaging of Bose-Einstein Condensates*. PhD thesis, University of Heidelberg, 2006.
- [86] J.P. Pérez. *Optique: fondements et applications*. Masson sciences. Dunod, 2000.
- [87] M. Peshkin and A. Tonomura. *The Aharonov-Bohm Effect*. Lecture Notes in Physics. Springer Berlin Heidelberg, 2014.
- [88] Wolfgang Petrich, Michael H Anderson, Jason R Ensher, and Eric A Cornell. Stable, Tightly Confining Magnetic Trap for Evaporative Cooling of Neutral Atoms. *Physical Review Letters*, 74(17):0–3, 1995.
- [89] William Phillips and Harold Metcalf. Laser Deceleration of an Atomic Beam. *Physical Review Letters*, 48(9):596–599, March 1982.
- [90] M. Piraud. *Localisation d’Anderson d’ondes de matière dans un désordre corrélé : de 1D à 3D*. PhD thesis, Université Paris Sud, 2012.

-
- [91] Marie Piraud, Luca Pezze, and Laurent Sanchez-Palencia. Matter wave transport and Anderson localization in anisotropic three-dimensional disorder. *EPL (Europhysics Letters)*, 99(September):1–6, 2012.
- [92] T. Plisson. Propriétés d’équilibre et de transport de gaz de bose bidimensionnels en présence de désordre, 2012.
- [93] Thomas Plisson, Thomas Bourdel, and Cord A Müller. Momentum isotropisation in random potentials. *The European Physical Journal Special Topics*, 217(1):79–84, 2013.
- [94] David E Pritchard. Cooling Neutral Atoms in a Magnetic Trap for Precision Spectroscopy. *Physical Review Letters*, 51(15):1336–1339, 1983.
- [95] A. Prasadka, S. Feat, P. Petitjeans, V. Pagneux, A. Maurel, and M. Fink. Time Reversal of Water Waves. *Physical Review Letters*, 109(1-5), 2012.
- [96] E. L. Raab, M. Prentiss, Alex Cable, Steven Chu, and D. E. Pritchard. Trapping of Neutral Sodium Atoms with Radiation Pressure. *Physical Review Letters*, 59(23):2631–2634, 1987.
- [97] Giacomo Roati, Chiara DErrico, Leonardo Fallani, Marco Fattori, Chiara Fort, Matteo Zaccanti, Giovanni Modugno, Michele Modugno, and Massimo Inguscio. Anderson localization of a non-interacting bose–einstein condensate. *Nature*, 453(7197):895–898, 2008.
- [98] M. Robert-de Saint-Vincent, J.-P. Brantut, B. Allard, T. Plisson, L. Pezzé, L. Sanchez-Palencia, a. Aspect, T. Bourdel, and P. Bouyer. Anisotropic 2D Diffusive Expansion of Ultracold Atoms in a Disordered Potential. *Physical Review Letters*, 104(22):2–5, June 2010.
- [99] C. Sackett. Limits on weak magnetic confinement of neutral atoms. *Physical Review A*, 73(1):013626, January 2006.
- [100] J. J. Sakurai and Jim Napolitano. *Modern Quantum Mechanics*. Jim Smith, 2011.
- [101] Laurent Sanchez-palencia and Maciej Lewenstein. Disordered quantum gases under control. *Nature Physics*, 6(2):87–95, 2010.

REFERENCES

- [102] Tal Schwartz, Guy Bartal, Shmuel Fishman, and Mordechai Segev. Transport and Anderson localization in disordered two-dimensional photonic lattices. *Nature*, 446(7131):52–55, March 2007.
- [103] Giulia Semeghini, Manuele Landini, Patricia Castilho, Sanjukta Roy, Giacomo Spagnolli, Andreas Trenkwalder, Marco Fattori, Massimo Inguscio, and Giovanni Modugno. Measurement of the mobility edge for 3d anderson localization. *arXiv preprint arXiv:1404.3528*, 2014.
- [104] Boris Shapiro. Cold atoms in the presence of disorder. *Journal of Physics A: Mathematical and Theoretical*, 45(14):143001, April 2012.
- [105] DU Sharvin and YUV Sharvin. Magnetic flux quantization in a cylindrical film of a normal metal. *JETP Lett.*, 34(5):272–275, 1981.
- [106] B. I. Shklovskii. Superfluid-insulator transition in Dirty ultracold Fermi gas. *Semiconductors*, 42(8):909–913, August 2008.
- [107] Sergey E Skipetrov, A. Minguzzi, Bart A van Tiggelen, and Boris Shapiro. Anderson Localization of a Bose-Einstein Condensate in a 3D Random Potential. *Physical Review Letters*, 100(16):165301, April 2008.
- [108] J Söding, D Guéry-Odelin, P Desbiolles, F Chevy, H Inamori, and J Dalibard. Three-body decay of a rubidium bose-einstein condensate. *Applied physics B*, 69(4):257–261, 1999.
- [109] Daniel Adam Steck. Rubidium 87 D Line Data. Technical report, 2010.
- [110] Martin Störzer, Peter Gross, Christof Aegerter, and Georg Maret. Observation of the Critical Regime Near Anderson Localization of Light. *Physical Review Letters*, 96(6):1–4, February 2006.
- [111] Arnaud Tourin, Arnaud Derode, Philippe Roux, Bart van Tiggelen, and Mathias Fink. Time-Dependent Coherent Backscattering of Acoustic Waves. *Physical Review Letters*, 79(19):3637–3639, 1997.
- [112] Leung Tsang and Akira Ishimaru. Backscattering enhancement of random discrete scatterers. *Journal of the Optical Society of America A*, 1(8):836–839, August 1984.
- [113] Meint P. Van Albada and Ad Lagendijk. Observation of Weak Localization of Light in a Random Medium. *Physical Review Letters*, 55(24):2692–2695, 1985.

-
- [114] Bart A Van Tiggelen. Localization of waves. In *Diffuse waves in complex media*, pages 1–60. Springer, 1999.
- [115] Bart A van Tiggelen and Roger Maynard. Reciprocity and coherent backscattering of light. In *Wave Propagation in Complex Media*, pages 247–271. Springer, 1998.
- [116] R Vreeker, M P Van Albada, R Sprik, and A Lagendijk. Femtosecond time-resolved measurements of weak localization of light. *Physics Letters A*, 132(1):51–54, 1988.
- [117] Kenneth M. Watson. Multiple Scattering of Electromagnetic Waves in an Underdense Plasma. *Journal of Mathematical Physics*, 10(4):688–702, 1969.
- [118] R. A. Webb, S. Washburn, C. P. Umbach, and R. B. Laibowitz. Observation of h/e Aharonov-Bohm Oscillations in Normal-Metal Rings. *Physical Review Letters*, 54(25):2696–2699, 1985.
- [119] Peter B Weichman. Dirty Bosons: Twenty Years Later. *Modern Physics Letters B*, 22(27):2623–2647, 2008.
- [120] Diederik S Wiersma, Paolo Bartolini, Ad Lagendijk, and Roberto Righini. Localization of light in a disordered medium. *Nature*, 390(December):671–673, 1997.
- [121] DS Wiersma, MP van Albada, BA van Tiggelen, and Ad Lagendijk. Experimental Evidence for Recurrent Multiple Scattering Events of Light in Disordered Media. *Physical Review letters*, 74(21):4193, 1995.
- [122] Pierre-Etienne Wolf and Georg Maret. Weak Localization and Coherent Backscattering of Photons in Disordered Media. *Physical Review Letters*, 55(24):2696–2699, 1985.
- [123] Afifa Yedjour and BA Van Tiggelen. Diffusion and localization of cold atoms in 3d optical speckle. *The European Physical Journal D-Atomic, Molecular, Optical and Plasma Physics*, 59(2):249–255, 2010.